



2020 Midwest American Society of Biomechanics

Regional Meeting
April 8-9 Cleveland, Ohio



Washkewicz College
of Engineering

engineering.csuohio.edu/MidwestASB2020



To Do tasks

Here are tasks still needed for this book.

1. Add sponsors

2. Add front matter content

3. Add back cover

Sponsors

All work and no play makes Jack a dull boy. All work and no play makes Jack a dull boy. All work and no play makes Jack a dull boy. All work and no play makes Jack a dull boy. All work and no play makes Jack a dull boy. All work and no play makes Jack a dull boy. All work and no play makes Jack a dull boy. All work and no play makes Jack a dull boy. All work and no play makes Jack a dull boy.

Schedule

All work and no play makes Jack a dull boy. All work and no play makes Jack a dull boy. All work and no play makes Jack a dull boy. All work and no play makes Jack a dull boy. All work and no play makes Jack a dull boy. All work and no play makes Jack a dull boy. All work and no play makes Jack a dull boy. All work and no play makes Jack a dull boy.

RESULTANT SHOCK ATTENUATION IS GREATER WHEN RUNNING OVER TRAIL SURFACES COMPARED TO PAVEMENT

¹Micah C. Garcia, ²Gianna DePons, and ¹David M. Bazett-Jones

¹University of Toledo, Toledo, OH, USA

²Carroll University, Waukesha, WI, USA

Email: micah.garcia@rockets.utoledo.edu

INTRODUCTION

Tibial acceleration (TA) and shock attenuation (SA) are associated with running-related injuries (RRIs), specifically tibial stress fractures [1, 2]. Previous research has been limited to analysis of only the vertical component of TA and SA during running [3, 4]. However, these analyses may be inadequate as they neglect anterior-posterior and medial-lateral accelerations.

Trail running (running over unpaved surfaces) has increased in popularity in recent years. It is believed that trail running surfaces are softer than pavement surfaces, but it is unclear if these surfaces influence resultant TA (rTA) or resultant SA (rSA). Therefore, the purpose of this study was to investigate differences in peak rTA and rSA between trail (dirt and gravel) and pavement running surfaces.

METHODS

Seventeen ($m = 5$, $f = 12$, age = 26.8 ± 8.9 years) uninjured recreational runners participated in this repeated-measures study. Participants were instrumented with triaxial accelerometers (TeleMyo DTS 3D, Noraxon USA Inc.) on the forehead and medial distal tibia. Participants ran over three different surface types (dirt, gravel, and pavement) at a public park while wearing a standard shoe (Saucony Jazz).

Self-selected running speed was determined during three, 30 m runs over a paved path. Participants were provided a 10 m run-up to reach self-selected running speed and then maintained speed over an additional 30 m. Trials were repeated until four runs on each surface were within $\pm 5\%$ of the self-selected running speed. Trials with running speeds greater than $\pm 5\%$ different from the self-selected running speed were

excluded from analysis. To account for accelerating or decelerating, the first and last five steps were excluded for analysis.

Triaxial peak acceleration was identified from the right tibia and head accelerometers and used for analysis. Resultant TA and head acceleration (rHA) were calculated by adding the peak vertical, anterior-posterior, and medial-lateral accelerations for each accelerometer. Resultant SA was calculated with the following equation:

$$rSA = \left(1 - \frac{rHA}{rTA}\right) \times 100$$

One-way ANOVAs with Fisher's LSD *post-hoc* tests were used to compare rTA and rSA among the three surface types. Significance was set at $P \leq 0.05$.

RESULTS AND DISCUSSION

Results found no significant differences in rTA between surface types (dirt = 20.80 ± 6.20 g, gravel = 21.85 ± 6.73 g, pavement = 18.61 ± 7.09 g; $P = 0.432$, partial $\eta^2 = 0.04$; Figure 1). These findings parallel previous results comparing vertical TA between surfaces with varying magnitudes of softness [3, 4]. While no differences have been found between vertical TA or rTA and surface types, rTA is likely a more appropriate measure to report. The rTA includes triaxial accelerations in the analysis and accounts for movement in all three planes. Anterior-posterior TA has been found to be different in rearfoot and non-rearfoot strikers demonstrating the importance of rTA analysis to consider the cumulative effect of multiaxial accelerations. A major limitation of uniaxial acceleration is that confounding effect of accelerometer orientation [5]. By analyzing rTA, this controls for any

accelerometer placement errors that may influence a plane of acceleration.

Resultant SA was significantly lower during running over pavement ($82.4 \pm 4.5\%$; Figure 2) than both dirt ($85.4 \pm 2.9\%$; $P = 0.039$) and gravel ($85.6 \pm 3.4\%$; $P = 0.024$) surfaces. No significant differences were found between dirt and gravel surfaces ($P = 0.839$).

Shock attenuation measures the body's capabilities to dissipate energy between the foot and the head [6]. Lower SA is indicative that muscles have a diminished capacity to dissipate energy. To our knowledge, this is the first study to report rSA during trail running. Over the course of a prolonged run, the lower rSA demonstrated with running over pavement surfaces may place the runner at a greater risk of sustaining a RRI compared to trail running, but this warrants further investigation.

CONCLUSION

Resultant SA is lower when running over pavement surfaces compared to trail surfaces (dirt and gravel) but there is no difference in rTA. The higher rSA suggest trail running may reduce the risk of impact-related running injuries.

REFERENCES

- [1] Milner, CE, et al. *Med Sci Sports Exerc.* 323-8, 2006.
- [2] Nordin, M, et al. *Basic Biomech of MSK System.* 1919-26, 2000.
- [3] Boey, H, et al. *Sports Biomech.* 166-76, 2017.
- [4] Garcia, MC, et al. *71st NATA Clinical Symposia.* Atlanta, GA, 2020.
- [5] Sheerin, KR, et al. *Gait Posture.* 12-24, 2019.
- [6] Shorten, MR, et al. *Int J Sport Biomech.* 288-304, 1992.

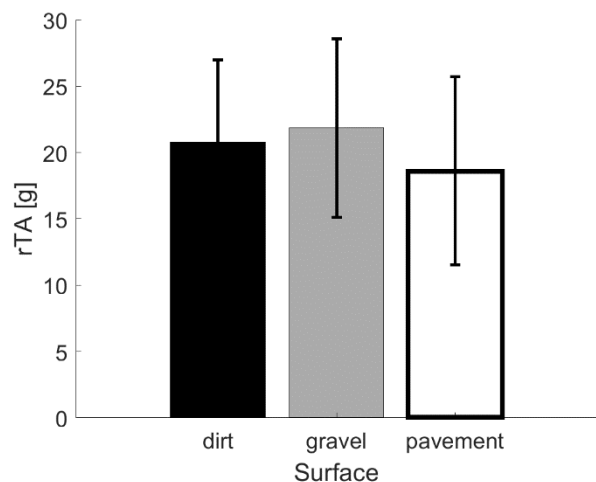


Figure 1: Dirt, gravel, and pavement rTA (g).

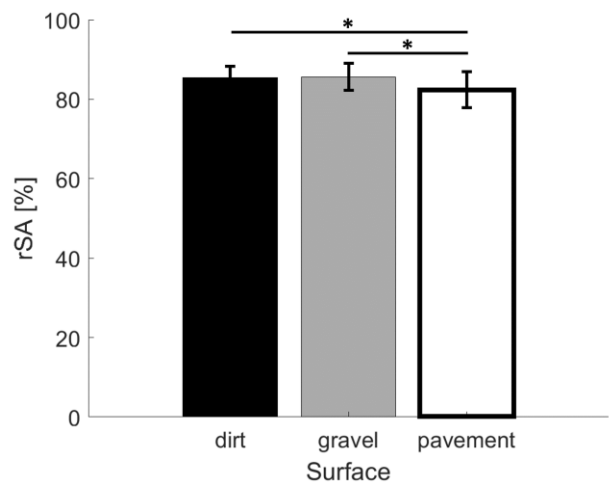


Figure 2: Dirt, gravel, and pavement rSA (%).
* denotes significant difference ($P < 0.05$).

THE EFFECT OF SOCK MATERIAL ON PLANTAR SURFACE SHEAR STRESSES

Shaye M. Tiell,¹ Brian L. Davis²

¹The University of Akron, Akron, OH, USA

²Department of Mechanical Engineering, Cleveland State University, Cleveland, OH, USA

Email: smt125@zips.uakron.edu

INTRODUCTION

At present, there are no viable systems that can acquire in-shoe measurement of distributed shear forces. The physics of foot-shoe interactions are such that a variable such as skin shear is a notoriously difficult quantity to measure under the best of conditions. This is further complicated in the case of the foot-ground interface by the presence of pressure forces that are large compared to the shear forces. This often results in cross-talk between pressure and shear signals. This study aimed at investigating the combined effects of interface friction (between the skin, sock and sensor) and sock stiffness through a model developed using a multi body dynamics package (MSC Adams).

METHODS

In order to investigate the combined effects of interface friction (between the skin, sock and sensor) and sock stiffness, a model was developed using a multi body dynamics package (MSC Adams).² While the human foot consists of various structures, the computational model created focused on a simple metatarsal bone covered by skin and connected with soft tissue.

Simulations were carried out with various coefficients of friction and sock stiffness for the following purposes: Aim 1 - Simulate the influence of sock stiffness for various

combinations of interface friction coefficients; Aim 2 - Simulate the influence of sock-skin coefficient of friction; Aim 3 - Simulate the influence of sock-sensor coefficient of friction.

RESULTS

The effect of sock-sensor coefficient of friction on S (Fig. 1) showed that with a low sock-sensor coefficient of friction of 0.04, the slope was highest (less ideal). At the highest coefficient of friction of 0.9, S was lowest, reaching a minimum value of -0.4599. The highest coefficient of friction was slightly outside of the range used by Dai et al.¹ but roughly the maximum possible value found by Zhang et al.³ Thus, even at an unreasonably high coefficient of friction, S was still far from its ideal value of -1.

For any sock-sensor coefficient of friction, changing sock-skin coefficient of friction had little effect on S. This is highlighted by the fact that the maximum standard deviation of S across all sock-skin conditions was 0.147%.

The degree to which sock stiffness increases the effectiveness of a shear pressure sensor (Fig. 2) is dependent on the sock-sensor coefficient of friction. If the sock-sensor coefficient of friction is low, the sock stiffness does not improve a sensor's ability to record skin stresses, as shown by the maximum slope of S = -0.0378. If the sock-

sensor coefficient of friction is higher, S reaches a minimum value of -0.5221, closer to its ideal value of -1.

In terms of the influence of sock-skin coefficient of friction (Fig. 3), S values were high (less ideal) with a high sock stiffness of 2000 N/m. At the lowest sock stiffness of 500 N/m, S was lowest (more ideal), reaching a minimum value of -0.5203. For any sock stiffness, changing sock-skin coefficient of friction had little effect on S. This is highlighted by the fact that the maximum standard deviation of S across all sock-skin conditions was 0.168%.

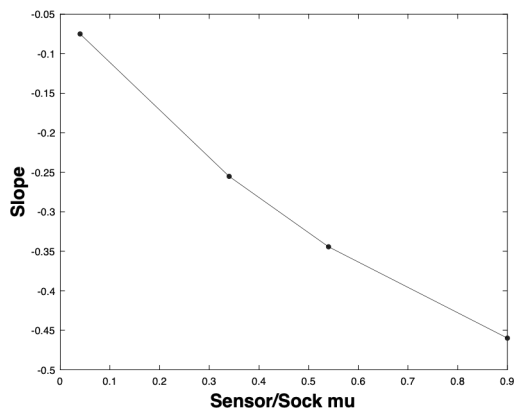


Figure 1: As the sock-sensor coefficient of friction increases, S decreases showing an inverse relationship.

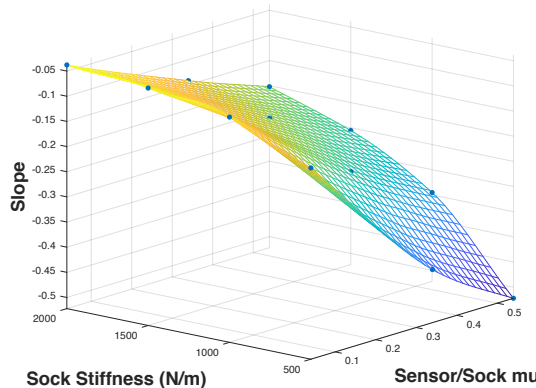


Figure 2: The degree to which sock stiffness improves the value of S is

dependent on the sock-sensor coefficient of friction.

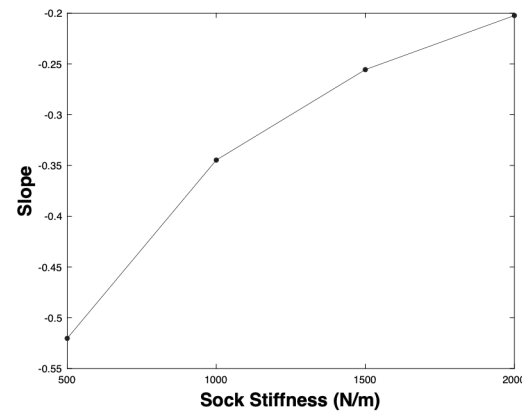


Figure 3: As the sock stiffness decreases, S also decreases showing a direct relationship.

DISCUSSION

The computational model developed in this study suggests that (i) any interface with coefficients of friction less than unity will degrade the accuracy of a sensor, (ii) sock stiffness has a profound effect (with stiff materials significantly degrading a sensor's reading), and (iii) sock weaves that have bi-directional differences, will have differential effects on antero-posterior shear versus medio-lateral shear.

REFERENCES

1. Dai et al., Effect of sock on biomechanical responses of foot during walking, Clinical Biomechanics 21 (2006) 314-321
2. MSC Software. (n.d.). Adams Student Edition (Version 2019.2) [Computer software]. Retrieved July 1, 2019, from <https://studentedition.mscsoftware.com/User/ProductsDownloadPage.aspx>
3. Zhang et al., In vivo friction properties of human skin, Prosthetics and Orthotics International 23 (1999) 135-141

SIMULATION BASED ANALYSIS OF ANATOMY SPECIFIC ANTERIOR CRUCIATE LIGAMENT GRAFT OPTIMAZTION IN PEDAATRIC POPULATIONS

¹Mallinos, A.D (Presenter), Davis, B.L and ²Jones, K.

¹Cleveland State University, Cleveland, OH, USA ²Akron

Children's Hospital, Akron, OH, USA

Email: a.mallinos@vikes.csuohio.edu

INTRODUCTION

Between the years of 2005 and 2015, the overall rate of Anterior Cruciate Ligament (ACL) tears has increased by 147.8% within the pediatric population [1]. Due to the high incidence of reinjury, it is vital to develop new surgical procedures that will ultimately reduce the risk of graft failure. In recent years, anatomic specific reconstructions have become more widely used amongst surgeons. This requires determining the femoral and tibial footprint locations of the ACL on that specific patient.

However, despite the importance of the attachment points of the ACL, no researcher has ever investigated the relationship between the ACL insertion points and angle with respect to the patient's unique morphological anatomy such as the radius of curvature of the femur and the ligamentous attachment location on the tibial plateau. The purpose of this study is to analyze the stresses placed on the ACL with respect to the geometry of the knee (i.e. the curvature of the femoral condyles, ACL insertion angles and location). Ultimately, the results collected can be used as a tool for surgeons to determine the optimal ACL graft insertion points based on the patient's unique anatomy.

METHODS

14 deidentified MRIs of healthy knees of pediatric patients ages 7 to 17 will be utilized. The pediatric

subjects must have open growth plates at the distal femur and proximal tibia. Using computer software, 3D Slicer, the bony anatomy of the patient will be extracted from the MR images (Figure 1).



Figure 1: Bony geometry extracted from 14-year-old female using 3D Slicer.

The bony anatomy will then be loaded into FEBio, a finite element mesh generator and analyzer, where the ligaments and soft tissues will be modeled. Using similar methodologies developed by Erdemir [2], a knee flexion from 0-60 degrees will be simulated (Figure 2). Various iterations of the ACL insertion points will be used and the stress generated will be analyzed with respect to the patient's unique morphological anatomy.

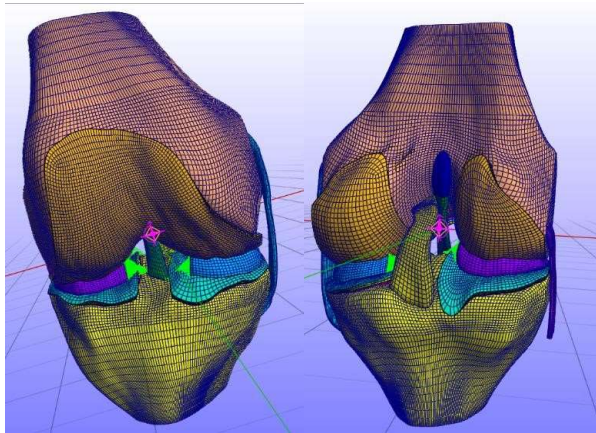


Figure 2: Tibiofemoral joint model developed by Erdemir [2] that was based on anatomical and mechanical data collected on a cadaver right knee from a 70-year-old female donor. Model includes ligaments and meniscus.

RESULTS AND DISCUSSION

The stress on the ACL during 60 degrees of knee flexion can be observed in Figure 3. A plot of the stress of the ligament throughout the flexion cycle is illustrated in Figure 4.

From the data, it is clear that the ACL experiences various stress throughout the 60-degree flexion cycle. For our research, we will analyze ways in which the stress of the ACL is impacted during simulation with respect to the patient's unique anatomy.

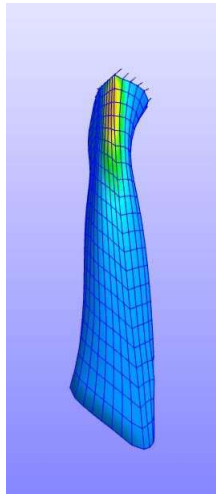


Figure 3: Simulated sagittal plane stress on the ACL during 60 degrees of flexion. Data model obtained from Erdemir [2].

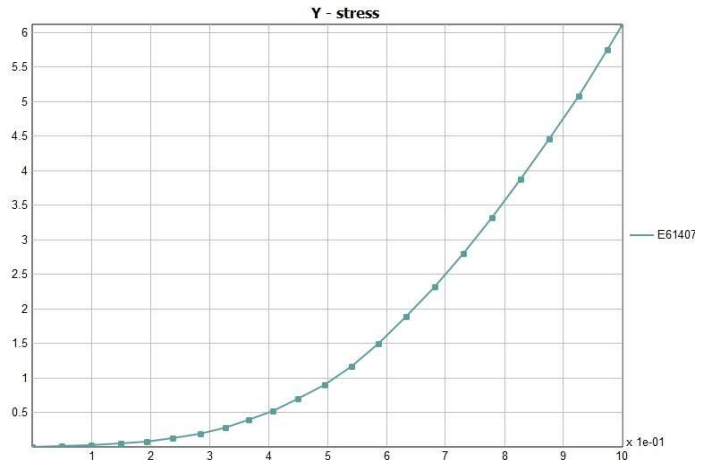


Figure 4: Simulated sagittal plane stress on the ACL during the 60 degrees of the flexion-cycle. Data obtained from Erdemir [2] model.

CONCLUSION

We will apply the methodology developed by Erdemir [2] to pediatric patients to analyze the stress placed on the ACL with respect to the geometry of the knee.

This information will be beneficial to the surgeon as it will enable the physician to customize tunnel position based on the patient's unique morphology.

In doing so, the number of ACL revisions will substantially decrease.

REFERENCES

- Shaw, L., & Finch, C. (2017). Trends in pediatric and adolescent anterior cruciate ligament injuries in Victoria, Australia 2005–2015. *International journal of environmental research and public health*, 14(6), 599.
- Erdemir, A. (2016). Open knee: open source modeling and simulation in knee biomechanics. *The journal of knee surgery*, 29(02), 107-116

NOVEL MOTOR TRAINING FOR STROKE SURVIVORS: CHANGES IN FRONTAL PLANE MOTION AND FREQUENCY CHARACTERISTICS

Jiafeng Song¹, Jessica P. McCabe², Margaret Skelly², Svetlana Pundik^{2,4}, and Elizabeth C. Hardin^{1,3}

¹Department of Biomedical Engineering, Case Western Reserve University, Cleveland, OH

²Brain Plasticity & NeuroRecovery Lab, Cleveland FES Center, Cleveland VA Medical Center

³Human Performance Virtual Reality Lab, Cleveland FES Center, Cleveland VA Medical Center.

⁴Department of Neurology, School of Medicine, Case Western Reserve University, Cleveland, OH

Email: jiafeng.song@case.edu

INTRODUCTION

Stroke survivors commonly experience unilateral lack of control in their lower limb joints (paresis). Impaired paretic limb motor control when walking can result in larger and varying limb displacement than normal in the frontal plane due to reliance on hip abduction for toe clearance during swing. This paretic limb displacement in the frontal plane can cause instability during walking, increases energy cost¹, and requires greater active balance control than anteroposterior displacement². The purpose of this study is to determine whether a novel motor training task for stroke survivors can reduce the magnitude and variability of paretic limb displacement in frontal plane, as well as determine whether frequency characteristics of the limbs are modified.

METHODS

Following approval for the study from our Institutional Review Board, two stroke survivors were recruited. Subject A was a 72-year-old male (61 months post-stroke, height=1.83m, weight= 84.4kg) and Subject B was a 62-year-old male (150 months post-stroke, height=1.80m, weight=78.7kg). Both subjects had right leg paresis. They had 10 novel motor task training sessions plus baseline, mid-training, and post-training during which data were collected. Subject B had an additional post-training session three weeks after the end of training. Training was twice weekly for five weeks. During the novel

motor training task treadmill walking was performed at their preferred speed while stepping over obstacles created by a virtual reality system. They used their unaffected leg to clear the obstacles which shifted their center of gravity to the paretic leg, forcing it's use during the weight bearing stance phase. For data collection, markers were mounted on right and left lateral malleoli (RLM, LLM). Passive marker motion capture was performed at 100 Hz (Vicon, Oxford, UK), three-dimensional marker coordinates were calculated, and frontal plane motion was analyzed for both unaffected and paretic legs. Coefficient of variation (COV) and standard deviation were calculated to determine the variability during the training sessions. The frontal plane motion was also transformed into the frequency domain to determine the frequency characteristics.

RESULT AND DISCUSSION

For both subjects, the paretic leg had greater frontal plane displacement than the unaffected leg (Figure 1). Displacement mean values varied throughout the sessions. The displacement range and standard deviation decreased over time. From baseline to post-training sessions, the COV decreased in the unaffected leg (56% to 39%, Subject A; 30% to 26%, Subject B), and in the paretic leg (22% to 20%, Subject A; 46% to 32%, Subject B). In the frequency domain both legs had frequency correspondence, with greater peak magnitudes in the paretic leg. Training caused shifting to lower frequencies.

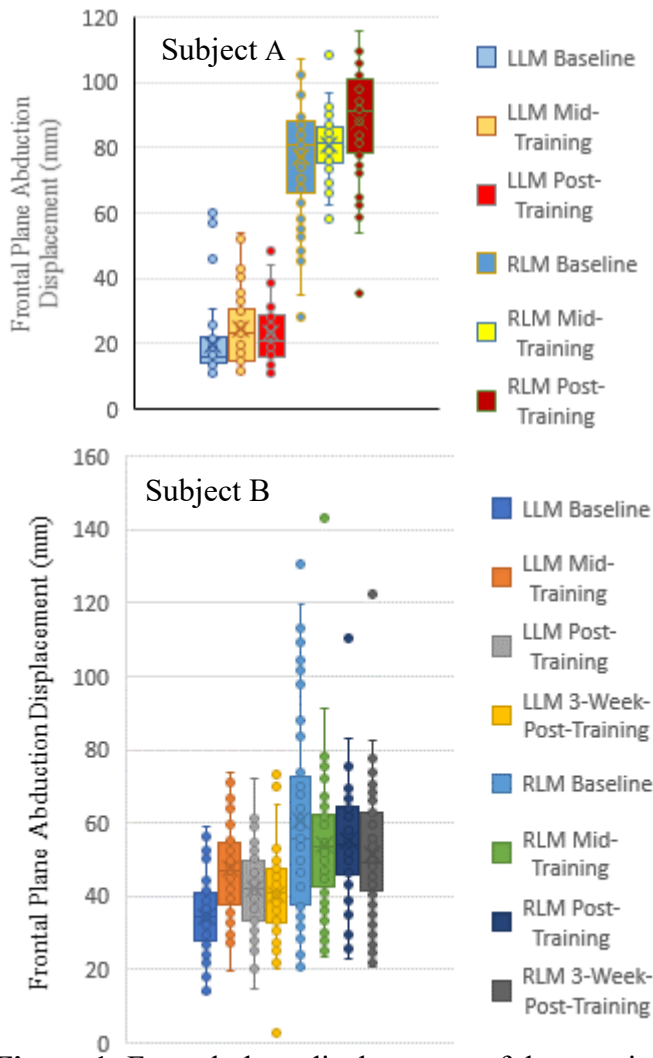


Figure 1: Frontal plane displacement of the paretic (RLM) and unaffected (LLM) legs during the evaluation sessions for the subjects.

CONCLUSION

The study demonstrates that the novel motor training task was effective in reducing variability of frontal plane limb displacement in both limbs, but did not reduce the magnitude. The shift to lower frequencies after training could be an indication of greater endpoint control. In addition, fatigue may have a critical influence on variability of lower limb frontal plane motion, which needs further study and evidence to support.

REFERENCE

1. Chen, G, et al. Gait Posture 22 (1), 51–56, 2005
2. O'Connor, S. J. Neurophysiol, 1411-9, 2009.
3. Highsmith, M, et al. Technol Innov, 99-113, 2016.

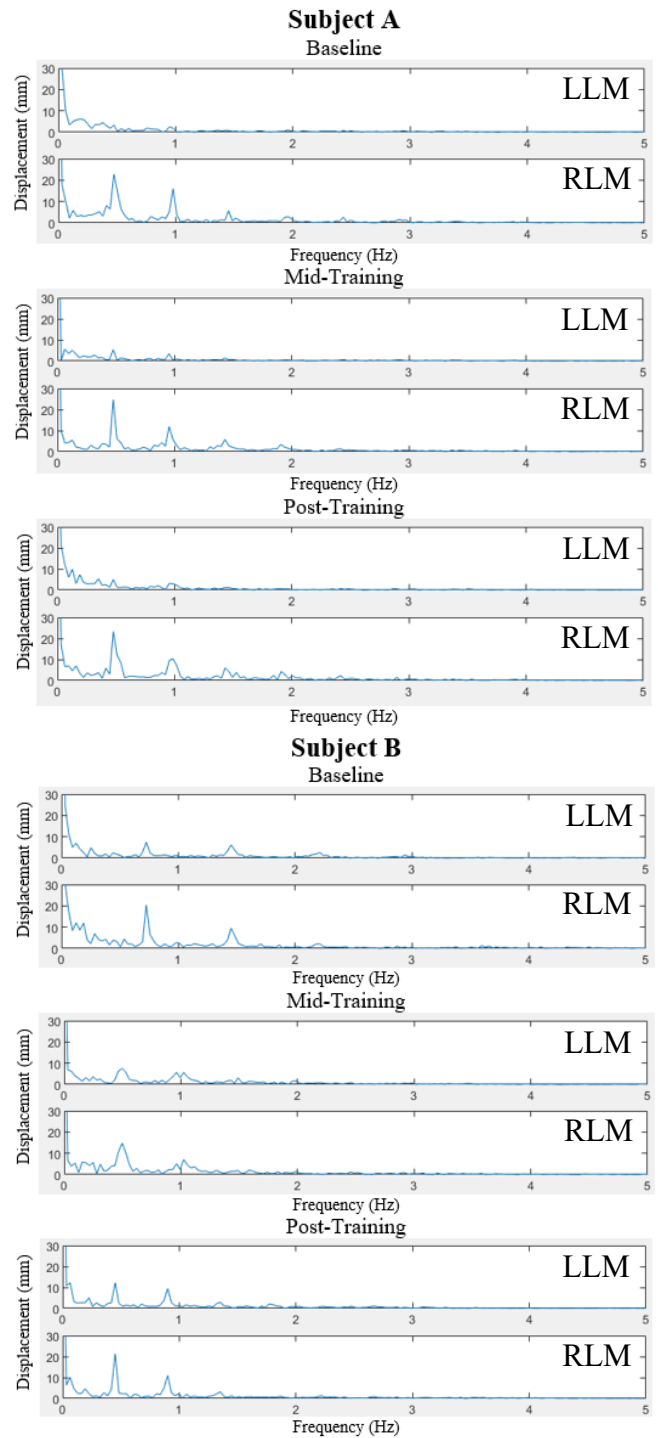


Figure 2: Paretic (RLM) and unaffected (LLM) legs frequency domain characteristics during the evaluation sessions for the subjects.

ACKNOWLEDGEMENTS

We gratefully acknowledge our funding from the Department of Veteran's Affairs (Merit Review award, Pundik).

ESTIMATION OF KNEE KINEMATICS FOR HEALTHY AND ACL-DEFICIENT CONDITIONS USING RULE-BASED KNEE MODELING

Neda Abdollahi^{1,2}, Jason P. Halloran³, Ahmet Erdemir¹

¹ Cleveland Clinic, Cleveland, Ohio, USA

² Cleveland State University, Cleveland, Ohio, USA

³ Washington State University, Spokane, Washington, USA

Email: abdolln@ccf.org

INTRODUCTION

Injury of the anterior cruciate ligament (ACL) alters joint kinematics and load distribution through the knee, and often predisposes the knee to subsequent disorders and early onset osteoarthritis (OA) [1, 2]. The ACL is the most frequently disrupted ligament in the knee [2] and is the primary restraint to the anterior motion of the tibia and a secondary constraint to internal-external and varus-valgus rotations of the knee [3].

Establishing computational tools to efficiently quantify the individualized mechanical environment of a knee joint is essential for developing surgical and rehabilitation procedures following ACL injury. It also has the potential to contribute to our understanding and management of OA development after ACL injury. Current knowledge of knee-specific motion is primarily based on direct measurement of said knee, or combined experimentation and computational simulations to estimate the mechanical response [4,5]. Thus, mechanical assessment of the knee is tied to the availability and quality of the experimental mechanics data, which are hard to obtain *in vivo*, necessitate significant resources, and may be susceptible to errors. A previously developed customizable rule-based framework minimized the need for experimental data by estimating knee-specific kinematics solely from routine clinical imaging [6]. This framework creates an easy to obtain biomechanical marker of knee motion signature that has the potential to be used efficiently in both healthy and pathological knee conditions by adjusting rule parameters. The framework has been previously used to reconstruct specimen-specific passive flexion motion of a healthy knee [6]. Thus, this study aimed to implement the rule-based framework to estimate

specimen-specific knee joint motion of the ACL-deficient condition through passive flexion motion and evaluate its potential utility for estimating changes in knee motion signature (i.e. passive flexion) due to pathology.

METHODS

Using freely available imaging data of two OpenKnee(s) [7], specimens (oks003: left knee, female, 25 years of age, 22.8 BMI; oks008: right knee, male, 40 years of age, 20.09 BMI), bony surfaces (for visualization), articulating cartilage surfaces, and insertion sites for ligaments were defined [6]. Bone and articular surfaces were represented using a triangular based mesh. Bundles of three major ligaments were included in the model (ACL-deficient model): 2 for posterior cruciate ligament (PCL), 3 for medial collateral ligament (MCL), and 1 for lateral collateral ligament (LCL). The rule-based framework optimized the discretized trajectory of the tibiofemoral joint kinematics (except flexion, which is prescribed from 0 to 90 degrees with 7 increments) in clinically relevant coordinate systems, developed from bony landmarks.

A gradient-based optimization (trust-constr, SciPy, Python) was utilized to minimize a weighted combination of: 1. covariance of ligament length changes from the average length of each ligament during passive motion (rule: ligaments remain isometric during passive flexion), 2. the anterior/posterior range of motion of the medial and lateral articular contact on tibial cartilage (rule: menisci's role to support joint conformity), and 3. the penetration/separation of the medial and lateral contact at each flexion (rule: enforcement of contact in both compartments). The objective function had the following form:

$$f(x) = W_1 \left[\sum_{k=1}^L \frac{\sum_{j=1}^N (Y_{kj} - y_k)^2}{N-1} \right]^2 + W_2 \left[(\max |C_m(x_j)|^2 + (\max |C_l(x_j)|^2) \right] + W_3 [(T_{AP,m})^2 + (T_{AP,l})^2] \quad (1)$$

Where Y_{kj} is the length of the k^{th} ligament at j^{th} flexion angle, and y_k is the average length of the ligament throughout the motion. C_m and C_l are the arrays of contact penetration/separation for the medial and lateral sides, respectively. $T_{AP,m}$, and $T_{AP,l}$ are the anterior/posterior range of motion of the medial and lateral contact centers, respectively. The optimization can be customized by selecting any desired weighting (W_1, W_2, W_3 in equation 1). To provide an initial guess to the optimization, all unknown trajectory variables were set to zero. In following, the maximum of penetration depth at each flexion angle was used as the initial guess for the superior translation. Calibrated kinematics of ACL-deficient model through the passive flexion motion were compared to the calibrated kinematics of the intact knee.

RESULTS AND DISCUSSION

For the same weight set reported in [6] ($W_1=50, W_2=1, W_3=1 \times 10^5$), knee motions for both intact and ACL-deficient conditions for two specimens are shown in Figure 2. Weights of the contact penetration/separation term were selected to be higher compared to the other two terms due to the smaller values of this term at different flexion angles.

ACL resection resulted in contrasting joint mechanics in the two specimens (Figure 2). However, the range of anterior-posterior (A-P) translation increased in both specimens by 4.67 and 2.84 mm in oks003 and oks008, respectively. oks003 showed a 1.5 mm shift in initial A-P alignment and both specimens had the highest posterior shift at 90° flexion (Figure 2 and 3).

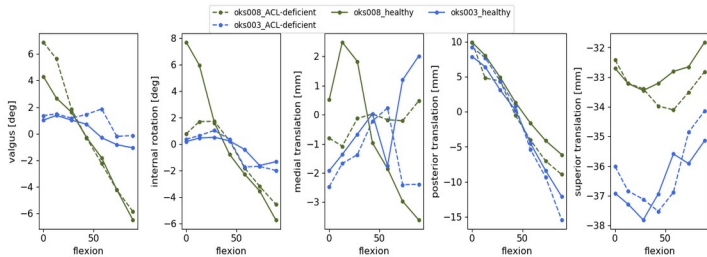


Figure 2. Predictions of knee motion during passive flexion using rule-based framework for both healthy and ACL-deficient conditions for oks003 and oks008 specimens.

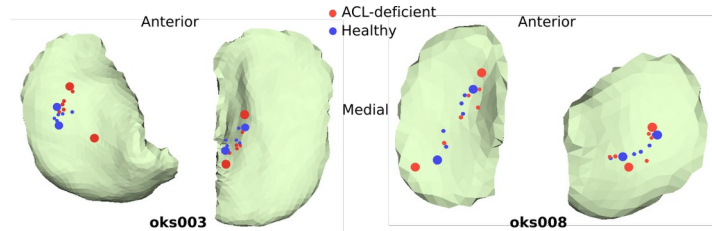


Figure 3. Contact center motion for both healthy and ACL-deficient states of the knee during passive flexion motion. Range of motion at each state is being highlighted by enlarged points.

CONCLUSION

In this study, a previously developed weighted rule-based framework was utilized to estimate subject-specific joint motion in ACL-deficient conditions for two specimens. The framework was developed using anatomical data alone to minimize rules related to the physiological function of the joint components, including ligament length covariance, anterior/posterior range of motion for medial and lateral contact, and penetration/separation of medial and lateral contact. Comparison between the kinematics of two specimens revealed important individual differences that can be lost in generic models of the knee. A similar trend of increasing A-P range of motion was observed in both specimens after ACL resection.

In order to accurately assess the suitability of the rule-based framework and the current sets of implemented rules for the analysis of ACL-deficient condition, further comparisons of the results with either physics-based model or experimental data are required. Moreover, expanding the study into additional specimens can better inform engineers and clinicians on the mechanism surrounding ACL injury across the population.

ACKNOWLEDGMENT

Funded by the NIH, grant R01EB024573.

REFERENCES

1. L. S. Lohmander et al., Am. J. Sports Med., 2007
2. B. D. Beynnon et al., Am. J. Sports Med., 2005
3. F. G. Girgis et al., Clin. Orthop., 1975
4. L. Blankevoort et al., J. Biomech., 1996
5. J. A. Ewing et al., J. Orthop. Res., 2016
6. N. Abdollahi Nohouji et al., ORS conference, 2020
7. <https://simtk.org/projects/openknee>.

THE EFFECTS OF FREEZING AND REFRIGERATION ON THE REPEATABILITY OF HUMAN SKIN MECHANICAL BEHAVIOR

Ellen Klonowski, Erica Neumann, Snehal Chokhandre, Ahmet Erdemir

Department of Biomedical Engineering, Lerner Research Institute, Cleveland Clinic, Cleveland, OH, USA
e-mail: klonowe@ccf.org

INTRODUCTION

Characterizing tissue properties of human skin is necessary to understand its mechanical role. Skin is an anisotropic, viscoelastic, and nonlinear material, making reliable characterization a challenge. Reported material properties vary greatly based on many factors including age, thickness, and orientation of the skin [1]. When testing cadaver skin *in vitro*, freezing and refrigeration of tissue samples are unavoidable, possibly contributing to uncertainties in characterization. Therefore, the goal of this study was to determine the effects of multiple freeze-thaw or refrigeration cycles on cadaver skin mechanical properties. The results from this study will inform future testing for building a cohort of specimen specific skin properties utilized for open source models of musculoskeletal extremities [2].

METHODS

Skin samples from a fresh, frozen cadaver leg (47 year old African American male, BMI: 24) were dissected (50mm x 100mm rectangular regions). After dissection, the sections were frozen until

tensile testing. Next, the anterior upper leg section was thawed at room temperature and hydrated using saline. Two adjacent test samples were manually cut into strips along the longitudinal axis of the leg (target dimension of 5mm x 25mm) using a scalpel. Each sample was secured in clamps using tissue adhesive. The sample width was recorded using a ruler and the thickness was measured optically using an in house device.

Samples were tested under cyclic loading conditions (Figure 1). The test protocol includes a sequence to find the reference length of the specimen by loading it to 25 grams (used to calculate strain and strain rate). Next, the sample is loaded to 15% strain at 20%/s, followed by 1000 preconditioning cycles at 2 Hz (10-15% strain). Finally, a second ramp to 15% strain was performed after finding a new reference length. Testing was performed at room temperature. Data was acquired at 2.5 kHz using a 10kg load cell (ATI Industrial Automation, USA) on a mechanical tester (Mach 1, Biomomentum Inc, Canada). After the test, the sample (still in clamps) was immediately removed from the machine, wrapped in a saline soaked paper towel and placed in a sealed plastic bag. Between tests, one sample was frozen (-20°C) and the other refrigerated (4°C).

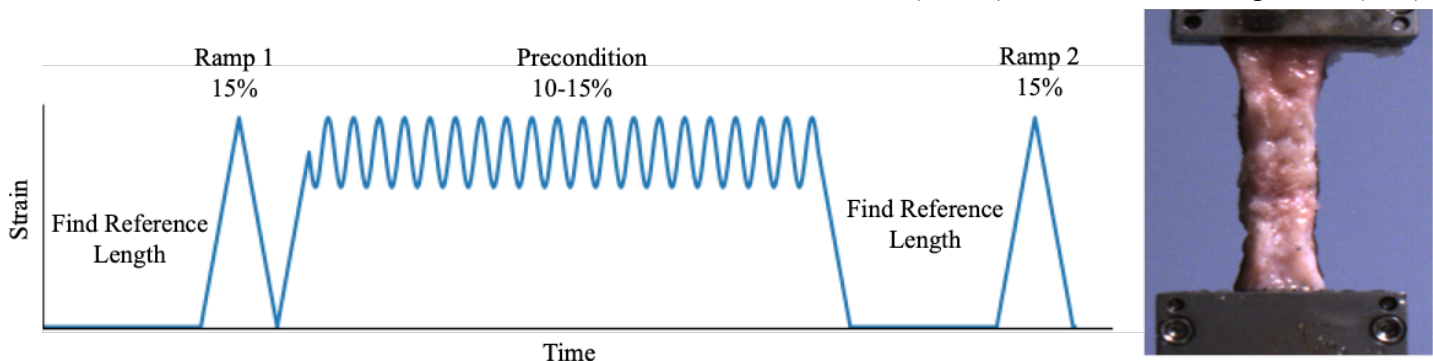


Figure 1: Tensile test protocol (left) and skin sample in clamps (right). Note: Only 20 preconditioning cycles are shown.

The same test protocol was completed every 20-24 hours for 6 days.

A Python script was used to process force-displacement data to determine stress and strain. Force data was filtered at 20 Hz using a low-pass third order Butterworth filter. The modulus was calculated from the slope of the stress-strain curve of ramp 2 in the linear region (defined from 10% strain to maximum load). Percent difference among moduli determined the repeatability between tests on the same sample. Differences less than 10% between sequential tests are considered repeatable for modeling applications.

RESULTS AND DISCUSSION

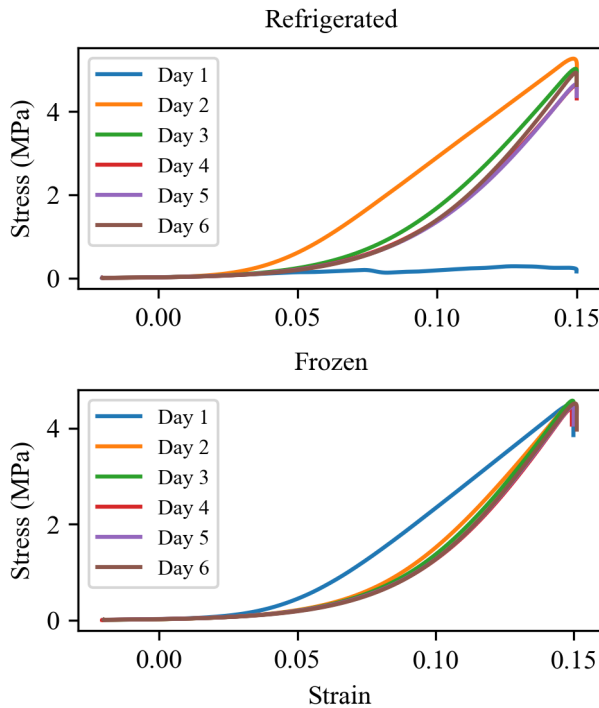


Figure 2: Stress-strain curves for both samples.

The stress-strain relationship of samples is shown in Figure 2. The mechanical behavior of the samples stabilized (day 2: frozen, day 3: refrigerated) as the percent differences suggest that freeze-thaw or refrigeration cycles do not contribute to variation in reported moduli (Figure 3). The refrigerated sample resulted in very low stress on Day 1, indicating that we were unable to load the sample appropriately. Day 1 (frozen) and day 2 (refrigerated) tests showed

distinct differences compared to the remaining trials. This could be due to long term conditioning of the samples throughout the whole test-retest workflow. Figure 3 shows change in modulus and reference length for each sample. Overall, the results suggest that at least 3 tests are needed to achieve moduli within the repeatability threshold.

CONCLUSIONS

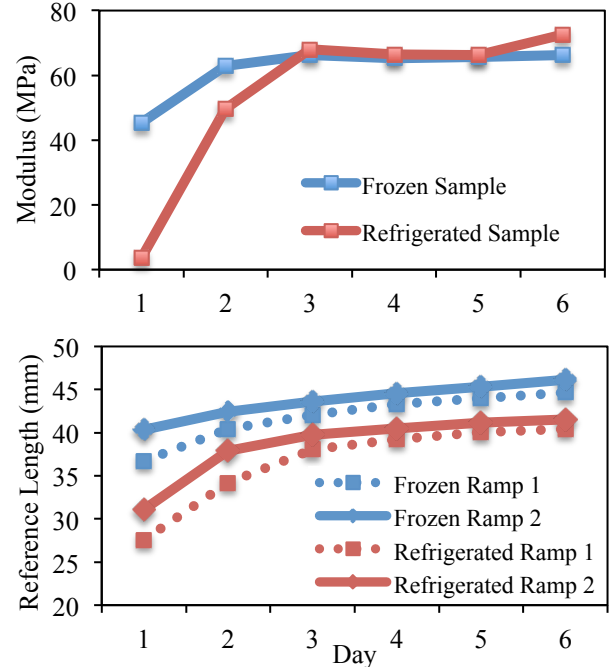


Figure 3: Change in modulus and reference length.

The experiment provides a repeatable protocol to determine whether freezing or refrigerating skin multiple times affects the mechanical stiffness of the tissue. The adjacent samples resulted in similar moduli. An obvious limitation of this study was the sample size, but will be expanded upon with further testing. This study suggests that cadaver skin specimens from a cohort of extremities can repeatedly be characterized despite undergoing multiple freeze-thaw cycles.

REFERENCES

- [1] Annaaidh, A, et al. JMBBM. 139-148, 2012.
- [2] Schimmoeller, T, et al. Sci Data. 20, 2020.

ACKNOWLEDGMENTS

USAMRMC (W81XWH-15-1-0232)

MODULATION OF SPINAL STRETCH REFLEXES IN THE LOWER EXTERMITY WITH REPEATED POSTURAL PERTURBATIONS: A PRELIMINARY ANALYSIS

¹Dong Jae Park, ¹Tyler Wood, ²Samuel J. Wilson, ³Harish Chander, ¹Christopher M. Hill*

¹Northern Illinois University, DeKalb, IL, 60115, United States

² Georgia Southern University, Statesboro, GA 30460, United States

³Mississippi State University, Mississippi State, MS 39762, United States

Email: chill8@niu.edu*

INTRODUCTION

Automatic postural responses are the first line of defense against environmental distributions to postural equilibrium. Rapid adaptation of the neuromuscular system's reactive and anticipatory mechanisms to novel perturbations decreases the possibility of fall and musculoskeletal injury [1]. In order to have the proper neuromuscular response to these disruptions, sensory afferents stimulate stretch reflex arcs to contract and relax lower extremity musculature in accordance with the direction of the disruptions. Previous literature has demonstrated a decrease in muscular co-contraction with repeated exposure to balance perturbations suggesting the adaptation of a feedforward control after initial exposure [2, 3]. However, this effect seems to be short-lived [4]. The collective evidence suggests that spinal stretch reflexes are modulated through feedforward control mechanisms when repeated exposed to balance disruptions; however, this possibility has yet to be tested. Thus, the purpose of this study is to examine the possible alterations to spinal stretch reflex arcs after multiple exposures to the same postural disruption over the course of several days.

METHODS

This study was conducted in a repeated measures design with eighteen healthy adults (8 male, 10 female age: 25 ± 4.73 years; height: 183.8 ± 8.5 cm; mass: 85.2 ± 15.6 kg) with no history of musculoskeletal, orthopedic, neurological, and vestibular abnormalities. Balance perturbations were delivered via a commonly used device in research and clinical settings, the Neurocom® EquiTTest®'s Motor Control Test (MCT). The largest anterior (FWL) and posterior (BWL) platform translations were selected for analysis, as they were most likely

to provide a sufficient stretch of the lower extremity muscles, thus the greatest spinal stretch reflex response. Data collection procedures included an initial familiarization that consisted of a single, full MCT. Following familiarization, participants performed five fully randomized MCTs over six testing sessions, in which they were not given knowledge of the direction or magnitude of the perturbations. The first five sessions occurred on consecutive days, with the sixth occurring two days after the fifth. Muscle activity was collected on medial gastrocnemius (Plantar Flexor-PF), tibialis anterior (Dorsi Flexor-DF), vastus medialis (Q) and semitendinosus (H) using the Noraxon TelemyoTM T2400 G2 wireless surface EMG system (Scottsdale, Arizona) with a sampling frequency of 1500 Hz. Raw EMG data was band-passed filtered between 20-250Hz and full wave rectified. To quantify spinal stretch reflex, mean muscle activity was taken 30-55ms after perturbation onset [5]. The first trial of a perturbation on each testing day was analyzed using a 1 (Participant) x 6 (Day) repeated measures ANOVA at an alpha level of 0.05 using SPSS v24.

RESULTS AND DISCUSSION

Spinal stretch reflex activity did not differ across testing days for the more proximal musculature of the lower extremity. No significant differences were detected across days for Q during the BWL perturbation [$F(2.363, 37.731) = 1.214, p = 0.312, \eta^2_p = 0.067$] or FWL perturbation [$F(2.212, 37.731) = 1.258, p = 0.291, \eta^2_p = 0.069$]. Similar findings were noted at for the H BWL perturbation [$F(1.094, 18.594) = 2.361, p = 0.140, \eta^2_p = 0.122$] or FWL perturbation [$F(2.212, 32.673) = 1.132, p = 0.303, \eta^2_p = 0.068$]. Similar findings were also found for the more distal muscles around the ankle. No significant

differences were detected across days for DF BWL [$F(1.892, 32.481) = 0.701$, $p= 0.624$, $\eta^2_p = 0.041$] or DF FWL [$F(1.892, 36.798) = 1.892$, $p= 0.104$, $\eta^2_p = 0.101$] (Figure 1). No significant differences were detected across days for PF BWL [$F(3.013, 51.219) = 0.933$, $p= 0.432$, $\eta^2 = 0.052$] or PF FWL [$F(2.826, 38.085) = 0.605$, $p= 0.696$, $\eta^2_p = 0.034$].

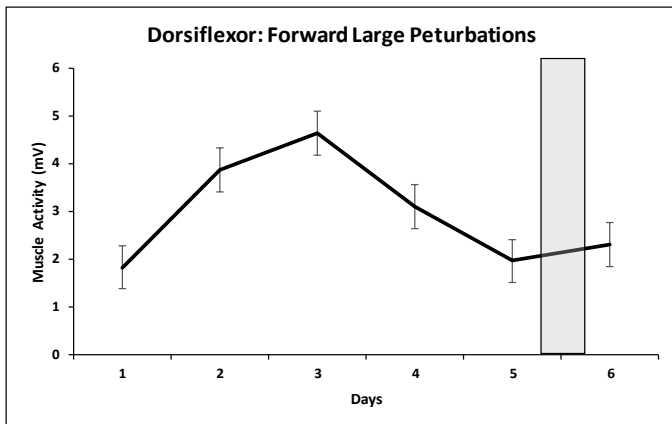


Figure 1: Mean muscle activity for the tibialis anterior (dorsiflexor) during the forward large perturbations over the six testing days. The shaded region represents the two-day retention period before the sixth day of testing. No significant differences were detected across days.

Previous studies documented changes to lower extremity muscle activity after repeated exposure to the same postural disruptions [2,4]. Upon examination of the spinal stretch reflex, which is the case of this study, a robust response was not found in the muscles of the lower extremity. Two possibilities remain as to why changes were not observed: 1. It was previously reported that reaction times did not change across repeated MCTs but overall muscle activation decreased [4]. This may mean the spinal stretch reflex contribution quantified in this study may operate with a similar level of sensitivity across days, but alters the associated efferent neurons in the stretched muscle to make the resulting contraction more efficient. In other words, afferent fibers detecting the muscle stretch do not change in their ability to detect and react to sudden platform translation, but repeated exposures changes only the associated efferent fibers. This would explain the changes in the overall muscle activation and the stable responses demonstrated in these data. 2. The methods used to access spinal stretch reflex was

developed initially in the study of arm perturbations [5]. Given the differences between lower extremity and upper extremity, such as motor control strategies of force development, it is possible this method of spinal stretch reflex quantification cannot be applied similarly.

CONCLUSION

This study did not provide evidence of changes to the spinal stretch reflex arc that has been suggested to occur prior studies. However, this study was exploratory in nature and requires further analysis to properly rule out the possibility of such modulation in the lower extremity resulting from repeated balance disruptions.

REFERENCES

- [1] Woollacott M. et al. *Gait & Posture*, 1-14. 2002.
- [2] Welch, T. & Ting., *PloS One*, 1-18, 2014
- [3] Winter, D. A., Patla, A. E., Prince, F., Ishac, M., & Gielo-Perczak, K. *J of Neurophy*, 1211-122, 1998.
- [4] Hill, C.M. et al., *J of Electomy Kin*, 96-102, 2018
- [5] Weiler et al., *Nat Neurosci*, 529-533. 2019

REPEATABILITY AND PRECISION OF A REMOVABLE AND MR-COMPATIBLE BONE-MOUNTED MARKER ASSEMBLY FOR IN VIVO MEASUREMENT OF JOINT BIOMECHANICS

¹Elise I. Baron, PhD, ¹Jillian E. Beveridge, PhD

¹Department of Biomedical Engineering, Lerner Research Institute, Cleveland Clinic, Cleveland, OH, USA

INTRODUCTION

The anterior cruciate ligament (ACL) is a critical structure in knee joint stability. Injury to the ACL and subsequent repair is associated with abnormal kinematics and high risk of developing osteoarthritis [1]. Changes in knee joint kinematics in a sheep model of ACL injury have correlated with increased osteoarthritis scores [2], and magnetic resonance imaging (MRI) T₂* relaxometry-based multiple linear regression models have shown to be predictive of ACL structural properties during the healing process [3]. The overarching goal of this project is to understand whether ACL graft remodeling modulates in vivo joint biomechanics in a way that increases the risk of post traumatic osteoarthritis in a porcine model [4] of ‘idealized’ ACL surgery [5]. To accomplish this, traditional motion capture will be used to record joint biomechanics (based on previously defined ovine model [6]), and MR imaging will be used to estimate mechanical properties of the healing ACL after surgery. To quantify joint motion accurately, markers will be attached to the bone via previously implanted bone plates (Figure 1). A positional relationship will be established between the bone and the attached markers by aligning a model of the engineered plate to the implanted plate in an MR image via a registration grid. Here, we describe the design framework of the implantable post and removable marker assembly and grid registration, and quantify the repeatability of the assembly fit in vitro.



Figure 1. Illustration of implantable plate and removable marker assembly on femur and tibia.

METHODS

In order for the design to be considered successful, the implantable plate-marker assembly had to be: biocompatible, MRI compatible, non-reabsorbing, rigid, contain an MR-visible asymmetrical registration grid, and yield a measurement uncertainty of less than 1.0mm based on previous work in an ovine model of ACL injury [2].

Prototype plates were machined from a biocompatible resin (UltemTM) and were implanted in cadaveric porcine hind limbs. The detachable marker assembly was 3D printed and spheres (4) were covered with retroreflective tape. Ten surface points were collected for each spherical marker with a Microscribe coordinate measuring machine (Revware, Raleigh, NC) and a sphere was fitted to each set of points with 3-matic software (Materialise, Leuven, Belgium). Marker assembly sphere centroid locations were expressed as vector magnitudes relative to the origin of the Microscribe global

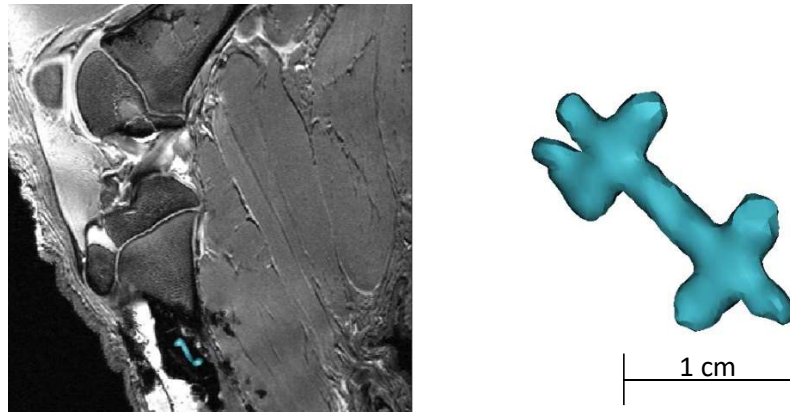


Figure 2. MRI image of porcine knee with plate implanted on the tibia, registration grid in blue (left). 3D object of registration grid segmented from MRI image (right).

coordinate system. Detachment/reattachment repeatability of the marker assembly was quantified as the standard deviation of marker centroid locations after five detachment/reattachments to the rigidly fixed bone plate. MR visualization of the registration grid was deemed acceptable if the entire 3D grid could be segmented from the MR images. The anatomical coordinate systems of the porcine femur and tibia were additionally defined from MR images.

RESULTS AND DISCUSSION

After several iterations of plate-marker prototype design, UltemTM was chosen for the implantable plate manufacturing, and PEEK screws were used to attach the plate to the bone. Preliminary MR imaging revealed no image artifact from the plate materials and visualization of the registration grid proved successful (Figure 2). Marker assembly repeatability testing revealed that the standard deviations of the centroid vector magnitude range from 0.12 – 0.21mm (0.16 average).

Human bone-based coordinate systems used to calculate the joint biomechanics were modified to reflect the functional axes of the porcine femur and tibia, which will be used to calculate joint kinematics.

Future work:

Quantification of the MR-based grid registration is ongoing. Upcoming in vivo pilot studies will assess feasibility and repeatability of collecting knee kinematics during treadmill gait, and MRI metrics of the native, intact ACL and adjacent tibiofemoral cartilage.

CONCLUSIONS

Preliminary testing suggests that the implantable plate and removable marker assembly meets our a priori design criteria, and will therefore provide a reliable approach to record tibiofemoral bone kinematics in vivo.

REFERENCES

- [1] Kiapour AM, Murray MM. *Bone Joint Res*, 3(2), 20–31, 2014.
- [2] M. Shekarforoush *et al.*, *Ann. Biomed. Eng.*, 47(3), 790–801, 2019.
- [3] J. E. Beveridge, *et al.*, *J. Orthop. Res.*, 36(6), 1701–1709, 2018.
- [4] B. L. Proffen, M. McElfresh, B. C. Fleming, and M. M. Murray, *Knee*, 19(4), 493–499, 2012.
- [5] Heard, B.J., Achari, Y., Chung, M., Shrive, N.G. and Frank, C.B.. *J. Orthop. Res.*, 29: 1185-1192, 2011.
- [6] J. E. Tapper, *et al.*, *J. Biomech Eng, Technical Briefs*, 126(2), 301-305, 2004.

ACKNOWLEDGEMENTS

This work was supported by NIH/NIAMS R00AR069094 and The Cleveland Clinic seed funding.

Multi-Scale Wearable Sensing for Movement and Gait Analysis

¹Loubna Baroudi, ¹Mark Newman, ²Elizabeth Jackson, ¹Kira Barton, ¹Alex Shorter, and ¹Stephen Cain

¹University of Michigan, Ann Arbor, MI, USA

²University of Alabama, Birmingham, AL, USA

Email: lbaroudi@umich.edu

INTRODUCTION

Technological advancements in wearable sensing and algorithm development enable new opportunities to inform health care decisions and provide a more complete picture of an individual's health and activity during daily life. However, implementation of new advancements in wearable sensing for clinical decision making has been limited due to many factors, which include time constraints imposed by current clinical practices, subject compliance, and knowledge barriers that exist between engineers, scientists, clinicians, and patients. As a result, simple assessments (e.g. 5-meter walk test) tend to be used to inform clinical decisions. While these simple gait assessments are trusted by clinicians, it is not clear in the literature how well a single metric like gait speed is representative of activity during daily life or is able to capture overall physical activity level. Therefore, the goal of this work is to create an approach that will utilize both fine-scale measurements from an array of wearable sensors and low-resolution long-term wearable devices to estimate gait speed across different time scales through novel analysis algorithms. Our first objective was to assess the influence of the walking environment (e.g. indoor versus outdoor) on gait parameters that can be extracted from the collected data. The second objective was to investigate how existing technologies can be leveraged for persistent (long-term) monitoring to estimate clinically relevant parameters over days or weeks.

METHODS

We propose a smart wearable sensing system that combines physiological and kinematic data from participants during activity at short (minutes), medium (hours), and long (days) timescales. During the short and medium timescales, data from inertial measurement units (IMUs) on the feet and body,

heart rate, and blood oxygen saturation measured at the gastrocnemius were used to quantify gait and activity during structured and free movement. During the short evaluation, participants performed standard clinical assessments of gait and activity: 5-meter walk, 6-minute walk, Berg Balance Scale, quiet standing, grip strength, and the sit to stand assessment. During the medium evaluation, participants completed both a supervised 'long walk' through buildings and outdoor spaces, and an unsupervised half-hour of activity. During the unsupervised time, the participants were given suggestions of where to walk on campus but were free to use the time as they saw fit. Steady-state gait parameters from these assessments were used to assess activity. To complement these high-resolution short and medium timescale measures, participants were sent home with an accelerometer-based archival sensor secured to their thigh (activPAL). Acceleration data from the activPAL was used to classify activity state (lying, sitting, standing, stepping and cycling; via activPAL algorithms) and to extract gait parameters (step frequency, gait symmetry, and statistical features). All protocols used off-the-shelf wearable sensors and were approved by the Institutional Review Board at the University of Michigan.

RESULTS AND DISCUSSION

For the 5-meter walk test, the 6-minute walk test, the long walk, and the week of observation, the number of steps collected is approximately 10, 300, 700, and 10 000, respectively.

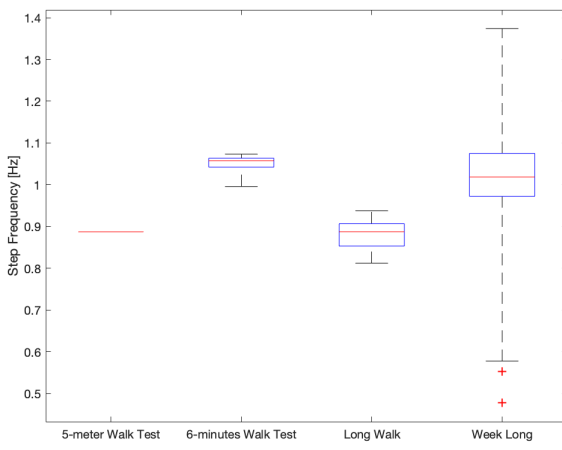


Figure 1: Box plots of the step frequencies extracted from the different data collections.

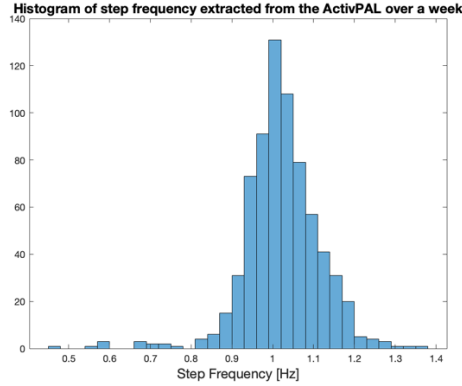


Figure 2: Distribution of step frequencies estimated from the activPAL data for a sample week long data collection.

Step frequency is a feature of interest since it can be linked to gait speed [1,2]. Figure 1 illustrates that longer timescales capture more variation in the step frequency of a representative subject and reveals the different median step frequencies for different timescales. Figure 2 illustrates the range of step frequencies used during a week for a sample subject, estimated using raw acceleration data from the activPAL.

Using the data from the short and medium timescales, we are able to derive a model of the relationship between stride speed and stride length as shown in Figure 3. Using this model we can derive the model that enables estimation of walking speed from step frequency.

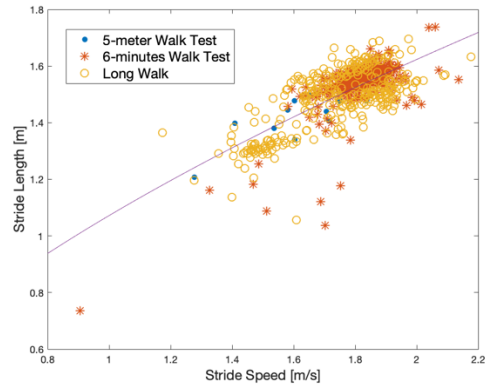


Figure 3: Predicted speed-step length relationships of a representative individual:
 $\text{stride length} = 1.072 * \text{speed}^{0.5986}$

CONCLUSION

Using the rich data extracted from a wearable sensor suite across different temporal timescales and resolutions, we evaluate how each sensor can be used to characterize gait across different environments. We also quantify the relationships between information collected in a controlled environment and information collected during free-living activities to draw appropriate conclusions from the data.

REFERENCES

1. Kuo, A, et al. *Journal of Biomechanical Engineering*, Pages 264-269, 2001.
2. Berthram, J, *Journal of Theoretical Biology*, Pages 445-453, 2001.

ACKNOWLEDGEMENTS

This research was supported by a grant from the University of Michigan Precision Health Initiative. 2020 Midwest Regional American Society of Biomechanics Meeting, Cleveland, OH, USA, April 8th-April 9th, 2020

Detection of Locomotion Deficits in a Post-Traumatic Syringomyelia Rat Model Using an Automated Gait Analysis Technique

¹Dipak D. Pukale, ²Mahmoud Farrag, ^{1,2,*}Nic D. Leipzig

¹Department of Chemical and Biomolecular Engineering, University of Akron, Akron, OH, USA 44325

²Integrated Biosciences Program, University of Akron, Akron, OH, USA 44325

Tel.: +1-330-786-8443; E-mail address: dp130@zips.uakron.edu

INTRODUCTION

Syringomyelia (SM) is a neurological disorder that is characterized by the formation of a fluid-filled cyst, a syrinx, inside the spinal cord. It is a common coincidence with multiple neurological diseases such as Chiari malformation I, trauma, and several other disorders. SM associated with spinal cord injury (SCI) is called post-traumatic SM, and it develops in about 21-28% of people with SCI. It is not always easy to track the triggering trauma, as it sometimes results from minor injury and takes months to years to fully develop, making it challenging to prevent. SM presents mainly with chronic progressive pain and neurological deficits because syrinxes compress the surrounding neural tissue while expanding, negatively impacting patient quality of life. The current treatment options for SM are mainly surgical interventions such as shunting, duraplasty, adhesiolysis, or decompression. Even though surgical treatments are standard options to treat SM, due to surgical complications and their higher failure rate (>80%), these options don't provide enough confidence to clinicians to treat SM permanently [1, 2].

The purpose of the present study was to determine the detectability of locomotion deficits due to syrinx formation or expansion/elongation in the spinal cord in a PTSM rat model using the GAITOR technique. Since PTSM or other SM animal models are non-severe and indirect, there is no technique, to the best of our knowledge, reported in the literature to detect functional outcomes in terms of motor or sensory. So, this is the first attempt to explore the arena of detecting functional outcomes in an SM animal model. The findings from this

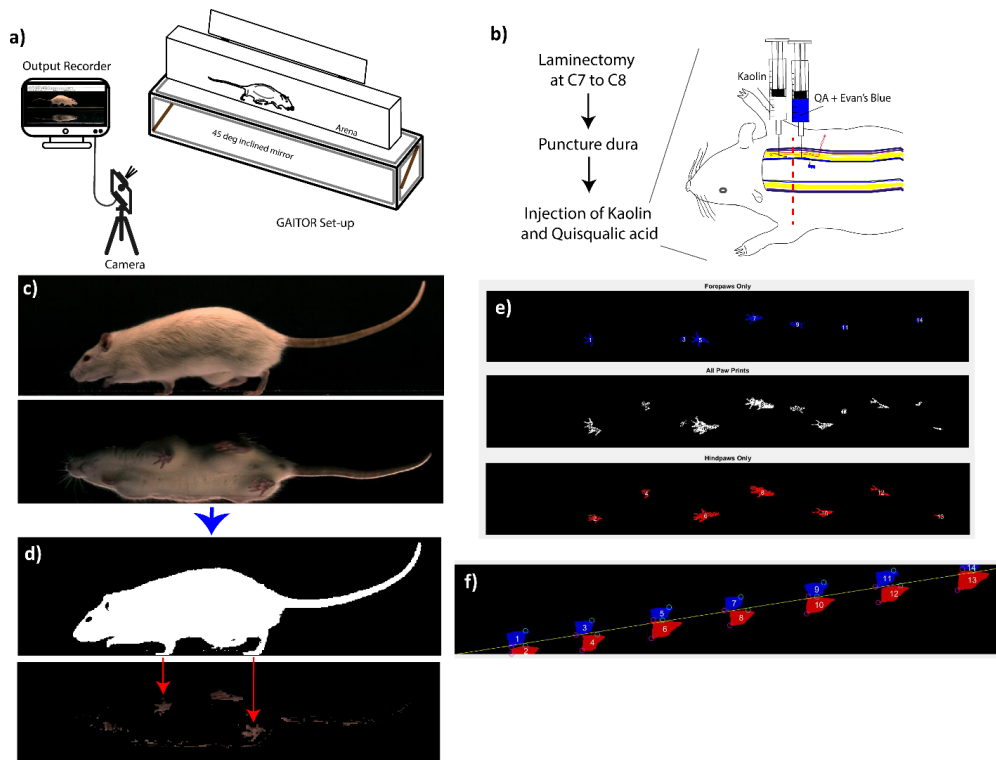


Figure 1. GAITOR Set up, injury model and overview of GAITOR analysis. a) Schematic representation of the GAITOR set up, it includes two components: arena of the clear acrylic enclosure where rats walk freely back and forth unprompted, and a 45° mirror placed below to view sagittal and ventral planes. A high-speed camera captures videos of rats walking on the arena. b) schematic representation of the PTSM injury at C7- C8 level of the spinal cord which potentially impacts forelimb as well as hindlimb movement to some extent by forming syrinxes in the spinal cord. c) A representative frame of a GAITOR video showing a sagittal and ventral view of the rat. d) AGATHA software filters rat and paws from the background in the sagittal and ventral view respectively. e) Pawprint images of forepaws, hind paws and combined generated for each video. f) Plots of forepaws (blue) and hind paws (red) showing foot stride (green circle) and toe-off (pink circle) generated for every video.

study will be useful to facilitate SM research to find better treatments, diagnoses, etc.

METHODS

Automated gait analysis

The detailed description and of instrumentation and AGATHA software have been explained previously, and detailed SCI-specific parameters were discussed in refs. [3, 4, 5]. In short, the GAITOR set up comprises of two parts, an arena where rats walk back and forth unprompted while video being recorded using high-speed camera and 45° inclined mirror to capture the ventral view of the rat walking on the arena as shown in Fig. 1 (a). The software part of the technique, AGATHA filters the rat in

the sagittal view and the paws in the ventral view from the background. AGATHA provides the capability to exclude the regions where the rat touches to the arena surface other than paws such as for the nose or tail. It determines the foot-strike toe-off (FSTO) diagram based on the earliest (foot-strike) and last (toe-off) frames in which a paw is in contact with the arena surface as shown in Fig 1 (f). AGATHA calculates temporal parameters such as duty factor imbalance, phase dispersion and spatial parameters such as paw placement accuracy, step width, stride length which provide locomotive information of the animals walking on the arena.

RESULTS AND DISCUSSION

The animals that received PTSM injury showed locomotion deficits compared to naïve animals in terms of duty factor imbalance, paw placement accuracy, step contact width, stride length, and phase dispersion (Fig. 2).

CONCLUSIONS

To summarize, we have shown that the capability of GAITOR with AGATHA to detect locomotion deficits caused due to presence of syrinxes in PTSM rats despite

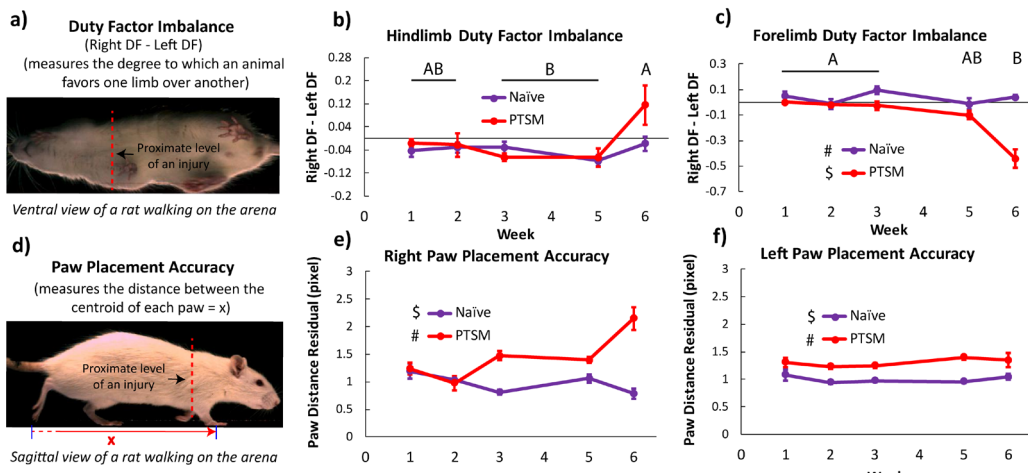


Figure 2. PTSM injury affects the **duty factor imbalance of the forelimb and paw placement accuracy** of both right and lefts paws. a-c, Duty factor imbalance. a) the definition of duty factor imbalance. b) Hindlimb duty factor imbalance is unaffected by the syrinxes present in the spinal cord due to PTSM injury, whereas c) forelimb duty factor imbalance got affected by the injury model. d-f, paw placement accuracy. d) definition of paw placement accuracy is presented pictorially. Syrinxes present in the spinal cord due to injury greatly affected the right (e) as well as left (f) paw placement accuracy. However, there is no significant difference at the different time points from week 1 to week 6. For all graphs, data are presented as mean \pm standard error, for naïve group n=6, and for PTSM group n=9, for both groups subsamples (videos) s=3 to 6. Letters and symbols denote statistical significance as determined by the two factors ANOVA with Tukey's post hoc ($p<0.05$)

being an indirect and non-severe injury. The results presented in this study in terms of duty factor imbalance,

paw placement accuracy, step contact width, stride length, and phase dispersion conclude that PTSM injury significantly and detectably impacted the locomotor activities of the forelimbs, indicating the syrinx presence in the cervical level of the spinal cord. This introduces a new functional analysis technique is the first attempt to capture locomotion deficits due to SM and will be useful for harnessing further treatment development strategies for SM in the near future.

REFERENCES

- [1] A.R. Brodbelt, M.A. Stoodley, Post-traumatic syringomyelia: a review, *J Clin Neurosci* 10(4) (2003) 401-8.
- [2] A. Agrawal, M.S. Shetty, L. Pandit, L. Shetty, U. Srikrishna, Post-traumatic syringomyelia, *Indian J Orthop* 41(4) (2007) 398-400.
- [3] H.E. Kloefkorn, T.R. Pettengill, S.M. Turner, K.A. Streeter, E.J. Gonzalez-Rothi, D.D. Fuller, et al., Automated Gait Analysis Through Hues and Areas (AGATHA): A Method to Characterize the Spatiotemporal Pattern of Rat Gait, *Ann Biomed Eng* 45(3) (2017) 711-725.
- [4] B.Y. Jacobs, E.H. Lakes, A.J. Reiter, S.P. Lake, T.R. Ham, N.D. Leipzig, et al., The Open Source GAITOR Suite for Rodent Gait Analysis, *Sci Rep* 8(1) (2018) 018-28134.
- [5] T.R. Ham, M. Farrag, A.M. Soltisz, E.H. Lakes, K.D. Allen, N.D. Leipzig, Automated Gait Analysis Detects Improvements after Intracellular sigma Peptide Administration in a Rat Hemisection Model of Spinal Cord Injury, *Ann Biomed Eng* 47(3) (2019) 744-753.

ACKNOWLEDGEMENTS

The authors would like to thank Dr. Trevor Ham for the training and guidance on GAITOR/AGATHA technique and help in data processing and Ms. Eleanor Plaster for assistance in video processing. We would like to thank Conquer Chiari and Column of Hope for the financial support for this study.

CHANGES IN FRONTAL PLANE MOTION AND FREQUENCY CHARACTERISTICS IN CHRONIC STROKE SURVIVORS FOLLOWING GAIT THERAPY

Jiafeng Song¹, Jessica P. McCabe², Margaret Skelly², Svetlana Pundik^{2,4}, and Elizabeth C. Hardin^{1,3}

¹Department of Biomedical Engineering, Case Western Reserve University, Cleveland, OH

²Brain Plasticity & NeuroRecovery Lab, Cleveland FES Center, Cleveland VA Medical Center

³Human Performance Virtual Reality Lab, Cleveland FES Center, Cleveland VA Medical Center.

⁴Department of Neurology, School of Medicine, Case Western Reserve University, Cleveland, OH

Email: jiafeng.song@case.edu

INTRODUCTION

Stroke survivors commonly experience unilateral lack of control in their lower limb joints (paresis). Impaired paretic limb motor control when walking can result in larger and varying limb displacement than normal in the frontal plane due to reliance on hip abduction for toe clearance during swing. This paretic limb displacement in the frontal plane can cause instability during walking, increases energy cost¹, and requires greater active balance control than anteroposterior displacement². The purpose of this study is to determine whether a novel gait therapy for stroke survivors can reduce the magnitude and variability of paretic limb displacement in frontal plane, as well as determine whether frequency characteristics of the limbs are modified.

METHODS

Following approval for the study from our Institutional Review Board, two stroke survivors were recruited. Subject A was a 72-year-old male (61 months post-stroke, height=1.83m, weight= 84.4kg) and Subject B was a 62-year-old male (150 months post-stroke, height=1.80m, weight=78.7kg). Both subjects had right leg paresis. They had 10 novel gait therapy training sessions plus baseline, mid-training, and post-training during which data were collected. Subject B had an additional post-training session three weeks after the end of training. Training was twice

weekly for five weeks. During the novel gait therapy, treadmill walking was performed at their preferred speed while shifting their center of gravity to the paretic leg, forcing its use during the weight bearing stance phase. For data collection, markers were mounted on right and left lateral malleoli (RLM, LLM). Passive marker motion capture was performed at 100 Hz (Vicon, Oxford, UK), three-dimensional marker coordinates were calculated, and frontal plane motion was analyzed for both unaffected and paretic legs. Coefficient of variation (COV) and standard deviation were calculated to determine the variability during the training sessions. The frontal plane motion was also transformed into the frequency domain to determine the frequency characteristics.

RESULT AND DISCUSSION

For both subjects, the paretic leg had greater frontal plane displacement than the unaffected leg (Figure 1). Displacement mean values varied throughout the sessions. The displacement range and standard deviation decreased over time. From baseline to post-training sessions, the COV decreased in the unaffected leg (56% to 39%, Subject A; 30% to 26%, Subject B), and in the paretic leg (22% to 20%, Subject A; 46% to 32%, Subject B). In the frequency domain both legs had frequency correspondence, with greater peak magnitudes in the paretic leg. Training caused shifting to lower frequencies.

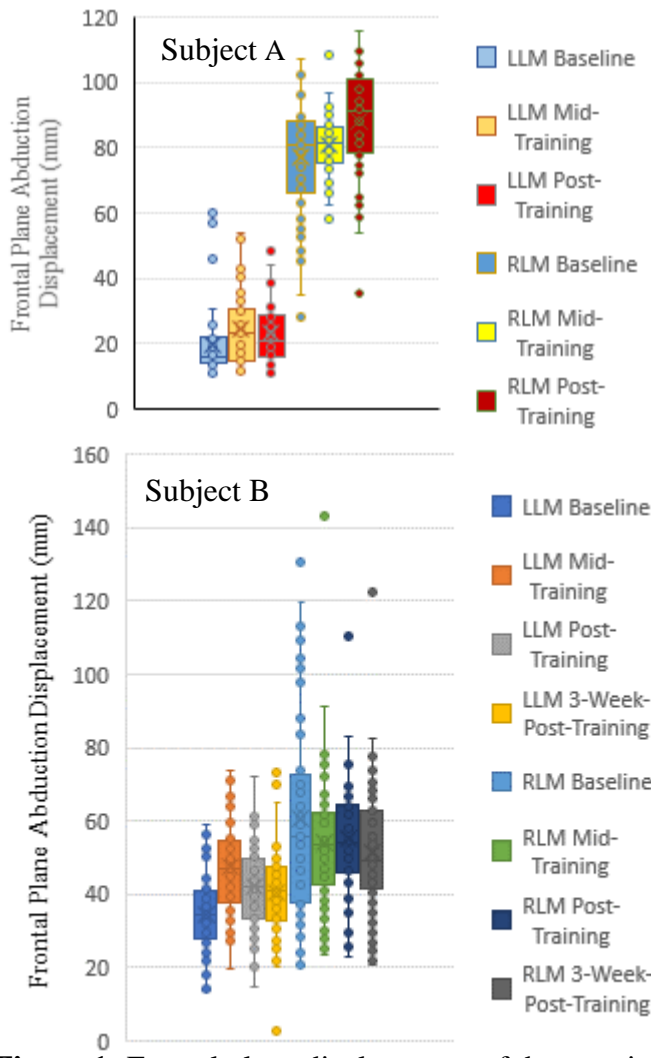


Figure 1: Frontal plane displacement of the paretic (RLM) and unaffected (LLM) legs during the evaluation sessions for the subjects.

CONCLUSION

The study demonstrates that the novel gait therapy was effective in reducing variability of frontal plane limb displacement in both limbs, but did not reduce the magnitude. The shift to lower frequencies after training could be an indication of greater endpoint control. In addition, fatigue may have a critical influence on variability of lower limb frontal plane motion, which needs further study and evidence to support.

REFERENCE

1. Chen, G, et al. Gait Posture 22 (1), 51–56, 2005
2. O'Connor, S. J. Neurophysiol, 1411-9, 2009.
3. Highsmith, M, et al. Technol Innov, 99-113, 2016.

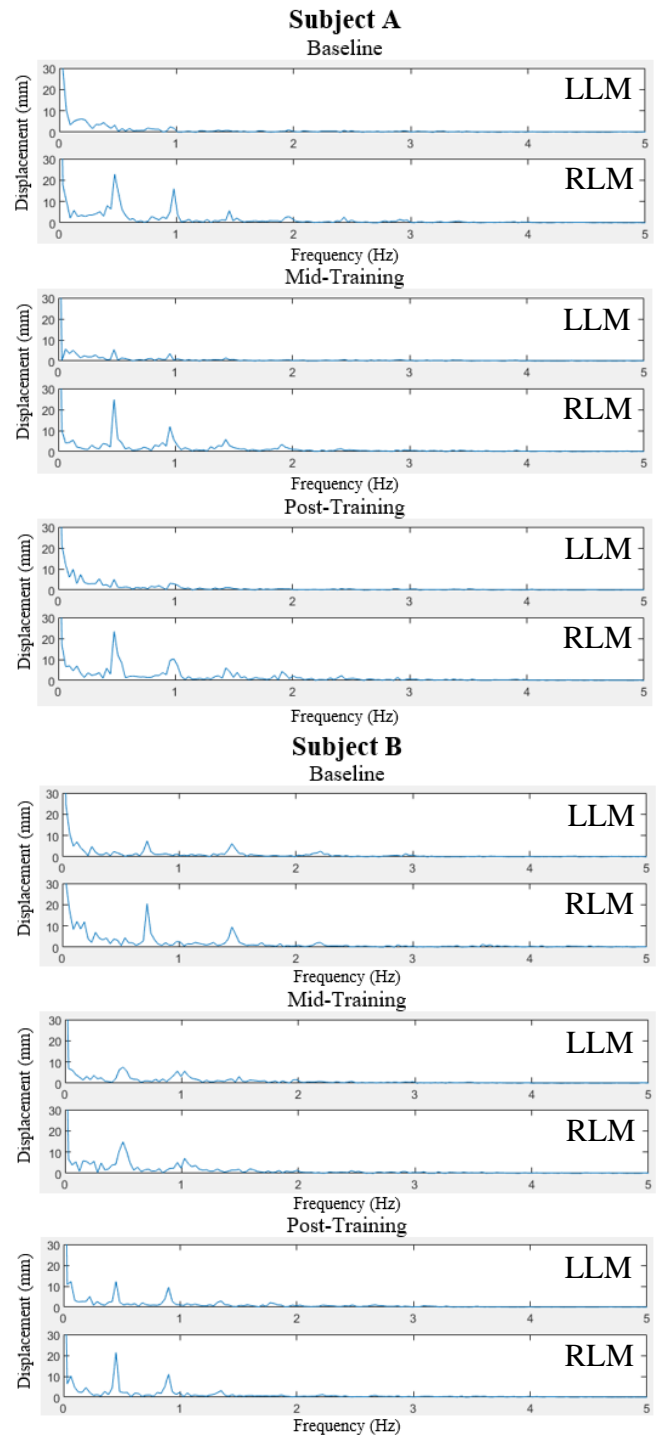


Figure 2: Paretic (RLM) and unaffected (LLM) legs frequency domain characteristics during the evaluation sessions for the subjects.

ACKNOWLEDGEMENTS

We gratefully acknowledge our funding from the Department of Veteran's Affairs (Merit Review award, Pundik).

A TREADMILL GAIT PERTURBATION BIOMECHANICAL ASSESSMENT FOR POST STROKE REHABILITATION

¹ Hala Osman MS, ²Antonie J. van den Bogert PhD, and ³Ann Reinalth PT PhD, ³ Debbie Espy PT PhD

¹ Cleveland State University, Department of Biomedical Engineering, Cleveland, OH, USA

² Cleveland State University, Department of Mechanical Engineering, Cleveland, OH, USA

³ Cleveland State University, College of Sciences and Health Professions, Cleveland, OH, USA

Email: h.osman@vikes.csuohio.edu

INTRODUCTION

Falls are the most common and costly medical complication for those who have had a stroke. Community dwelling stroke survivors show a high risk of falls with unexpected external perturbations during walking. Fear of falling is one of the problems that stroke survivors encounter daily. Regaining balance after stroke is thus imperative. When a person is destabilized by a sudden shift of balance from an impact to their body during gait, the body responds in an effort to recover its balance; this is known as gait perturbation.

Previous studies have established the importance of compensatory stepping to restore dynamic stability in response to perturbations among hemi-paretic stroke survivors because the paretic-side has difficulty executing a successful stepping response.

Measurement of gait stability is important in that it offers crucial information for establishing the level of functional limitations, whether due to pathology such as among a stroke population, or in evaluating rehabilitation exercise intervention effects.

Despite the number of studies that focus on gait stability, ways to quantify dynamic stability of human gait are still not fully clear. Thus, the purpose of this work is to develop gait perturbation based biomechanical assessment tools for a poststroke population. This offer both engineers and physical therapists a quantitative approach to assess directly fall resistance and balance strategies accurately.

METHODS

Walking balance, pre- and post-intervention, were tested by a progressive belt speed perturbation protocol on an instrumented treadmill (Fig. 1). Optical motion capture was used to obtain 3D full body kinematics.



Figure 1: Experimental setup

The participant performed a sequence of fifteen 90-second walking trials, consisting of normal walking speed, a perturbation period, and a recovery period. Both self-selected normal and maximum walking speeds were measured in meters per second. A perturbation was applied once per trial at mid-stance of the non-paretic limb during a randomly selected gait cycle within the perturbation period. The intensity of the external perturbation was initially determined as the percentage of participant's maximum walking speed and increased or decreased

based on success or failure of recovery, as determined from an instrumented harness.

RESULTS AND DISCUSSION

This work is currently in progress and these results are preliminary. Our results showed improved characteristics of gait velocity (Table 1) and fall/recover trials (Table 2) from pre- to post-intervention.

Table1: Gait velocity measurements before and after intervention.

Participants	Pretest		Posttest	
	NWS [m/s]	MWS [m/s]	NWS [m/s]	MWS [m/s]
1	0.70	0.93	0.85	1.20
2	0.25	0.40	0.30	0.50
3	0.40	0.55	0.48	0.65
4	0.25	0.35	0.25	0.40

NWS: normal walking speed; MWS: maximum walking speed

Gait velocity offers helpful information about the functional ability and physical condition of individuals.

Table2: Falls and recoveries trial measurements before and after intervention.

Participants	Pretest		Posttest	
	Fall	Recovery	Fall	Recovery
1	4	8	3	11
2	0	11	0	15
3	1	12	0	14
4	1	13	0	14

The perturbation was generated at the specified time (mid-stance), under the non-hemi-paretic leg, in a random gait cycle, and generated a participant response that can be quantified. The effect of perturbation is noticeable as shown as an increase in vertical force and high knee flexion. The right foot is lifted quite high after the perturbation to make a recovery step. Participants demonstrated varying ability to respond to both; small and large perturbations (Fig. 2).

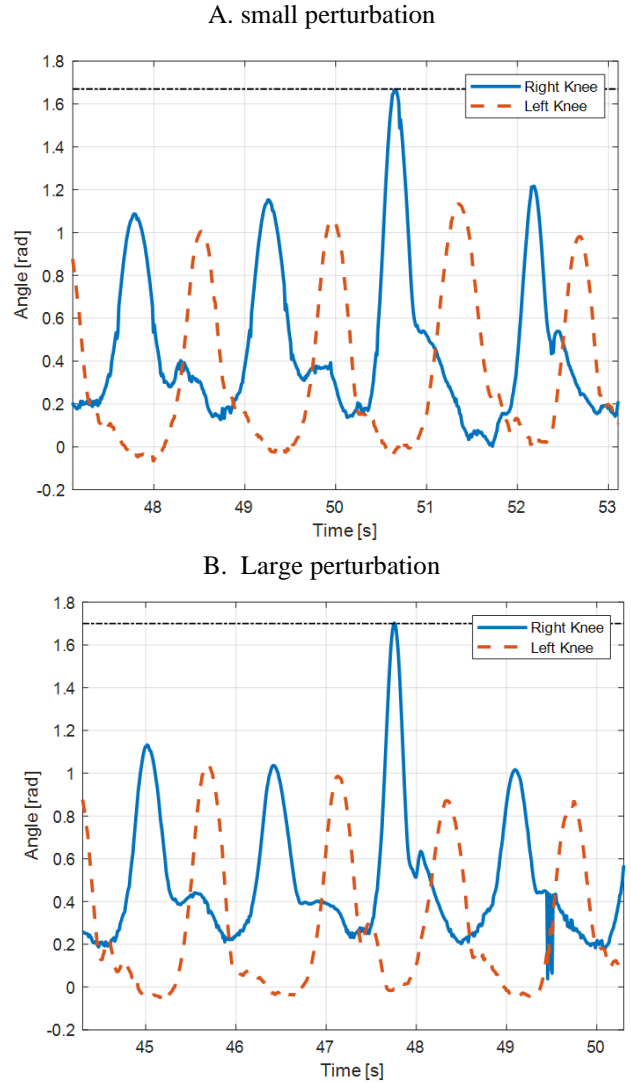


Figure 2: Illustration of perturbations responses for the knee angle joints results for left side hemi-paretic stroke participant.

CONCLUSION

The developed method is functional for people who have had a stroke. Gait perturbation-based assessment could be used as a potential proxy for real-world falls for individuals poststroke. Fall - resistance assessment for people post stroke is clinically essential given that falls have a high incidence.

ACKNOWLEDGEMENTS

This work has been and supported by the American Heart Association.

KINEMATIC CONSIDERATIONS FOR INERTIAL MEASUREMENT UNITS

Andrew D. Shelton¹ (Presenter), Joseph W. Mileski¹, Stephen M. Cain²,
and Louis A. DiBerardino III¹

¹Department of Mechanical Engineering, Ohio Northern University, Ada, OH, USA

²Department of Mechanical Engineering, University of Michigan, Ann Arbor, MI, USA

Email: l-diberardino@onu.edu

INTRODUCTION

Inertial measurement units (IMUs) are often used for research purposes in a variety of fields. Their wireless and mobile nature make them advantageous for data collection outside of a laboratory setting. IMUs measure acceleration and angular velocity, which is different from the measurements of position and orientation usually made with optical motion capture in traditional laboratory environments [1-3]. The relationships between accelerations, angular velocities, positions and orientation of a rigid body can be deduced using principals from engineering dynamics. However, utilizing these relationships to understand how IMU measurements are related to traditional biomechanical metrics is more difficult.

The aim of this work in progress is to show how these sensors function in line with the basics of rigid body kinematics and to lay out what researchers need to consider when using them for more advanced studies. While much of this information is seen as common knowledge to individuals with a strong background in engineering dynamics, literature often lacks a clear display of the fundamentals for those who have not seen them before.

METHODS

Given the linear acceleration, \bar{a}_A , of a point A on a rigid body, a second point B on the body has a linear acceleration given by

$$\bar{a}_B = \bar{a}_A + \bar{a}_{B/A}$$

where $\bar{a}_{B/A}$ is acceleration of B relative to A . For planar motion, $\bar{a}_{B/A} = \bar{\alpha} \times \bar{r}_{B/A} - \omega^2 \bar{r}_{B/A}$, where $\bar{\alpha}$ is the angular acceleration of the body, $\bar{r}_{B/A}$ is the position of B relative to A , and ω is the angular speed of the body. It is clear that $\bar{a}_A \neq \bar{a}_B$ unless they are the same point ($\bar{r}_{B/A} = 0$) or the body is not rotating ($\bar{\alpha} = \omega = 0$). It should also be noted that angular velocity and angular acceleration are the same at all points of a rigid body. These observations hold when extending to full three-dimensional motion as well.

The current work involved highlighting fundamental rigid body kinematics through the data collected from a set of Trigno IM sensors (Delsys Inc., Natick, MA). Utilizing a rod fixed to a hinged joint, these sensors displayed the fact that the location of the IMU is not important when measuring angular motion, but is very important when measuring linear motion. Two sensors were placed on the rod. The upper sensor was the primary sensor, from which the corresponding motion of the second sensor was derived using the above equations and compared to its recorded data. Data were collected and exported with EMGWorks (Delsys Inc.), then post-processed in MATLAB (MathWorks Inc., Natick, MA) and analyzed.

The angular velocity at both points on a rigid body are equal, so we compared the angular data obtained from each sensor, which should be the same neglecting noise. The linear acceleration can be calculated with the above equations, using the distance between sensors (measured physically) and the angular velocity and acceleration of the primary sensor. The calculated values were compared to the

actual linear acceleration data from the secondary sensor.

Currently, work is progressing on extending the methodology from planar to three-dimensional motion, including human movement, while comparing results to those from optoelectronic motion capture.

RESULTS AND DISCUSSION

Initial data from the two IMUs prove that linear acceleration is different and depends on location, while angular velocity is the same and does not depend on location (Fig. 1).

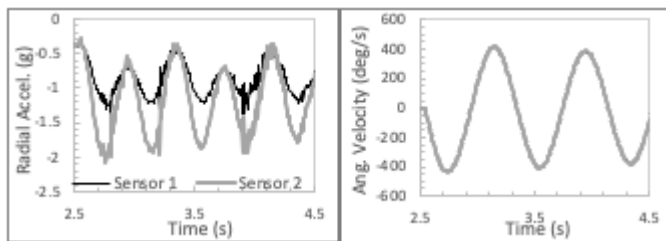


Figure 1: Linear acceleration (left) along the long axis of link and angular velocity (right) from each sensor while swinging.

Working with this data, we were able to prove several things based on calculations using the kinematics equations presented above. Most importantly, given the data from one IMU, and the position of a second location on the rigid body relative to the IMU, we can compute the linear accelerations of the second point. This was verified by comparing the calculated results with the data from the second sensor (Fig. 2-3). Thus, only one IMU sensor per rigid body is required if precise locations can be measured relative to the sensor.

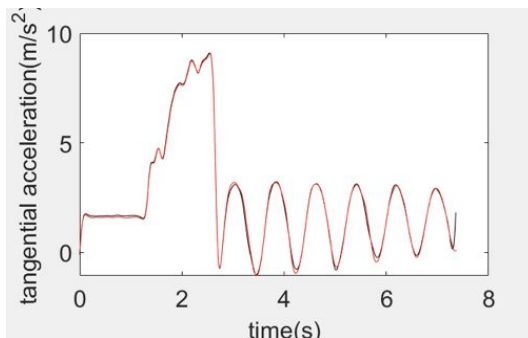


Figure 2: Normal acceleration of sensor 2 measured (red) and calculated using sensor 1 data (black).

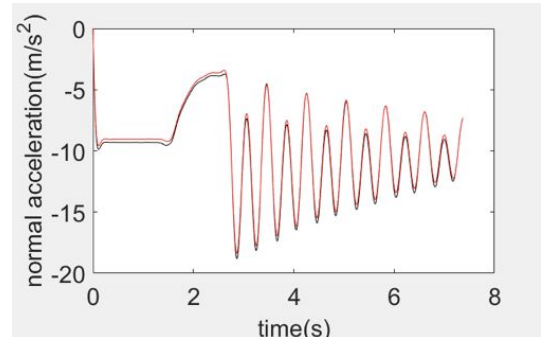


Figure 3: Tangential acceleration of sensor 2 measured (red) and calculated using sensor 1 data (black).

Other notable validations include calculating angular velocity and acceleration from linear acceleration data of both sensors. If equipment limitations exist, a researcher could use two 3D accelerometers to compute rotational kinematics of a rigid body. It is also possible to calculate the position vector between two IMU sensors based on the equations above.

The remaining goal of this work is to move from the two-dimensional framework to 3-dimensional space. Also, validation is required in a biomechanics setting. We plan to use the shank with two IMUs as the rigid body, in conjunction with an optoelectronic motion capture system as validation of the IMU data.

CONCLUSIONS

IMUs are extremely versatile tools for data collection. By demonstrating how the data collected from two IMUs are similar to the anticipated data based upon the primary sensor, researchers will have a better understanding of how these sensors can be used in more complicated experiments. This is meant to introduce and reinforce the fundamentals of rigid body kinematics for use with IMUs.

REFERENCES

- [1] Favre, J. et al. (2009). *J Biomech*, **42**:2330-2335.
- [2] Cain, SM et al. (2016). *Gait Posture*, **43**:65-69.
- [3] Seel, T & Schauer, T (2013). *P 4th Eur Conf Technically Assisted Rehab*

Evaluation of Foot Placement Control on a Lower Limb Exoskeleton

Huawei Wang and Antonie van den Bogert

Cleveland State University, Cleveland, OH, USA

email: h.wang59@vikes.csuohio.edu, web: www.hmc.csuohio.edu

INTRODUCTION

Lower limb exoskeletons have been developed that intend to help people with locomotor disabilities to regain the ability to stand up, walk, and even run. Even though the hardware design of current devices has become compact and elegant, crutches are always needed to keep balance. This limitation is a consequence of fixed reference trajectories used to control joint motions, lacking the ability to response to walking pattern changes and external perturbations [1-2].

Humans use the so-called “step strategy” during walking to maintain balance. The strategy involves controlling the swing leg for stepping to appropriate locations. Studies have shown that healthy adults may choose their foot placement based on position and velocity of the pelvis or Center of Mass (CoM) [3]. Humanoid robots have achieved stable walking even with external perturbations by using this control algorithm [4]. However, this control strategy has not been used in lower limb exoskeletons.

We propose that step strategy controller can be applied on lower limb exoskeletons and help the user maintain balance during walking. To answer this, we implemented the step strategy control on an Indego exoskeleton (Parker-Hannifin Corp., Cleveland, OH) and conducted walking tests with healthy adults. Activation of six leg muscles was measured and analyzed with and without the step strategy control.

METHODS

Step strategy controls the swing leg stepping to appropriate landing locations. A linear inverted pendulum (LIP) model is used to determine the foot placement location required for stability. Pelvis position and velocity relative to the stance foot are inputs of the LIP model and were calculated from the knee and hip joint angles of stance leg. A swing path

was generated based on the estimated landing location and a constant swing duration (0.6 second) according to a polynomial function. Reference joint angles for the hip and knee joints of swing leg were calculated through inverse kinematics at each time frame. Proportional-derivative (PD) controllers were used at the hip (1600 Nm/rad and $120 \text{ Nm} \cdot \text{s/rad}$) and knee (1200 Nm/rad and $80 \text{ Nm} \cdot \text{s/rad}$) joints to track the calculated reference joint angles. Instrumented treadmill was used to detect ground reaction force and then to separate the stance and swing phase. Step strategy only controls the motion of the swing period, the stance leg of Indego was in fully passive (Fig. 1).

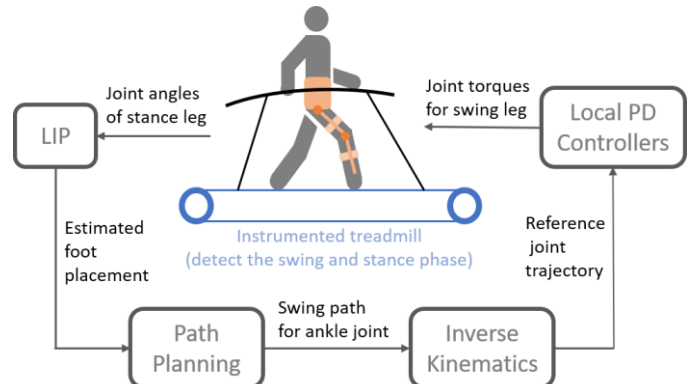


Figure 1: Structure of the step strategy control for Indego Exoskeleton.

Two healthy adults were included in the walking test. Six electromyographic (EMG) sensors were used to record the right leg’s muscle activation during the test. Measured muscles are: *Biceps Femoris; Gluteus Maximus; Semitendinosus; Lateral Gastrocnemius; Medium Gastrocnemius; Rectus Femoris*. The test spanned over two days. On the first day, participants were asked to perform natural walking without exoskeleton and walking with passive exoskeleton. Results of these walking tests were used to personalize the step strategy controller for each participant. On the second day, participants were

asked to walk with passive and step strategy-controlled exoskeleton. Each walking trial was 2.5 minutes long.

Muscle activation was processed and averaged over gait cycles in each walking trial [5]. Comparisons of the averaged muscle activation between passive and step strategy-controlled exoskeleton trials were included.

RESULTS AND DISCUSSION

Two participants were able to keep stable walking with the step strategy controller. Both mentioned that the step strategy-controlled exoskeleton was helping them to swing their legs forward which reduced around 50% of their total efforts. However, muscle activation of these two participants does not fully support their feeling.

In general, the first participant has significant higher muscle activation (yellow line indicates significant difference ($P < 0.05$) between two trials) in the step strategy controlled trial (blue line and area) than the passive trial (red line and area) during majority of the swing period (grey x axis) (Fig. 2). Bioceps Femoris, Gluteus Maximus, and Semitendinosus have significant smaller muscle activation at the early swing with the step strategy controller. Higher muscle activation in the step strategy-controlled trial was not expected which means that the participant was fighting with the exoskeleton.

The second participant has significant higher muscle activation in the step strategy-controlled trial at early and middle swing period (Fig. 3). At the late swing, he has less muscle activation of almost all six monitored muscles. This lower muscle activation indicates that the step strategy-controlled exoskeleton was helping him to slow down the swing leg before landing.

CONCLUSIONS

In this study, we implemented the step strategy controller on a lower limb exoskeleton and generated stable walking motion with healthy participants. Muscle activation results showed unclear effects of this control strategy. More studies are needed.

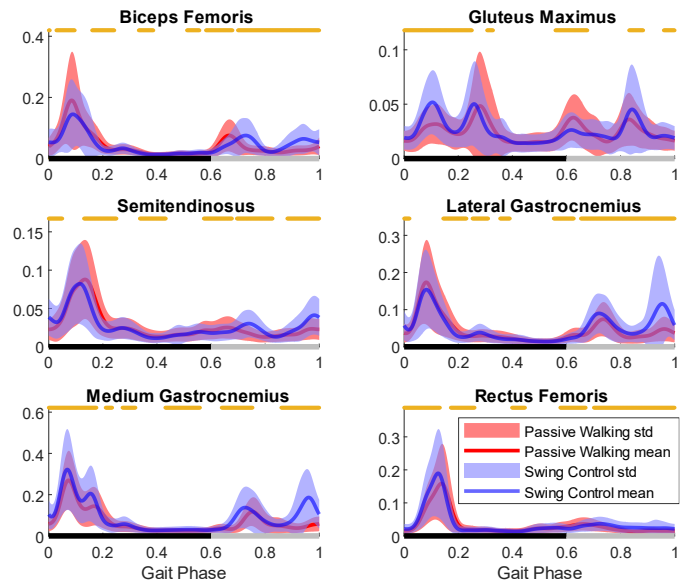


Figure 2: Comparison of muscle activation in constant speed walking (participant 1).

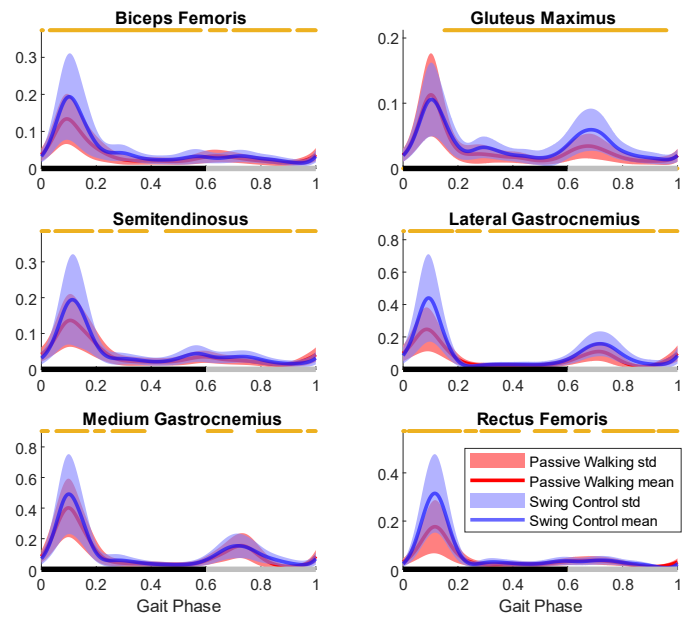


Figure 3: Comparison of muscle activation in constant speed walking (participant 2).

REFERENCES

1. Quintero HA, et al. *JMD*, **6(4)**, 041-003, 2012.
2. Esquenazi A, et al. *JPMR* **91(11)**, 911-921, 2012.
3. Koolen T, et al. *IJRR* **21(9)**, 1094-1113, 2012.
4. Pratt J, et al. *IJRR* **31(10)**, 1117-1133, 2012.
5. Konrad, P. The abc of emg, 1(2005), pp.30-5.

ACKNOWLEDGEMENTS

This work is support by NSF 1344954 and 1544702.

ISOLATED SEAT PAN TILT REDUCES BUTTOCK AND LOWER BACK PRESSURE ON ABLE-BODIED INDIVIDUALS AND WHEELCHAIR USERS WHILE SEATED

¹Justin Scott and ¹Tamara Reid Bush, PhD

¹Michigan State University, East Lansing, MI, USA

Email: scottju5@msu.edu, reidtama@msu.edu

INTRODUCTION

Wheelchair users (WCs) experience pressure ulcers (PUs) at a staggering rate, with a prevalence as high as 47% in care facilities [1]. As a result, PUs cost the United States healthcare system about \$1.3 billion annually [2]. PUs are caused by sustained external pressure on the body, so wheelchair design has tried to reduce pressure on areas that experience large pressures while seated. Half of PUs occur in the buttocks and lower back, so those areas are of particular concern [3]. Back recline and whole-body tilt (simultaneous back recline and seat pan tilt) are the most common movements used to relieve pressure while seated [4].

Despite the popularity of back recline and whole-body tilt, there is little research demonstrating their efficacy. Notably, most studies do not have pressure data in the neutral (no back recline or seat pan tilt), reclined, and tilted positions; and most studies have no data from WCs. Commercial wheelchairs include back recline and whole-body tilt, but PUs are still prevalent in WCs. Thus, we propose an isolated rearward seat pan tilt to offload the buttocks and lower back while seated. The goal of this work was to evaluate the efficacy of back recline and whole-body tilt in reducing the maximum pressure on the buttocks and lower back while seated and to compare them to a position with an isolated seat pan tilt.

METHODS

Twenty able-bodied individuals (ABs) (ten males, ten females) and ten male WCs (IRB #15-889)

participated in this study. An articulating chair was constructed with independent rotations of the back and seat pan (Figure 1). Data were collected on participants in nine positions with varying back recline angles and seat pan tilt angles. Three angles of back recline (0° , 10° , 20°) and three angles of seat pan tilt (0° , 15° , 30°) were tested, with 0° back recline and seat pan tilt shown in Figure 1.

Pressure mats were placed on the back support and seat pan of the chair to collect pressure data in each position. Each pressure mat was an array of 42 rows with 48 sensors. Pressure data were split into three regions: the thighs (anterior half of the seat pan mat), buttocks (posterior half of the seat pan mat), and lower back (inferior third of the back mat). The maximum pressures in each region were determined by calculating the maximum average measurement over any three by three set of sensors in the region.

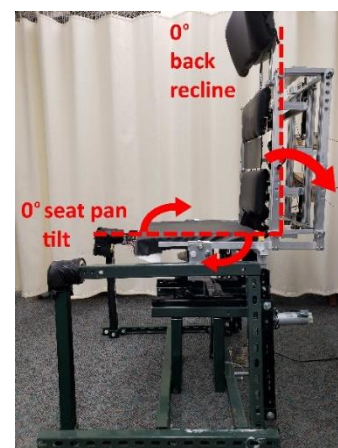


Figure 1: Side view of the articulating chair, with the top arrow showing the back recline and bottom arrows showing seat pan tilt. The vertical dashed line shows 0° recline, and the horizontal dashed line shows 0° seat pan tilt

RESULTS AND DISCUSSION

Increasing back recline increased the maximum pressures in the lower back and buttocks of ABs and WCs, while decreasing maximum pressure in the thighs (Figure 2). Increasing seat pan tilt had the opposite effect, seen in Figure 3.

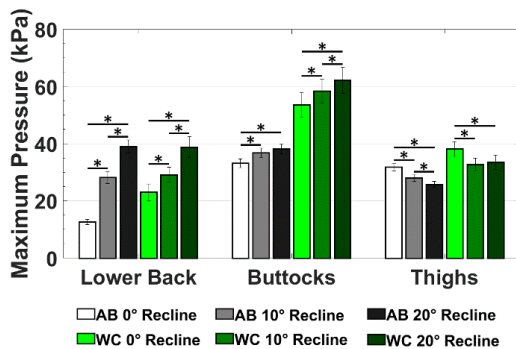


Figure 2: Maximum pressure values for each region in each recline angle, with ABs in greyscale and WCs in green. Significant differences are denoted by asterisks (*)

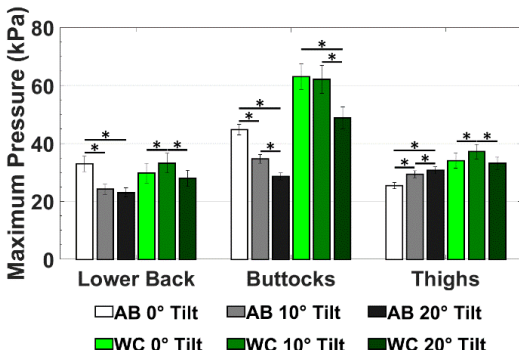


Figure 3: Maximum pressure values for each region in each pan tilt angle, with ABs in greyscale and WCs in green. Significant differences are denoted by asterisks (*)

The collected data are critical because they include data from ABs and WCs in several positions. The maximum pressures on WCs were generally larger than those of ABs. These pressures indicate an overall increase in PU risk for WCs that may not be captured by testing only ABs. Meanwhile, there were common trends in pressure shifts between the two groups. The reported data support the use of an isolated seat pan tilt to reduce the maximum pressures on the buttocks and lower back of ABs and WCs. However, increasing back recline, which is

most often used to relieve pressure on the body, does not offload the pressure on the buttocks or lower back. Whole-body tilt did not have any consistent pressure changes relative to a neutral position with no back recline or seat pan tilt, indicating that it does not decrease the risk of PUs in seated individuals.

Both back recline and seat pan tilt increased the maximum pressure in one region while decreasing it in another. There is previous work showing that soft tissue is more resilient to higher pressures if those pressure are intermittently relieved [5]. Because of this, there is a need for a position change regimen that moves between several positions, to reduce the risk of a PU in any single region.

CONCLUSION

When considering the design of equipment such as wheelchairs, it is important to include the intended user in data collection. This work was vital because it included data from WCs while investigating the effects of chair movements on seated pressures. In doing so, this work showed that there are larger pressures on WCs as compared to ABs. The trends recorded support the use of an isolated seat pan tilt to relieve the pressure on the buttocks and lower back while seated; and the use of a movement regimen to reduce the risk of PU formation in any region.

REFERENCES

1. Cowan, L.J., et al., *Wound Care*, 32:122-130, 2019.
2. S.D. Horn, et al., *J. Am. Ger. Soc.*, 50: 1816-1825, 2002.
3. Peart, J. *Br. J. Nursing*, 25: 840-843, 2016.
4. Ding, D., et al., *J. Rehab. Res. Dev.*, 45, 2008.
5. Linder-Ganz, E., et al. *J Biomech.*, 39: 2725-2732, 2006.

ACKNOWLEDGEMENTS

Research was funded by NSF Grant CBET-1603646.

ESTIMATION OF KNEE LIGAMENT SLACK LENGTH UTILIZING NOVEL DISTRACTION LOADING FOR MULTIPLE SPECIMENS

¹ William Zaylor, ²Jason P. Halloran

¹Cleveland State University, Cleveland, OH, USA. ²Applied Sciences Laboratory, Institute for Shock Physics, Washington State University, Spokane WA, USA.
email: w.zaylor@vikes.csuohio.edu

INTRODUCTION

Ligaments influence the internal forces acting across the knee. Physical testing and computational models have shown that the knee's mechanics are sensitive to ligament slack length [1], [2]. Computational knee models that utilize specimen-specific ligament properties have shown better performance than models that utilize literature-based properties [3]. Inverse modeling is normally used to estimate specimen-specific ligament properties [4]. These methods use optimization to minimize the residual between model predicted and experimentally measured joint mechanics. This approach assumes that for a given joint position the external joint forces balance with the internal ligament and contact forces. The experimental loading can be changed to avoid articular contact, which would limit the internal joint forces to soft-tissue restraints [5]. The purpose of this work was to use novel experimental loading in an inverse modeling scheme to estimate ligament slack lengths for two specimens.

METHODS

Experimental joint distraction tests were conducted with two knee specimens. The specimens were prepared following the Open Knee(s) protocol [6]. In summary, registration markers were fixed to the specimen approximately 15 cm proximal and distal to the knee joint line. These markers were digitized and present for MR imaging to facilitate model development. After imaging, the specimen was dissected by an orthopedic surgeon. The patella was removed, along with the skin and muscle around the knee joint. To avoid contact during testing, the surgeon removed the inferior and posterior articulating surface of the femur (Fig. 1).

Three laxity-style distraction test cases were performed with a six degree of freedom (DOF) robot (SimVitro, Cleveland Clinic) at 0°, 30°, 60°,



Figure 1: The specimen after the femur's articulating surface was removed by an orthopedic surgeon.

and 90° flexion. These test cases were **load case 1**: anterior and posterior loads that increased up to ± 100 N while a constant 75 N distraction load was applied **load case 2**: fixed varus or valgus at 5°, each with a distraction force that increased from 25 to 100 N, and **load case 3**: distraction from 25 N to 100 N where only flexion was fixed.

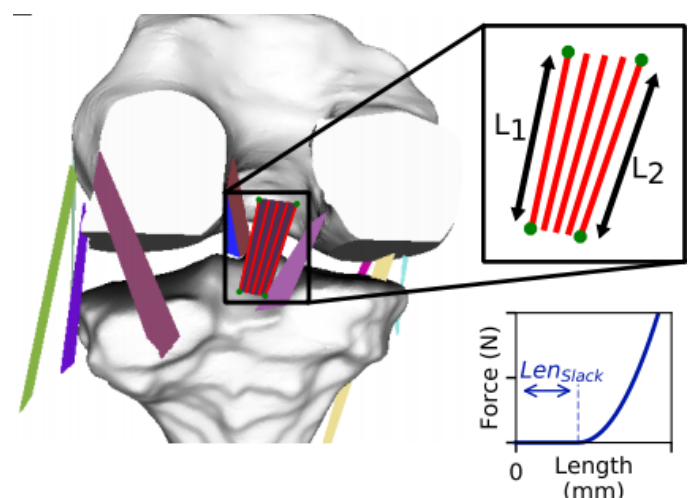


Figure 2: The specimen-specific knee model for one specimen. (Inset) An example of how slack length values were specified for a ligament, and the nonlinear force-length relationship that was used for each fiber.

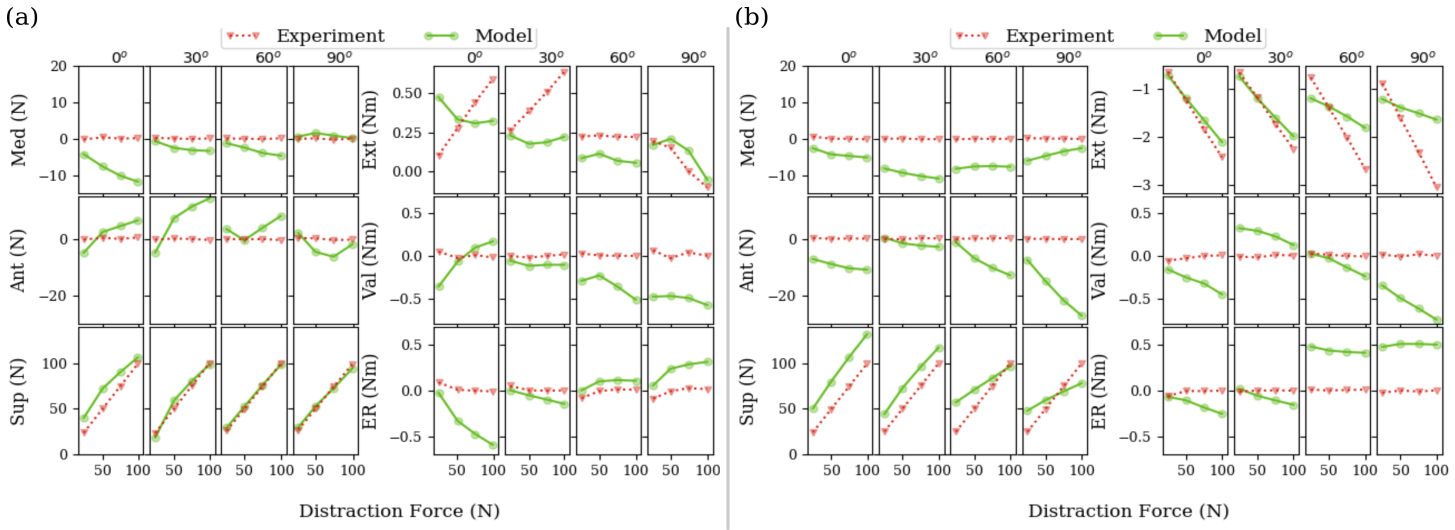


Figure 3: Experimentally measured and model predicted tibial reaction forces and moments during the distraction test (load case 3) for (a) specimen 1 and (b) specimen 2. This load case was not included in the optimization.

A specimen-specific forward kinematic knee model was generated for each specimen, where each ligament was modeled as a bundle of 25 nonlinear springs (Fig. 2). Two values were used to define slack length for each ligament, where these values defined the slack length of the fibers at the margins of the ligament fiber bundle (Fig. 2). Slack lengths of the remaining 23 fibers in the ligament was defined with linear interpolation.

The specimen-specific forward kinematic models were used in an inverse modeling scheme to estimate ligament slack lengths. A constrained sequential quadratic programming optimization algorithm was used to minimize the squared residual between model predicted and experimentally measured tibial reaction loads for load cases 1 and 2. Load case 3 was not included in the inverse modeling scheme. The objective function included all six kinetic DOF. The force residuals were weighted with a value of 1 and moment residuals were weighted with a value of 20. Inequality constraints were used in the optimization where each control variable was associated with an inequality constraint. The constraint would be violated if the corresponding ligament fiber carried less than 0.1 N at any point in the simulated load cases (load case 1 and 2). This ensured that each control variable in the optimization can affect the objective value.

RESULTS AND DISCUSSION

Both specimens generally recreated the experimental loads. For the load cases included in the optimization, the RMS force and moment errors were less than 18 N and 0.85 Nm, respectively (Fig. 3). For the distraction test (load case 3), which was not included in the optimization, the RMS force and moment errors were less than 23 N and 0.51 Nm, respectively (Fig. 3).

This study used novel experimental loading in an inverse modeling scheme to estimate specimen-specific ligament slack lengths for two specimens. The RMS errors in tibial reaction loads for the test excluded from the optimization indicate that the inverse modeling scheme was able to estimate specimen-specific ligament slack lengths. Future work should evaluate whether the estimated slack lengths can be applied to a corresponding forward dynamics model to estimate joint kinematic errors under traditional laxity loading. The kinematic errors would provide a direct comparison to other inverse modeling studies and highlight the utility of the methods described in this current study.

REFERENCES

- [1] C. W. Imhauser, *et al.*, *J. Biomech.*, Nov. 2017.
- [2] M. Baldwin, *et al.*, *Comput. Methods Biomed. Engin.*, Dec. 2009.
- [3] J. A. Ewing *et al.*, *J. Orthop. Res.*, Sep. 2015.
- [4] L. Blanckvoort and R. Huiskes, *J. Biomech.*, Jul. 1996.
- [5] W. Taylor, *et al.*, *J. Biomech.*, Jul. 2019.
- [6] “Open Knee(s): virtual biomechanical representations of the knee joint.” <https://simtk.org/home/openknee>.

DESIGN OF TPMS FOR TISSUE ENGINEERED SCAFFOLDS USING NTOP PLATFORM

¹Andrew Fretwell (Presenter), Matthew Shomper, Trenton Classen, Joel Pensworth, and Timothy Norman

¹Cedarville University, Cedarville, OH, USA

Email: tnorman@cedarville.edu

INTRODUCTION

In the medical industry, there is a growing need for affordable implants that are customized to each patient. Just as each bone defect is unique, so is each patient in need of an implant. Additive manufacturing (AM) allows for the creation of more complex geometries than traditional manufacturing methods and can be used to make customized titanium implants. Triply-periodic minimal surfaces (TPMS) can be created using AM. TPMS structures have continuous smooth surfaces in which the mean curvature of the surface is zero [1]. TPMS have a high ratio of surface area to volume, allowing more room for osteoblasts to adhere to the structure [2]. TPMS are also preferred for biological applications because they have a long fatigue life, are less prone to stress risers and concentrations, and encourage homogeneous cell generation [3].

METHODS

In this study, we created cubic lattices composed of repeating TPMS unit cells to match the strain response rate of natural trabecular bone. TPMS unit cells come in a variety of types. The diamond and gyroid unit cell types are studied here.

Using nTop Platform (New York, NY), we generated TPMS lattices in the shape of 1cm³ cubes, utilizing both the diamond and gyroid unit cell types. We created nearly 70 lattices, varying the wall thicknesses and the sizes of the repeated TPMS unit cells. The cell size was varied from 1mm³ to 10mm³ in 1mm³ increments, and these 10 designs each had a respective group of models with varying wall thicknesses. When increasing the wall thicknesses for each design, a point was reached where increasing the thickness any more would not be beneficial, as the resulting geometry would resemble a solid cube. This is illustrated in Figure 1.

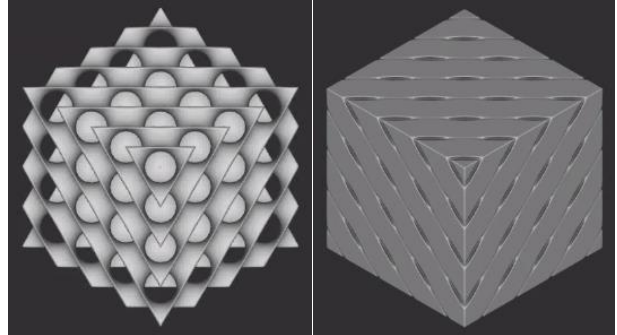


Figure 1. Diamond TPMS lattices with 5 mm unit cell side lengths. 0.25 mm wall thickness (left); 1.75 mm wall thickness (right)

Once we had created the lattices that fell within the range of 1mm-10mm side lengths and with varying thicknesses, we performed finite element analysis (FEA) on the lattices (Figure 2). In order to perform satisfactorily as implants, a target strain range of 1500-3000 $\mu\epsilon$ for the lattices was used [4]. For our analyses we subjected each scaffold to a 1000 N load, a conservative estimate for what is experienced in the human spine during moderate exercise [5].

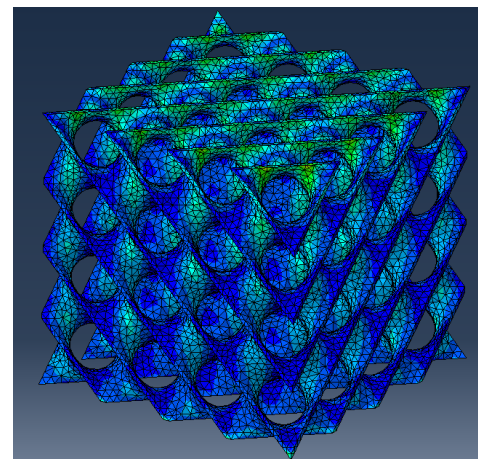


Figure 2. Max principle strain plot on diamond TPMS lattice (5 mm cell size, 0.25 mm wall thickness)

Using our results and the cross-sectional areas of the lattices, we also determined the stiffness of each structure, E_{global} . Due to the nature of TPMS, the cross-sectional area of each lattices is not constant. Because of this, an average cross-sectional area was used when calculating stiffness. 1-D Hooke's Law (Eq. 1) was used for the stiffness calculations.

$$\frac{Load}{A_{avg}} = E_{global}\varepsilon_{global} \quad (1)$$

After analyzing our models using FEA, we printed physical lattices in order to verify our results. The physical models were additively manufactured using Ti-6Al-4V and Selective Laser Melting techniques at Tangible Solutions (Fairborn, OH) (Figure 3). Compressive loading was applied to the lattices to determine their stiffnesses, and the average cross-sectional areas were used as with the FE models.

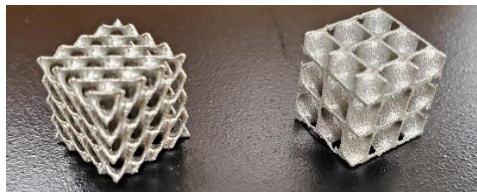


Figure 3. 10 mm diamond TPMS cubes. 5 mm cell size, 0.25 mm thickness (left); 8mm cell size, 0.5 mm thickness (right)

RESULTS AND DISCUSSION

Figure 4 shows an interpolated surface using the resulting strains from a select group of diamond TPMS lattices, containing 25 models that experienced max strains near our desired strain range. Horizontal planes mark the desired strain range for the lattices. For a given cell size or thickness, there is a complementary range of thicknesses or cell sizes that produces a strain value within the desired range.

The two physically tested lattices had similar performances when loaded compressively. Both the 5 mm cell – 0.25 mm thickness specimen and the 8 mm cell – 0.5 mm thickness specimen has stiffnesses of about 11.4 GPa. This value is lower than the values obtained through FEA, as these two models were predicted to have stiffnesses of about 19 GPa. This discrepancy is under investigation but may be

attributed to the general differences between ideal numerical calculations and physical models. While different, both of these stiffness values are very comparable to that of bone.

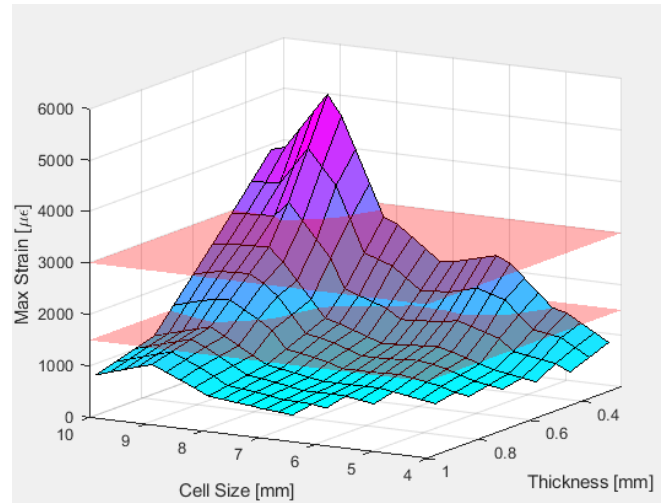


Figure 4. Max principle strain of diamond TPMS finite element lattices subjected to 1000 N load

CONCLUSION

In conclusion, we found that we were able to successfully mimic the strain response rate of trabecular bone with TPMS lattices designed in nTop Platform. These TPMS lattices had high porosity and surface area conducive to cell proliferation. In addition, stiffnesses were comparable to bone which should promote bone remodeling and implant sustainability.

REFERENCES

1. Yan, C. et al. *Journal of the Mechanical Behavior of Biomedical Materials* pp. 61-73 (2015)
2. Vijayavenkataraman, S. et al. *ACS Applied Biomaterials* pp. 259-269 (2018)
3. Liu, F. et al. *Materials and Design* pp. 849-860 (2018)
4. Khan, K., et al. *Physical Activity and Bone Health*. Human Kinetics, 2001.
5. Rohlmann, A., et al. *Activities of Everyday Life with High Spinal Loads*. (2014)

ACKNOWLEDGMENTS

The team would like to thank Tangible Solutions for printing our titanium lattices and nTopology for allowing us access to their nTop Platform software.

ADVANCING ERGONOMICS AND POSTURE THROUGH ENGINEERING PRINCIPLES AND AVATARS

Garrett Weidig¹, Archana Lamsal¹, and Tamara Reid Bush, PhD¹

¹Michigan State University, East Lansing, MI, USA

Email: weidigga@msu.edu, reidtama@msu.edu

Introduction

Whether it's playing video games, sitting in class, or working at the computer, posture is always a concern. With teens and young adults being exposed to technology more and more, bad habits with respect to posture are perpetuated [1]. This increase in technology use has been shown to cause poor posture, such as slouching with the shoulders or downward neck movement [2]. Poor posture can then lead to back pain and general joint pain- even for teenagers [3]. Ergonomic standards aim to correct poor posture, suggesting that ankle, knee, and hip angles should be at 90°. However, these standards are rarely known and are followed by even fewer. There is a need to identify and be able to measure good and poor postures. Also, so that these postures can be communicated to others, particularly teens and young adults, a visual representation of these body positions is necessary.

A bridge between engineering office seating and ergonomics is the use of an avatar. By linking motion data with a human body model, or avatar, differences in posture can be shown visually. Therefore, the goals of this study were twofold. The first was to define and identify poor posture, specifically rounding of the shoulders; and the second was to create an avatar that could serve as a communication medium for these raw data.

Methods

Movement data were recorded with an 11 camera motion capture system and reflective markers were placed on the body. Five participants were instructed to type and mouse as they would naturally. At the end of the five minute test, participants were positioned in an erect posture as defined by the ergonomic standards previously noted. The results of this study produced two outputs, the first being engineering definitions for poor posture, specifically related to shoulder curvature. Shoulder curvature was defined by the angle made by the left acromion (shoulder top), 7th

cervical vertebra (the top of the spine), and the right acromion (Figure 1). Poor posture was defined by the magnitude of the deviation from the erect posture. The second output from this study was the creation of an avatar from these data sets.

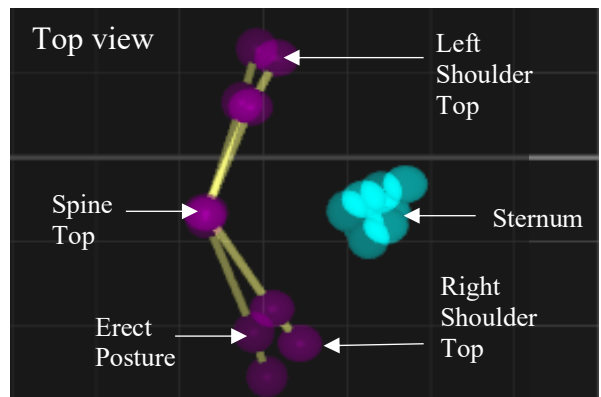


Figure 1: Top view of shoulder markers (purple) show deviation in posture between erect and slouched. Sternum markers (blue) are shown for reference. The erect posture is the most left set of purple markers. The slouched posture is the most right set of purple markers.

Results and Discussion

The following table provides the averages for the shoulder angle of the participants and the deviation from the erect posture, while mousing, and while typing.

Table 1. Average shoulder angle at erect and slouched postures while mousing and typing.

Posture	Shoulder Angle(°)	Angle Deviation(°)
Erect	127	-
Slouched Mousing	112	15
Slouched Typing	111	16

The data in Table 1 show that it is possible to define poor posture as a deviation from an erect posture. As of now, there is no spectrum that defines what levels of poor posture are associated with which angles of

shoulder curvature. However, these preliminary data show that there is a large difference between erect and slouched, from an engineering perspective.

For the second goal of this work, these data were incorporated into an avatar to demonstrate shoulder rounding. Figure 2 shows both shoulder rounding and how it visually compares to the erect posture.

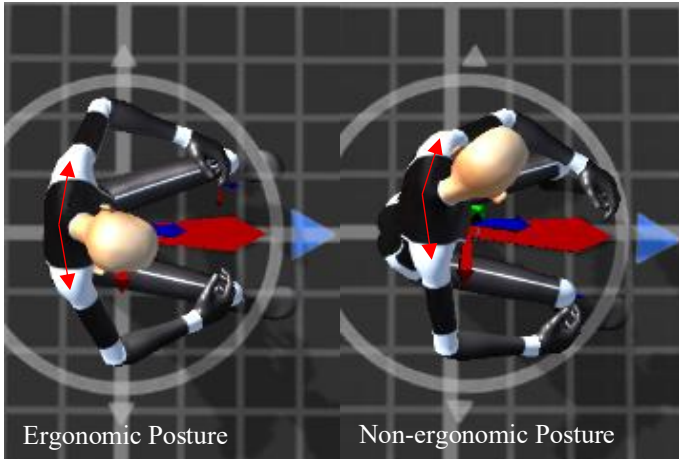


Figure 2: Top view of avatar shoulder curvature in an erect, ergonomic posture (left) and a slouched, non-ergonomic posture (right)

Just as there is a difference in the shoulder angle calculation, there is a clear difference in the shoulder rounding appearance in the avatar between the subject's erect and slouched postures. Figures 1 and 2 show that an avatar can accurately reflect the findings of basic engineering angles and can therefore accurately report posture and postural deviations.

Significance

The results of this study provided quantitative measures on slouched posture and provided a means to visually present these postural changes. This research has the potential to help in device design such as gaming chairs that provide more support when poor posture is engaged. This also opens up opportunities to create biofeedback devices that, based on duration and magnitude of the poor posture, will tell users how to correct their positioning. With more testing, postural changes between different demographics can be analyzed to further help office/gaming seating companies create optimized designs.

The use of the avatar reveals how people look in these poor postures and the use of the markers can verify the

posture. Future work will include more participants, including more activities for participants (such as using a cell phone or playing video games), and include standing.

References

1. Lim C. et al., (2013). *Bridging the Gap: Technology Trends and Use of Technology in Schools*
2. Laeser K. et al., (1998). *The Effect of Computer Workstation Design on Student Posture*
3. N. Quka et al., (2015). *Risk Factors of Poor Posture in Children and Its Prevalence*

BONE INGROWTH MODEL USING STRAIN CRITERIA

Brooke Hieronymus (Presenter), Joel Pensworth, and Timothy Norman

Cedarville University, School of Engineering and Computer Science, Cedarville, OH, USA

Email: tnorman@cedarville.edu

INTRODUCTION

Designing for biomimicry requires an understanding of the mechanobiological function of natural bone tissue. This consists of the physiological and cellular response to dynamic loading on the bone structure. The osteoclasts and osteoblasts are both active in remodeling: the breakdown of existing bone and the subsequent formation of new bone tissue [1]. The mechanostat theory by Frost describes when bone will remodel based on strain levels. According to this theory, bone is most stimulated to remodel between 1500-3000 $\mu\epsilon$ [2]. The higher the load onto the bone architecture the higher the strain, which is why exercise promotes the bone remodeling. Similarly, when loading is decreased, there will be a decrease in bone mass. When an area of bone experiences less than 200 $\mu\epsilon$ it typically results in bone resorption, the loss of bone mass [2]. The loading history affects bone quality and bone mineral density. Therefore, dynamic levels of strain are required to initiate bone remodeling. The strain frequency and strain gradients are also influential on bone morphology [1]. This study will focus on the strain magnitude and distribution. In order to promote bone cells to grow within a titanium scaffold, it is assumed that the initial strain value should be within the preferred range of 1500-3000 $\mu\epsilon$ recommended by the mechanostat theory strain criterion [2]. A bone ingrowth model as proposed uses a rule-of-mixtures equation to evaluate the composite stiffness and strain as bone grows into the titanium (Ti-6Al-4V) scaffold targeted for tissue engineering. The scaffold is produced by additive manufacturing and is designed to be implanted into a human lumbar spine.

METHODS

To have an accurate prediction of the loading conditions that the scaffold will experience when it is implanted into the human body, data from a vertebral body replacement study provides forces on a lumbar implant during typical daily movements

[4]. The analysis should consist of load values during inactivity as well as during intense physical activity to ensure that the bone experiences a minimum and a maximum strain within the desired ranges to maintain bone remodeling. After analysis of the research by Rohlmann [3], 1000 N was chosen to model a conservative value of force during exercise and is used in the calculation of resulting strain. Previous studies have used the rule-of-mixtures, modified it according to the material to model the mechanical properties of a composite, and found that their data corresponded well with the predicted behavior [4][5]. By the rule-of-mixtures, the composite stiffness (E_c) is the Young's modulus of bone (E_b) times volume fraction of bone (V_b) added to the Young's modulus of titanium (E_t) times the volume fraction of titanium (V_t):

$$E_c = E_b * V_b + E_t * V_t \quad (1)$$

The volume fraction of the composite that is bone increases as bone cells proliferate and remodel within the scaffold. The volume fraction that is titanium is determined by the porosity of the scaffold design. To determine the material stiffness of the titanium scaffold before bone ingrowth, Finite Element Analysis (FEA) can obtain the global deformation of the scaffold (δ). FEA analysis was completed on a diamond Triply Periodic Minimal Surface (TPMS) structure with a cubic unit cell size of 5mm and a wall thickness of 0.25mm (Fig. 1). The volume fraction of titanium in this scaffold is 0.1169. The global strain (ε_{global}) can be found from

$$\varepsilon_{global} = \frac{\delta}{height} \quad (2)$$

where the height of the scaffold equals 10mm. The global stiffness of the titanium structure can be

$$\text{calculated by } E_{global} = \frac{N}{\varepsilon_{global}} \quad (3)$$

where N is the load value in Newtons and the area is represented by the volume fraction of titanium.

E_{global} can be substituted in equation (1) for $E_t * V_t$ as the modulus of the scaffold geometry.

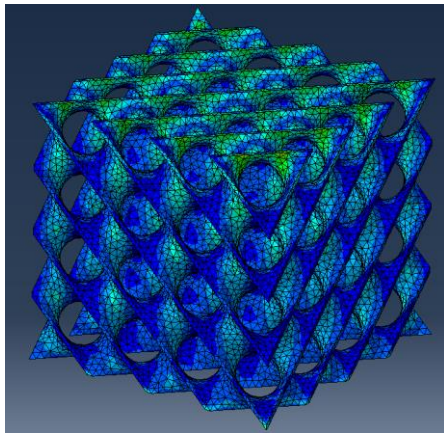


Figure 1. Max principle strain plot on diamond TPMS lattice (5 mm cell size, 0.25 mm wall thickness)

As bone grows into the scaffold, the strain in the composite structure will decrease, as there is more material to support the load. The resulting strain in the composite is found from the composite stiffness (E_c) and the cross-sectional area (the volume fraction of titanium and the bone ingrowth) solved by an equation of similar form of equation (3).

RESULTS AND DISCUSSION

The deformation under a case load of 1000N was 0.0023cm. A TK Solver (UTS, IL) code is used to calculate the global stiffness and the resulting composite stiffness with varying bone ingrowth percentages. This resulted in a stiffness (E_{global}) of 36.87GPa of the titanium scaffold. This modulus with zero bone ingrowth yielded $2320\mu\epsilon$, which is within the range that promotes bone remodeling. As an example, as the bone grows into the scaffold to fill it with 0.5 volume fraction bone and 0.1169 volume fraction titanium, the composite stiffness (E_c) is 44.37GPa and the strain becomes $365.3\mu\epsilon$. A plot (Fig. 2) was created to demonstrate the strain values in the scaffold as bone grows into it, as a function of the volume of titanium. To test other loading conditions, the linear relationship between the force value and the deformation allows for prediction of strain as well. The results show that this TPMS design (Fig. 1) is within the desired strain range for bone remodeling after it is initially implanted. Up to an infill of 50% volume it maintains the minimum

strain value to avoid decreasing bone mass. The 3D plot (Fig. 2) demonstrates that the strain decreases as bone grows into the scaffold, so it is important to analyze the strain after ingrowth. Future designs can be similarly analyzed using this process. Cell culturing experiments will also assist in the decision for which TPMS designs allow for the most advantageous bone ingrowth.

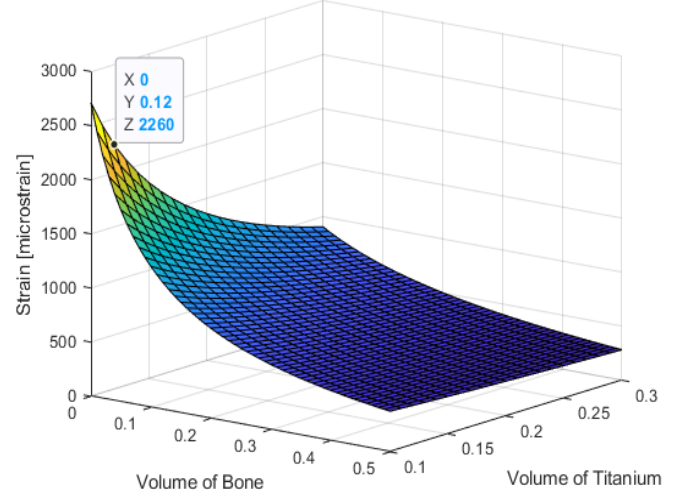


Figure 2. Bone ingrowth model of strain as influenced by the initial volume of titanium

CONCLUSION

The application of strain criteria developed by Frost [2] as the basis for designing scaffolds that will promote bone growth is an emerging concept. With the technology of additive manufacturing and the biocompatibility of Ti-6Al-4V, the future study on titanium scaffolds will be increasing. It is important to keep the end goal of the scaffold in mind, as it will remain in the person's body and will need to support the natural physiological processes.

REFERENCES

- [1] Nigg, B., et al. *Biomechanics of the Musculo-skeletal System*. Wiley, 2007.
- [2] Khan, K., et al. *Physical Activity and Bone Health*. Human Kinetics, 2001.
- [3] Rohlmann, A., et al. *Activities of Everyday Life with High Spinal Loads*. (2014)
- [4] Wagner, H., et al. *On the Relationship Between the Microstructure of Bone and its Mechanical Stiffness*. (1992).
- [5] Perreux, D., et al. *A Model for Prediction of Bone Stiffness Using a Mechanical Approach of Composite Materials*. ASME, 2007.

PATH PLANNING IS NECESSARY FOR ACCURATE CONTROL OF REACHING WITH A FUNCTIONAL ELECTRICAL STIMULATION DRIVEN ARM

¹Derek Wolf and ¹Eric Schearer

¹Cleveland State University, Cleveland, OH, USA

Email: d.n.wolf@vikes.csuohio.edu

INTRODUCTION

For individuals with tetraplegia, their highest priority for functional restoration is achieving hand and arm function. Functional electrical stimulation (FES) is a promising technique that reanimates paralyzed limbs by sending electrical signals to the paralyzed muscles and nerves. FES has been demonstrated to be effective in driving an arm through 2D reaching motions [1] as well as in holding static 3D positions [2]. To date, 3D reaching motions have yet to be achieved by controlling the complete arm with FES.

The roadblocks in achieving 3D reaching motions with FES include a limited number of activatable muscles, muscle weakness due to atrophy and fatigue, and muscle spasticity. These conditions are nearly universal among individuals in the spinal cord injury community. For these individuals, these conditions lead to a restricted feasible workspace even while driven with FES. The feasible workspace is defined as all wrist positions that the muscles can generate the forces necessary to move the arm to. The purpose of this study was to perform an initial analysis on the effect of this restricted feasible workspace on the ability to complete 3D reaching motions driven by FES.

METHODS

To analyze the effect of the feasible workspace, we completed a set of reaching experiments with the FES controlled arm of an individual with tetraplegia. With the data from these reaches, we determined a minimum required force necessary to achieve reaching motions. A simulated version of the workspace was then analyzed to determine the ability to find and achieve feasible reaching motions.

A. Reaching experiments

We completed the reaching experiments with a single human participant who has high tetraplegia and no voluntary movement of her right arm which is the arm we stimulated with FES. The procedures were approved by the internal review board at Cleveland State University (IRB #30213-SCH-HS).

The subject is implanted with a stimulator with which we vary the muscle activation by adjusting the pulse-width of the electric signal. We developed models of the forces produced by the stimulated muscles using the methods presented in [2]. We used these models to move the arm along straight line paths. A proportional-integral controller selected the forces necessary to move the wrist along the desired path. The muscle models were then inverted to select the muscle stimulation commands that most closely achieve the desired force. If the desired force was not possible to be achieved (due to muscle weakness), the goal of our controller was to produce the most possible force in the desired direction.

The accuracy of each reach was measured as the Euclidean distance from the final position of the subject's wrist to the desired final target. For each point of a trajectory, the maximum achievable force (as defined by our models) in the direction of the next desired wrist position was calculated, and the average force for the whole trajectory was recorded. The relationship between the average maximum force and the accuracy was analyzed graphically.

2. Workspace Analysis

We next analyzed the effect of the achievable muscle forces to find feasible reaching paths in the subject's

workspace. Using the relationship of the average maximum force to accuracy relationship, we selected a minimum force necessary to achieve accurate reaching motions. We then attempted to find paths in the subject's workspace (as defined by our models) through which the subject's muscles would be able to achieve this minimum force throughout the entire path. We analyzed the feasibility of achieving straight line paths to the target. The results of this portion of the study were analyzed graphically.

RESULTS AND DISCUSSION

To understand the effect the muscle forces have on the accuracy of a reach, we completed 90 straight line reaches and plotted the relationship of the accuracy and the maximum possible force along the desired path in Fig. 1. There is a clear negative correlation (correlation coefficient of -0.59) that demonstrates the importance of selecting paths that the muscles can achieve forces along.

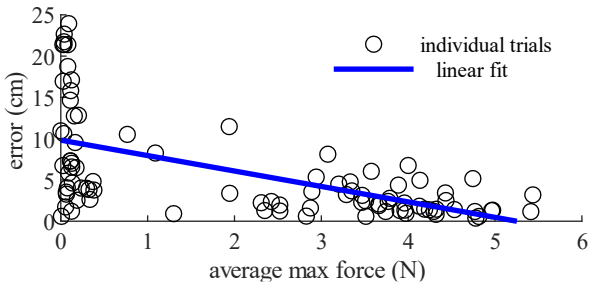


Figure 1: The relationship between the average maximum force that the muscles can produce for a reach and the error that is produced.

As seen in Fig. 1, reaches with an average maximum force greater than 2 N did not have an error larger than 10 cm. We therefore selected 2 N as the minimum force required to select a desired path. In Fig. 2, we show a planar view of the subject's 3D workspace. The green points are points from which the subject's muscles can produce 2 N of force in a straight line towards the target position (blue circle). It is only through a series of contiguous green positions that a straight-line reaching path is achievable.

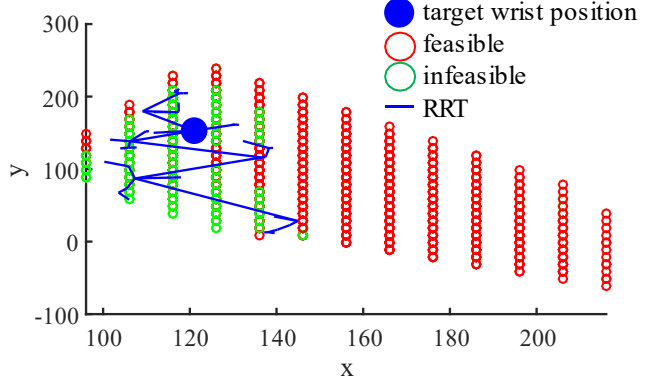


Figure 2: The wrist positions (green) at which 2 N force can be produced in the direction of the target (blue). Straight line paths would have to cross only green positions. The RRT path expands the points from which the target position can be achieved.

Clearly, using straight line paths are limiting to the possible reaches that can be achieved. Instead, we propose using a rapidly-exploring random tree (RRT) [3] to determine from which positions it is possible to get to the target with a minimum of 2 N force along the path. As seen in Fig. 2, after only 45 nodes, the RRT expands outside the green points to points which are not available with straight line paths.

CONCLUSION

Though only shown for a single wrist position in this study, these results demonstrate the need for a smarter path planning algorithm to achieve reaching motions with FES. We propose using an RRT to better define the feasible workspace and the reaches that are possible.

REFERENCES

1. Razavian, R. S., et al., *IEEE Transactions on Neural Systems and Rehabilitation Engineering*, pp. 2033-2043, 2018.
2. Wolf, D., et al., *IEEE Transactions on Neural Systems and Rehabilitation Engineering*, pp. 2044-2052, 2018.
3. LaValle, S., *IEEE Robotics and Automation Society Magazine*, pp. 79-89, 2011.

EFFECT OF AN ANKLE-FOOT ORTHOSIS ON REACTIVE STEPPING IN YOUNG ADULTS

¹ Kyra E. Twohy, Kurt Jackson and ¹ Kimberly E. Bigelow

¹ University of Dayton, Dayton, OH, USA

Email: twohyk1@udayton.edu

INTRODUCTION

Ankle-foot orthoses (AFO) are commonly prescribed to individuals with conditions such as stroke and multiple sclerosis to assist with foot drop and other gait deficits [1]. While AFOs have obvious benefits, there is believed to be some tradeoffs. In particular, the rigidity and support provided by AFOs may hinder ankle movements which could be helpful for tasks such as sit-to-stand or recovery upon a slip or trip. While there are numerous studies examining reactive stepping after a perturbation to better understand fall mechanisms and successful fall recovery strategies [2,3], to date, these studies have not included individuals wearing AFOs.

The goal of this pilot study was to examine, first in healthy young adults, differences in step recovery metrics when an AFO was worn compared to a no-AFO condition, using a lean-and-release paradigm. We hypothesized that individuals would prefer to step with the leg not wearing the AFO, and that the presence of an AFO on either the stepping or stance leg would increase the overall time it took to step.

METHODS

Eleven healthy, young adults aged 19 to 29 participated in this study. Study participants were excluded if they had prior use of an AFO, prior participation in lean-and-release studies, any current lower extremity injuries, and a history of neurological, musculoskeletal, or cardiopulmonary conditions that could influence stepping ability. All individuals gave written informed consent and all study procedures were approved by the University of Dayton Institutional Review Board.

Participants were fitted with an off-the-shelf polycarbonate leaf spring AFO and provided shoes to wear for all trials. Each participant had 25 retro-reflective markers placed on anatomical locations of

the back, hips, thighs, shank, and feet, as well as 4 marker plates each with 4 markers placed on the shank and the thigh. All participants were given standard earplugs, to eliminate sound cues of the release.

The lean-and-release system followed previous research and was set to induce a 15° forward lean, which was confirmed with an angle gauge [2,3]. To determine the moment of release during analysis, an additional 2 retro-reflective markers were attached to the harness, one that remained with the person after release and one that remained with the rope. Participants placed each foot on side-by-side Bertec in-ground force plates [Models 4060 and 4080]. For each trial, a researcher would pull the release mechanism at a random time, the participant would then do whatever was necessary to recover their balance.

A total of 30 reactive stepping trials were completed using the lean-and-release set up. The first 10 trials were used for familiarization and no AFO was present. Following the familiarization trials, a total of 20 trials with an AFO were completed, 10 on the right and the left leg, which were randomized in groups of two. All trials were recorded with a VICON motion capture system at 150 Hz.

Visual 3D was used to calculate step length and timing variables, identified by previous lean-and-release-research [2,3]. Timing variables were split into two, reaction time (the time between the release and when the stepping foot is completely unloaded) and step time (the time between stepping foot being unloaded and foot contact, defined by heel strike). Other variables studied included step length and stepping foot preference, defined by the number of recoveries initiated by the right foot with an AFO on the right leg, with an AFO on the left leg, and without an AFO.

Differences between reactive stepping with and without an AFO present was determined by running a one-way ANOVA with a Tukey post-hoc (significance of $p < 0.05$) in SPSS to compare the no AFO condition to the AFO placed on the stepping leg and to the AFO placed on the stance leg. Stepping foot preference was analyzed separately with a General Liner Model.

RESULTS AND DISCUSSION

The stepping foot preference did change when an AFO was present. Participants, on average, initially preferred to step with their right foot (7 of 10 trials with no AFO). However when an AFO was worn, stepping limb preference shifted significantly to keep the AFO on the stance limb (5.7 of 10 trials with an AFO on the right leg compared to 8.1 of 10 with an AFO on the left leg). This indicates that with an AFO present, stepping foot preference does change to favor keeping the constricted AFO leg in stance. Changes in preference may be due to increased weight or restriction of an AFO limiting the ability to move quickly, as a reactive step requires.

The impact of an AFO on the factors of a reactive step are displayed in Table 1, below.

Reaction time was significantly increased in trials without an AFO present as compared to the AFO placed on both the stance and the stepping leg. This was the opposite of the predicted outcome but could be due to the trials without the AFO being used for familiarization with the system. The increased

Table 1: Summary of Stepping Variables

	AFO Condition		
	No AFO	AFO on Stance Leg	AFO on Stepping Leg
Reaction Time (sec)	0.330 ± 0.062 *†	0.311 ± 0.055 *	0.296 ± 0.044 †
Stepping Time (sec)	0.192 ± 0.031	0.192 ± 0.051	0.189 ± 0.028
Step Length (m)	0.633 ± 0.087 ‡†	0.562 ± 0.135 ‡	0.542 ± 0.128 †

Significance: * $p < 0.05$, ‡ $p < 0.001$, † $p < 0.001$

standard deviation for the no AFO condition is evidence of more variable reaction time, perhaps as the participant adjusted to the novel perturbation.

No significant differences were seen in the step time across AFO conditions. This suggests that the swing phase of recovery is similar across conditions, with only reaction time impacting the total time from harness release to foot contact.

Step length was significantly different in the stance and stepping leg AFO conditions, as compared to the no AFO condition. Steps were longer when no AFO was present. The resulting shorter steps with an AFO could be due to a flat foot recovery strategy. As the knee extends to complete the step the toes are brought further up with the ankle constrained by the AFO. A shorter step is then needed to minimize plantarflexion to be able to land on a flat foot.

CONCLUSIONS

We found that reactive stepping in young adults is significantly impacted by the presence of an AFO. The AFO influenced both the preferred stepping foot and the factors of the step itself. This suggests that AFOs may change an individual's response to perturbations and should be examined more closely for their role in successful fall recovery.

REFERENCES

1. Pohl, M, et al. *Clinical rehabilitation*. 324-330, 2006.
2. Do, M, et al. *Journal of Biomechanics*. 933-939, 1982.
3. Hsiao-Wecksler, E. *Journal of Electromyography and Kinesiology*. 179-187, 2008.

ACKNOWLEDGEMENTS

The authors acknowledge Molly Chamberlain, Alex Nagy, Matthew Sheridan, Carter Langdon, Katie Valentine, Ryan Christopher, Hunter Andrews, and Aaron Scott for their help with data collection.

Model-free Trajectory Optimization of Human Training by Extremum Seeking

Humberto De las Casas^a, Nicholas Chambers^b, Hanz Richter^a, Kenneth Sparks^b

^a*Mechanical Engineering Department, Cleveland State University, Cleveland, OH 44115 USA.*

^b*Health and Human Performance Department, Cleveland State University, Cleveland, OH 44115 USA.*

1. Introduction

Research in human-machine interaction (HMI) has received a lot of attention in recent years because of the several applications with potential opportunities of development. For instance, human training has shown enhancement through the use of robotic training machines capable of providing variable resistance based on the user requirements [1] [2].

Human performance and engineering go hand-in-hand as the body is engineered to move efficiently and effectively. Human performance is concerned with measuring and perfecting the efficiency of the human movement. Typical measurements often collected include electromyography (EMG), heart rate (HR), oxygen consumption (VO_2), and energy requirements. In this work EMG was used in order to quantify the amount of work being performed.

The aim of this study was the automatic optimization of human training through the regulation of the geometric path to be tracked. The automated regulation seeks to be fulfilled without knowledge or model of the human dynamics but only using muscle effort distribution as a feedback. This is an application of a new mechatronic discipline called smart HMI [3]. This discipline considers the human dynamics in the closed-loop system. That makes possible to integrate human science together with mechanical, electrical, and information technology. This work focused on the use of ESC for trajectory optimization. ESC is a model-free controller for real-time optimization [4]. This controller was selected in order to deal with the unknown human dynamics and its volubility due to fatigue, body temperature, and level of hydration.

2. Dynamics

The dynamic systems involved include the AEM (robot dynamics) and the muscle dynamics. The robot used on this work as a AEM is a WAM robot. The WAM is 4 DOFs linkage robot from Barrett Advanced Robotics. The muscle dynamics are in function of several parameters. Some of these parameters are measured by sensors such as the user position and the interaction force between the human and machine by encoders and load cells respectively. However, most of them are unknown or difficult to measure, such as the musculoskeletal distribution, performance status, level of hydration, or joint orientations. Furthermore, some parameters like the muscle tem-

perature or fatigue make of the muscle dynamics time-varying. Consequently, the muscle dynamics are difficult to model.

3. Control System

Three controllers are involved in the project. The first two controllers, a PD and a gravity compensator controller, work isolated on the AEM and the third works on the HMI system.

In order to work on an ellipsoidal trajectory in 2D, the robot was restricted to work with 2 DOFs. Therefore, a PD controller was developed to fix the third and fourth joint. Furthermore, in order to improve the robot maneuverability, gravity compensation $\tau = g(q)$ was applied. The third and main controller is based on the use of the model-free deterministic perturbation Extremum Seeking Control (ESC) [5] [4]. This controller was selected to deal with the nonlinear time-varying muscle dynamics including the unknown and unmeasurable parameters.

ESC is a branch of adaptive control developed for optimization. The aim of this control is to enforces the output of a dynamical system to converge to unknown maximum or minimum operating points. The popularity of ESC lays on its model-free optimization algorithms and its ability to operate in real-time.

4. Methodology

The methodology of the study was experimental. One subject of the age of 23, height of 180 cm and weight of 91.8 kg performed several experiments on different days, under different physical conditions of resting and muscle fatigue. The major movements involved were flexion and extension, horizontal abduction and adduction, and anterior circumduction. Therefore, the four primary drivers for the glenohumeral joint were chosen in the following order: lateral deltoid (1), anterior deltoid (2), biceps brachii (3), and pectoralis major (4).

The HMI system can be seen on Figure 2. The closed-loop system is represented on Figure 1. The user and desired positions are labeled as a red dot and a black dot respectively in the map (see Figure 1-a). On the same figure, the blue line represents the ellipsoidal curve. The black dot goes over the ellipsoidal curve. And the red dashed lines represent the tolerance limits where the user is recommended to stay. The objective of the subject during the experiment was to follow the automatic regulated desired trajectory (see Figure 1-b). The raw muscle signals (Figure 1-c) are real-time processed to obtain the muscle

activation (Figure 1-d). Then, muscle activations are introduced to the performance function (Figure 1-e) to be maximized:

$$y(t) = \frac{t_s}{t_{rev}} \sum_{i=t-t_{rev}/t_s}^t \left(W^{[1 \times 4]} M^{[4 \times 1]} \right), \quad (1)$$

where t_s is the time sample set, t_{rev} is the frequency of revolution of the black dot, t is the time, W is the muscle weight vector. Due to the high sensibility of the muscle signal, a second order filter is applied at the output of the performance function (see Figure 1-f).

The main controller running the model-free optimization (see Figure 1-g) and making use of the processed performance function varies the geometric path to be tracked in order to find the solution which maximize the muscle performance. The trajectory is regulated by the new ellipse orientation (see Figure 1-h) and the cycle is repeated.

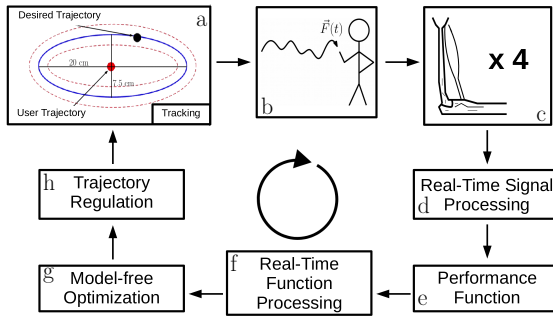


Figure 1: Closed-loop system scheme for the model-free optimization.



Figure 2: Experiment of human training with AEM.

5. Results and Discussion

One set of 2 experiments performed under the same parameter configuration but different physical condition is presented. The highest priority was given to the anterior deltoid and pectoralis major, the medium to the biceps brachii and the lowest priority to the lateral deltoid.

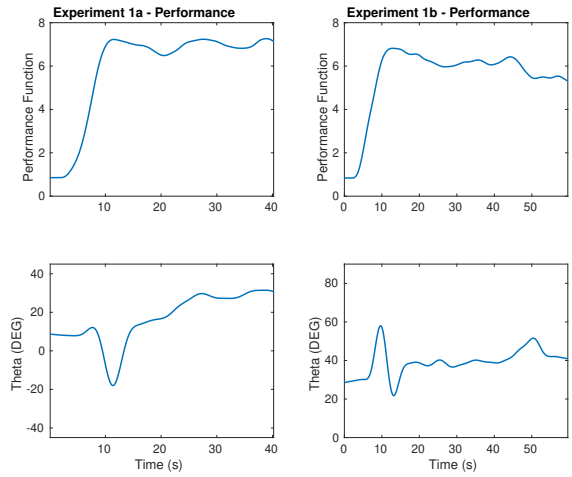


Figure 3: Set of experiments.

Upon completion of the experiments, a local maxima and a difference in muscle performance were exhibited. For instance, a higher performance function on Figure 3-a than on Figure 3-b was produced expected due to the increased effort of the muscles to perform activity during fatigue. However, despite of the difference in the muscle performance, each of the experiment converged to a solution in the same neighborhood. It is important to consider that the muscle dynamics are permanently changing. Therefore, ESC remains varying slightly even after reaching the optimal solution. Hereby, a convergence is assumed once the estimated parameter remains between $\pm 10^\circ$.

6. Future Work

Currently, the framework is being improved to include convergence criterion, performance measures, and a more controllable environment. Future research will be performed for single-variable optimization by trajectory parameter regulation, impedance regulation and multi-variable optimization by simultaneous trajectory and impedance regulation. Pilot studies will be performed, followed by research studies with a group of people.

References

- [1] H. De las Casas, H. Richter, A. van den Bogert, Design and hybrid impedance control of a powered rowing machine, in: ASME 2017 Dynamic Systems and Control Conference, 2017.
- [2] H. D. las Casas, K. Kleis, H. Richter, K. Sparks, A. van den Bogert, Eccentric training with a powered rowing machine, Medicine in Novel Technology and Devices 2 (2019) 100008.
- [3] F. Harashima, Human adaptive mechatronics, in: IEEE Workshop on Advanced Robotics and its Social Impacts, 2005., 2005, pp. 80–. doi:10.1109/ARSO.2005.1511624.
- [4] M. Krstic, Extremum Seeking Control, Springer London, London, 2013, pp. 1–5.
- [5] M. Krstic, H.-H. Wang, Stability of extremum seeking feedback for general nonlinear dynamic systems, Automatica 36 (4) (2000) 595 – 601.

LOWER BODY JOINT KINEMATICS FOLLOWING AN ANTERIOR CRUCIATE LIGAMENT (ACL) INJURY

¹ Vinayak Vijayan, ¹ Shanpu Fang, ¹ Megan Reissman, and ¹ Allison Kinney

¹ University of Dayton, Dayton, OH, USA

email: vijayanv1@udayton.edu

INTRODUCTION

ACL (Anterior Cruciate Ligament) injuries are common in active population [1]. A retrospective cohort study querying a national database for anterior cruciate ligament (ACL) injuries found that the rate of ACL injuries and ACL reconstruction surgeries were higher in a cohort of pediatric subjects (ages 5 to 19), when compared to a comparative cohort of adults (ages 20 to 45) [2]. The paper suggests an increased involvement in sports might be the reason for this higher rate of ACL injuries in the pediatric population. When compared to adults, the skeletally immature population also had significantly higher incidences of concomitant meniscal and cartilage injuries.

Despite the higher rate of ACL injuries in skeletally immature population, the research on kinematics after ACL reconstruction surgery has been skewed towards studying the joint kinematics of adults. The kinematic results from adults, who underwent ACL reconstruction surgery, might not strictly apply to pediatric patients, as the changes in bone dimensions of a growing pediatric patient could affect the kinematics of the subject's motion. The ACL reconstruction surgery itself, often, follows a slightly altered procedure for pediatric patients, to spare the epiphyseal plate [4]. Extensive damages to the epiphyseal plate could result in growth arrest, and other growth deformities like genu valgum and tibial recurvatum.

The higher rate of ACL injuries among pediatric individuals, the differences in the surgical procedure used in case of pediatric subjects, and the fact that skeletally immature patients are still growing, validates the need for separately and more comprehensively studying the kinetics and kinematics of pediatric subjects following an ACL reconstruction surgery. This work is a pilot study of a broader study, in collaboration with Dayton

Children's hospital, which hopes to fill the gap in knowledge about lower-body kinematics and kinetics of pediatric patients following an ACL reconstruction surgery.

METHODS

This pilot study, examines and compares the lower-body joint kinematics of a control subject to a subject who underwent a unilateral ACL reconstruction surgery. The participants were fitted with 41 retroreflective markers to keep track of the position and orientation of the different body segments. A Vicon motion capture system, along with 3 force plates were used to collect the kinematic data and ground reaction forces.

The protocol followed in this study involved a variety of 7 different tasks (walking, running, cutting, squatting, single-legged lateral hopping, sidestepping, and forward jumps) that would help in comprehensively defining the lower-body joint kinematics of the subjects, and identifying the differences in kinematics between the control subject and the ACL patient. Motion capture data and ground reaction forces were collected for at least 10 repetitions of each task for both subjects, and this data was processed in Visual3D and OpenSim. Some of the movements, examined in this study, involved higher degrees of hip and knee flexion. So, an appropriate model, created by Catelli et alia, capable of providing accurate kinematic data at extreme angles of hip and knee flexion was chosen for this study. The scaling tool in OpenSim was used to scale the generic model, to match the dimensions of individual subjects. The bigger segments in the model were scaled nonuniformly, by defining the scaling factors along 2 or 3 axes, and the smaller segments were scaled uniformly, by using only one scaling factor. Inverse kinematics was then used to match the position of the scaled model with the experimental data, and this simulated motion of the

scaled model was used to calculate the lower body joint kinematics.

The main factors considered for this study to compare the bilateral differences between the control subject and the ACL reconstructed subjects were: 1) the highest medial-lateral ground reaction force, 2) the highest anterior-posterior ground reaction force, 3) Hip (x, y, z), knee (x), and ankle (x) angles as a time series, and 4) Hip (x, y, z), knee (x), and ankle (x) angles at the point of maximum ground reaction force. A generalized linear model was used to evaluate whether the differences in kinematics and ground reaction forces seen between the affected and unaffected sides of the ACL subject was significantly different from the differences seen between the left and right side of the control subject.

RESULTS AND DISCUSSION

The differences in symmetry between left and right side, as a time series, was quantified by calculating the root mean square difference (RMSD) between the means of the sides during each task. No noticeable differences in symmetry were seen throughout the trials and tasks, in the case of the ACL subject. This could be because some of the important information about asymmetries that happen at points of interests might be averaged out when side-to-side differences are summarized by using RMSD, but RMSD might be a good tool going forward, to assess whether there are systematic and consistent bilateral differences across trials and tasks.

Different generalized linear models were built with hip angles, knee angles, ankle angles, and maximum

ground reaction forces as the response factors. Significant differences in kinematics between tasks was noticed in both the ACL subject and the control subject. This was expected, as the execution of the seven different tasks in the study protocol, required kinematically very different movements. The most interesting findings of the pilot study was that there were significant differences between the affected side and unaffected side in maximum ground reaction force produced, knee sagittal angles and ankle sagittal angles. These bilateral differences were not observed in the case of the control subject. Prior studies have also identified higher ground reaction forces as a risk factor for ACL injuries [3].

CONCLUSIONS

In this pilot study, significant differences were noticed in ground reaction forces, knee angles (sagittal), and ankle angle (sagittal) between the affected and unaffected sides of the ACL subject, and these differences were not noticed in the control subject. However, the reasons for these bilateral differences cannot be determined by this study, as only 2 subjects were used for this study.

REFERENCES

1. Webster, et al. *Journal of Orthopedics*, **36(10)**, 2696–2708, 2018.
2. Werner, et al. *Journal of Pediatric Orthopaedics*, **36.5**, 447-452, 2016.
3. Bourne, et al. *Sports medicine*. 1-7, 2019.
4. Shea, et al. *Knee Surgery, Sports Traumatology, Arthroscopy* **15.4**, 320-327, 2007

Table 1: Bilateral difference in the ACL subject and the control subject (The significant differences are marked with an asterisk *).

Response Variable	P-value	
	ACL	Control
Maximum force	<0.0001*	0.9397
Hip Sagittal	<0.0001*	0.3230
Hip Frontal	<0.0001*	<0.0001*
Hip Transverse	<0.0001*	<0.0001*
Knee Sagittal	<0.0001*	0.1011
Ankle Sagittal	<0.0001*	0.4184

INFLUENCE OF ADDED MASS ON THE KINEMATICS OF OVERGROUND WALKING AMONG YOUNG ADULTS

¹Shanpu Fang, ¹Vinayak Vijayan, ¹Megan E. Reissman, ¹Allison L. Kinney, ¹Timothy Reissman

¹University of Dayton, Dayton, OH, USA

Email: fangs4@udayton.edu

INTRODUCTION

An active gait exoskeleton device has the potential to improve the strength and mobility of its wearer by providing torque assistance at their lower limbs. For effective torque assistance, the exoskeleton must have an accurate estimate of the intended gait pattern of its wearer. However, intent recognition with accurate gait estimates has been described as difficult to achieve by the exoskeleton research community. The reasoning is hypothesized that since each device creates unique laden mass to the wearer, the wearer will then respond with unknown changes to their baseline kinematics. A few prior studies have shown that these changes are small but observable [1]. The challenge with applying such knowledge though is that this information is limited as the subjects were mostly young, healthy males ($n=5$) and were constrained to walking on a treadmill only, which alters a person's joint kinematics [2]. In this work, we aim to increase the scientific understanding of the influence of added mass by presenting the baseline kinematic changes of 12 young, healthy subjects (7 females and 5 males) who performed overground walking with 6 different conditions of laden mass on their lower body. The aim is to then provide a guide to exoskeleton design which minimizes the estimated changes to the wearer's baseline, or unladen, gait.

METHODS

This study was approved by the University of Dayton Institutional Review Board. Here we present the partial results for 12 participants (20-25 years of age) who gave written informed consent and completed the study. Each participant was asked to perform over-ground walking at a self-selected speed with

added masses of different levels: 2 or 4 pounds on each shank, 2 or 4 pounds on each thigh, and 4 or 8 pounds on the waist. In total there were 6 added mass loading conditions which were performed in random order, with 5 repeated walking trials for each condition. Full body gait kinematics were captured using an 8-camera Vicon motion capture setup with reflective markers ($n=43$) placed on the torso, pelvis, and lower limbs of each participant and post-processed using Nexus 2.9 software. OpenSim was then used for estimating the lower limb kinematics. For each participant, a scaled model was constructed using OpenSim's Gait 2392 model. The lower limb joint kinematics of interest were the hip, knee, and ankle in the sagittal plane. Analyses involved estimating the changes in degrees with respect to each participant's baseline.

RESULTS AND DISCUSSION

Added mass at the waist, thigh, and shank locations caused changes less than 6 degrees in lower limb joint angles in comparison to the baseline condition (Fig. 1). Most changes were of less than 2 degrees.

Both 4 and 8 pounds of added waist mass increased hip flexion throughout the gait cycle, with the largest changes of 4-6 degrees occurring with the 8 pound mass (Fig. 1, 400 and 800 conditions). Despite the larger influence on the hip kinematics, changes in both the knee and ankle angles were small for both levels of added waist mass. Thus, an exoskeleton design that limited its added mass to less than 4 pounds at the waist may reduce maximum kinematic changes considerably.

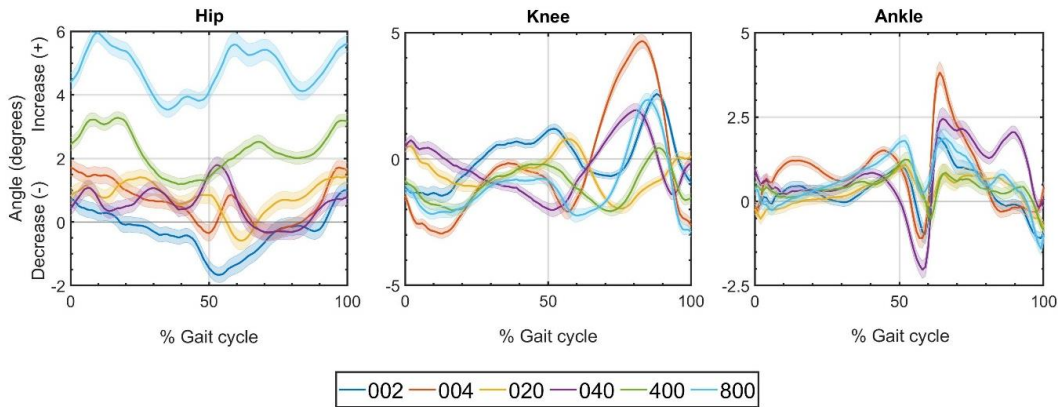


Figure 1. Change in angles relative to baseline condition across 12 subjects. Solid lines represent the mean differences with shaded bars representing the 95% confidence intervals. Each legend is in such sequence that, the first digit indicates added mass on the waist, the second for each thigh, and the third for each shank. Mass values are in pounds.

Adding mass to the thigh segment (Fig. 1, 020 and 040 conditions) had the smallest overall impact on the joint kinematics at all three joints. Both levels of added thigh mass caused joint angle changes of less than 2 degrees relative to the baseline condition. This suggests that exoskeleton designs that add up to 4 pounds of mass to the thigh segment will be well tolerated by young adults during walking.

Mass added to the shank segment, particularly the larger 4 pound mass, caused the largest changes in both knee and ankle kinematics in comparison to the baseline condition (Fig. 1, 002 and 004 conditions). Overall, the 4 pound mass led to the largest changes observed at both the knee and ankle joint. At the knee, the 4 pound mass increased knee flexion throughout stance and reduced knee flexion during the majority of swing reaching a peak of almost 5 degrees around 85% of the gait cycle. The larger shank mass caused relatively small changes in ankle angle during stance, but caused larger changes to the ankle kinematics during swing phase. Therefore, our younger adults had less ability to adapt to added shank mass that is typical of ankle exoskeletons.

CONCLUSION

As added thigh mass was best tolerated by the younger adults, an exoskeleton design that adds mass at the thigh will likely induce the smallest kinematic

changes during walking. Although added mass at the waist caused larger changes at the hip, the smaller 4 pound mass caused less kinematic alterations over all three joints. Therefore, exoskeletons may be better designed if they limit added mass to less than 4 pounds and distribute mass across the thigh and waist to reduce kinematic changes. Although our results indicate that younger adults have the capacity to adapt to added masses representative of an exoskeleton, our results are limited since other potential populations for exoskeleton use, i.e. older adults, likely do not have the same capacity to adapt. Future work will extend this study to observe how older adults (65-85 years of age) respond to added mass during walking.

REFERENCES

- [1] Browning, RC., Modica JR., Kram, R., Goswami, A. (2007). "The effects of adding mass to the legs on the energetics and biomechanics of walking," Med. Sci. Sports Exerc. 39(3), pp.515-525.
- [2] Sloot, H. L., Van der Krogt, M. M., Harlaar, J. (2014). "Self-paced versus fixed speed treadmill walking," Gait and Posture, 39(1), pp. 478-484.

ACKNOWLEDGEMENTS

We would like to thank Alice Luanpaisanon for her assistance with data collection.

Assessment of Frequency Power and Path Length in Postural Responses to Challenging Environments

Leah O’Shea, Jordan Pauley, Megan Reissman
University of Dayton, Dayton, OH, USA

INTRODUCTION

With increasing age, adults begin to exhibit more postural sway [1], which can be a marker for higher risk of falls. Among those with balance issues, challenging environments can increase this risk. Challenges can occur because of difficult terrain, dynamic perturbations, and visual stimuli [2]. As challenging environments are difficult to replicate experimentally, this study investigates balance response to different environments using Virtual Reality (VR).

This abstract focuses on the center of pressure (COP) and body segment trajectories, particularly frequency components and total path length. Total path length groups anterior-posterior and medio-lateral components of response into one measure and also captures some aspects of frequency content. Additionally, to better assess frequency content of postural sway we utilized a Fast Fourier Transform (FFT). The FFT is a widely used algorithm that directly filters noisy time domain signals in the frequency domain. This can then be used to calculate the power spectral density (PSD) which quantifies how power of a signal is distributed over frequency. Prior work suggests that particular bands of the power spectrum are associated with different sensory systems: 0-0.3 Hz for visual system, 0.3-1 Hz for vestibular system, and 1-3 Hz for proprioceptive system [5]. Age also appears to influence relative power between these bands, with healthy elderly individuals relying more on visual information during standing balance compared with healthy young individuals.

This study seeks to characterize differences in standing balance response between age groups and determine which environments elicit the greatest postural responses. We hypothesize that older adults will have a larger vestibular response when placed in the VR environments compared to the middle and younger adults. We also hypothesize that environments with dynamic visuals/platforms will produce a larger response.

METHODS

The study was approved by the University of Dayton IRB, and all subjects provided written consent prior to the study. Healthy participants were grouped into age brackets of Young (aged 18-29, n=15), Middle (aged 30-59, n=9), and Older (aged 60-85, n=7). Exclusion criteria included any neurological disorders, balance related impairments, pain with standing, or lower limb injury. Participants wore 27 motion capture markers to track the movement of their pelvis, torso, and head segments.

Participants stood on a Bertec 4080 series force plate (collecting at 1500Hz) for 1 minute during each trial. Eyes Open defined the baseline stance behavior prior to VR exposure. Each participant then viewed seven VR environments in a randomized order. Boat Day, Boat Night, and Train had dynamic (moving) visual stimuli and suggested a dynamic standing platform (translation or rotation). Busy Road had dynamic visual stimuli. Cliff, Office, and Tall Building had only static visual stimuli. After placing the headset on, participants had 1 minute to look around in the environment and acclimate themselves. Then, they were instructed to look forward with their hands at their side (test position) for 1 minute. Breaks were given between trials.

Visual3D (C-motion) was used to analyze the force plate data (COP) and the marker data to find the total path length. Two approaches were used to assess body sway: a single marker approach using markers at C7, T10, and S2 spinal locations and a segment (multi-marker) approach in which 3-4 markers on the pelvis or torso were used. Technical computing software, MATLAB, was used to calculate the PSD for the anterior-posterior and medio-lateral center of pressure trajectories. We then took the average power for the three frequency bands mentioned above: 0-0.3 Hz (visual), 0.3-1 Hz (vestibular), and 1-3 Hz (proprioceptive). Statistical software NCSS was used to run all comparisons, with significance set at p<0.05. A Repeated Measures ANOVA was used with a between factor of age group and a within factor of condition.

RESULTS AND DISCUSSION

Anterior-posterior center of pressure trajectories

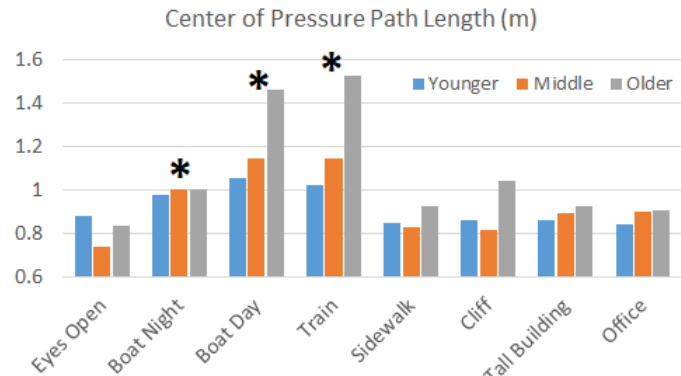
No significant differences were found between the age groups. Frequency power in the low band was significant for condition with Boat Day showing greater power than in the Eyes Open condition ($p<0.01$). Low frequency power in the postural response is thought to relate to increased weighting of visual inputs. Frequency power in the Middle and High band was significant for condition with all VR environments showing greater power than in the Eyes Open condition (all $p<0.01$). Middle band and High band frequency power is thought to relate to increased weighting of vestibular inputs and proprioceptive inputs respectively. This suggests that participants increased their reliance on vestibular and proprioceptive inputs which appears to be a reasonable strategy to maintain standing balance despite the (often contradicting) visual inputs provided by the VR system.

Medio-lateral center of pressure trajectories

No significant differences were found between the age groups. Frequency power in the low band was significant for condition with Train showing greater power than in the Eyes Open condition ($p<0.01$). Frequency power in the Middle and High band was significant for condition with all dynamic platform environments (Boat Day, Boat Night, Train) showing greater power than in the Eyes Open condition (all $p<0.05$). This suggests that only these environments that visually suggested medio-lateral movement/tilt elicited an increased reliance on vestibular and proprioceptive systems.

Total path length of COP and motion trajectories

For a standing balance task, we anticipated that there would be a larger response in COP and body trajectories for dynamic VR environments. **Figure 1** shows COP path length with * denoting a condition significantly different from Eyes Open. COP path length was significantly greater (all $p<0.05$) for the environments with dynamic platforms/visuals.



Additionally these results were consistent for two approaches to assessing body segment sway: single marker trajectory and segment (multi-marker) trajectory. For all single markers (C7, T10, S2) and both segments (pelvis, torso), the paths were significantly greater for the same three conditions (all $p<0.001$). While further nuances may exist between lower and higher body segments (differing contributions of ankle and hip adjustments) this suggests that single marker approaches to segment movement during standing balance may be sufficient.

CONCLUSIONS

Frequency power and path length assessments were not able to discriminate between different age groups. However both metrics demonstrate increased postural sway responses for environments with dynamic visuals and platforms. Exposure to dynamic environments in VR may benefit individuals with balance impairments by providing safe conditions under which to practice balance responses.

REFERENCES

- Shaffer SW, et. al. Physical Therapy 87(2), 193-207, 2007
- Richardson J, et al. Archives of Physical Medicine and Rehabilitation, 86(8), 1539-1544.
- Jang, D., et al. IEEE Transactions on Information Technology in Biomedicine, vol. 6, 213-217, 2002.
- Liu, S. H., & Lawson, D. The Australian Journal of Science and Medicine in Sport, 27(3), 62-67, 1995.
- Pasma J. H. et al. J Neurophysiol. 2015 Dec 1; 114(6): 3220–3233.

Developing a Hand Brace of a Collegiate Basketball Player due to Injury: A Need for Identification of Hand Forces During Dribbling and Passing

Nicole Arnold¹, Nick Richey¹, Joshua Drost¹, Amber Vocelle¹, Justin Scott¹
and Tamara Reid Bush¹, PhD

¹Michigan State University, East Lansing, MI, USA

Email: reidtama@msu.edu

INTRODUCTION

Eighty-five percent of all hand fractures that occur in sports happen while playing ball related sports and about two thirds of these hand fractures are in the metacarpals [1]. Many athletes may return to play using a hand brace as long as the fracture is immobilized and protected, even following surgery. Proper protection using a brace requires an understanding of the forces that will be placed on that body region during play.

In this case study, a college basketball athlete sustained a left 4th metacarpal hairline fracture, which was surgically repaired with fixation using a pin. The athletic trainer asked for a brace design that would permit play after surgery and allow the individual to participate in the Big10 tournament and March Madness. Current knowledge about forces transmitted into the hand while handling a basketball is limited. The authors could not locate any published studies discussing forces and pressure transmitted to the hand during basketball play. Therefore, the goal of this work was to estimate the loads experienced by the hand during dribbling, during an aggressive two-handed single bounce (generally occurring prior to a shot and called a power dribble), during a crossover dribble and while receiving a chest pass. These data were then used to assist with brace design and material selection.

METHODS

Two male college basketball players, one with the injury and another with similar abilities, served as the participants for this work. Our team of biomechanics researchers took our equipment to the athletic training facility to conduct these evaluations. Two sets of force data generated by the basketball were collected. The first set consisted of data collected while dribbling where a teammate of the injured player executed various dribbling styles on the force plate (Bertec, Columbus, OH). The force plate was positioned on the

ground, which collected forces of three dribbling styles: normal dribble, crossover, and power dribble. The second data set was collected from a chest pass. To collect forces due to a chest pass, two feet on the base of the plate were removed, and a piece of unistrut was attached in their place. We placed the force plate on a nearly vertical section of a sports prep table that was mounted to the wall and recalibrated the plate. Two trials per dribbling style and three trials of a chest pass were conducted. Basic camera video was also recorded in each of these trials.

A 3D scanner (Sense 3D Scanner, Rock Hill, South Carolina) was used to obtain a scan of the physical features of the injured player's hand, which were used to produce a 3D model. The hand was scanned resting on a table with the thumb side up and hypothenar side resting on the table. Four different hand positions were scanned which included a posture to mimic when the hand was gripping the basketball, a semi-flexed, relaxed hand and the hand in handful extension.

RESULTS AND DISCUSSION



Figure 1: 3D Printed Model of Injured Athlete's Hand (left) and composite dorsal and palmer plates made for hand brace (right).

The maximum force of the ball transmitted into the force plate was used to calculate the maximum pressure that may be experienced by the hand (Table 1). Based on video evidence, we estimated

that the 2nd through 5th proximal and middle phalanges, the 1st distal phalange, the metacarpals, and the distal palm would initially contact the ball. Using the surface area of these regions, the overall pressures were calculated and are listed in the last column in Table 1. There are several limitations to this work. These include the estimate of the hand contact area. Also, we used the force as measured by the force plate which is an overestimation of the force into the hand as it does not account for the force reduction as it moves upwards against gravity. However, when compared to a study of peak hand pressures experienced by softball catchers (269kPa) our peak pressures were less than those by 48-78% [2].

Table 1: Forces and Calculated Pressures Transmitted into the Hand After Ball Handling

Dribble	Overall Force (N)	Overall Pressure (kPa)	Reduced Force (N)	Finger and Distal Palm Pressure (kPa)
Max	1652.8	78.6	1645.7	92.9
Min	1258.7	59.9	1252.6	70.7
Average	1403.3	66.8	1397.2	78.9
Two-Handed Dribble				
Max	1480.1	7.4	1474.0	83.2
Min	1187.8	56.5	1181.6	66.7
Average	1322.4	62.9	1315.3	74.3
Power Dribble				
Max	2488.5	118.4	2482.3	140.2
Min	1721.6	81.9	1715.5	96.9
Average	2067.6	98.4	2061.5	116.4
Pass				
Max	1022.5	48.6	1016.3	57.4
Min	540.9	25.7	534.8	30.2
Average	840.5	40.0	834.4	11.3

A CAD (computer aided design) file was created from the hand scans and a 3D printer was used to print a full-scale model of the athlete's hand (Figure 1 left). This model was used as a form to mold two composite

plates (Figure 1 right). The composite brace was developed from carbon fiber and epoxy which is lightweight, thin and durable. Thus, it was selected as the best material to protect the hand based on our initial load estimates. The brace consisted of two plates each on the palmar and dorsal sections of the hand. The athlete wore this brace, covered with thin foam padding and played in the tournaments.

CONCLUSION

We were able to obtain measures of loads into the floor and estimate the pressures experienced by the hand while executing several basketball movements. These force data fill a gap in existing literature. Further, by using the 3D hand scans, a brace was personalized for this player. Designing a customized brace in this fashion can help athletes that are not able to use an "off-the-shelf" brace system. Linking engineering and athletics is applicable to the biomechanics field because it helps athletes in need. This method also allows us to examine and treat those with unusual or specific need cases.

REFERENCES

1. Singletary, S, et al, *J. Hand Ther.*, vpp. 171–179, 2003.
2. Hicks, B, "A Comparative Analysis of Softball Gloves: Catcher's Glove Yields Highest Peak Hand Pressure," *Electron. Thesis Diss. Repos.*, 2015.

ACKNOWLEDGEMENTS

A special thank you to Xavier Tillman and Nick Ward for their participation.

RECUMBENT TRIKE: PREDICTING TOP SPEEDS BASED ON RIDER INPUT AND CONTRIBUTING POWER LOSSES

¹Antal K. Petrik and ¹Louis F. Vertosnik IV, ¹Alex C. Vertosnik, ¹Assel Al-Adayleh, ¹Andrew L. Sahlani

¹Cleveland State University, Cleveland, OH, USA

Email: akpetrik@gmail.com

INTRODUCTION

Recumbent bicycles have been around since the turn of the 20th century. These designs offer various rider advantages, including higher speed and comfortability. There are also ergonomic benefits due to a rider's weight being distributed over a larger surface area and more towards the rear drive wheel. Recumbent bikes became famous when biker Francis Faur broke the one-hour speed record in 1934 [1]. The efficiency and added speed appealed to the likes of many, producing many different styles and layouts. One such design is the so-called "tadpole" option, where one wheel is at the back driving the vehicle and two wheels are in the front to steer with. This provides better balance when turning at higher speeds.

The overall goals of this project were to (i) optimize the vehicle's weight and aerodynamics, (ii) reduce the amount of drag developed at higher speeds, and (iii) design a tricycle that could accommodate different anthropometric dimensions.

METHODS

Anthropometric measurements of the legs, height, arms, and shoulder width were obtained with the use of a tape measure, while weight was found using a digital weight scale. Riders' power outputs were measured through a 5 minute fitness test on an indoor Star Trac Pro 6430 HR Recumbent Bike (w/o click-in pedals). The test bike displayed power (watts) & rpm output on a real-time display screen. The fitness test consisted of 4 mins. of average pace followed immediately by 1 min. of maximum effort.

Following data collection, the chassis was modelled in Solidworks based around the anthropometric dimensions. A front, rear, and underbody fairing were then added to the model, along with a mannequin seated at the spec'd position.

Finite element analysis (FEA) was performed to simulate a loaded crank from a rider induced force. CFD analysis was performed using the Solidworks simulation package. The drag coefficient and drag force were found through this simulation. Then, the gear ratios of the vehicle were analyzed to determine which chain ring size would be optimal. Afterwards, the power loss due to drag, rolling resistance, and drivetrain efficiency were calculated for the heaviest and lightest rider and summed up to find the total power loss at any given speed for each. Then the average power loss was taken and plotted against speed, from 0 MPH to 35 MPH (at 5 MPH increments), deriving an exponential equation.

RESULTS AND DISCUSSION

The fitness test results can be found in Table 1. The two heaviest riders (riders 2 & 4) generate the most amount of power, but only deviate 16.04 ± 1.0 RPMs from the rest of the riders.

Table 1: Physical Fitness testing results.

Rider(s)	Average Output		Max Output	
	RPM	Watt	RPM	Watt
Rider 1	80	60	118	146
Rider 2	100	97	132	233
Rider 3	58	46	106	82
Rider 4	105	100	135	253
Rider 5	75	58	98	82
Average	83.60	72.20	117.80	159.20
STD Dev.	19.17	24.62	16.04	81.15

The CFD results provided a drag force of 4.698 lbf at 45 MPH along with a drag coefficient of 0.16. This drag coefficient proved to be essential in allowing the rider to reach greater speeds with less required effort.

After calculating velocity maps for the 3 different sized chain rings, it was determined that the 32T chain ring would provide the optimal range, ratio and best obtainable theoretic top speed.

The averaged total power losses seemed to exceed the watt capabilities of both the heaviest (Rider 4) and lightest (Rider 3) rider. Figure 1 shows this in a speed versus power graph, along with an exponential function being derived as the best fit line. Using this function, it was calculated that, at 35 MPH, neither of the 5 riders would be able to reach that speed based on their watt inputs in Table 1.

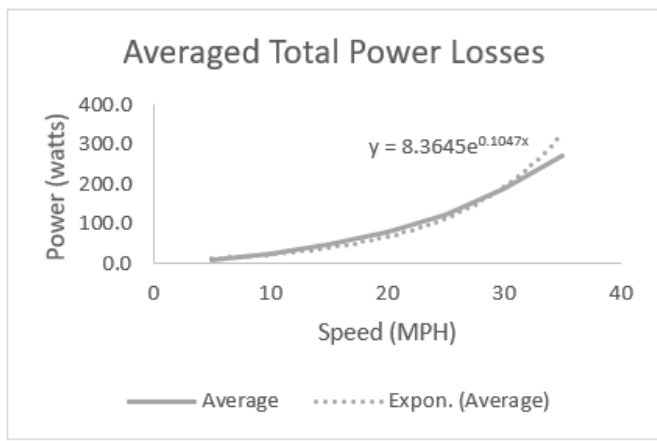


Figure 1: Averaged total power losses based on the slowest and fastest rider.

At average pace, Riders 1,3, and 5 would only reach approx. 17 MPH and Riders 2 and 4 would only reach 24 MPH. At maximum effort, Rider 1 would reach 27.3 MPH, Rider 2 would reach 31.8 MPH, Riders 3 and 5 would reach 21.8 MPH, and Rider 4 would reach 32.6 MPH. It is speculated that if the riders were to use clip-in pedals, they would generate more power due to having an extra pulling force attributed to their retracted leg.

CONCLUSION

Obtaining higher speeds on a recumbent tricycle is dependent on user input, gear ratios, aerodynamics, frame geometry and weight. These factors dictate power loss occurring in a human powered vehicle. It is especially crucial to minimize those power losses in a multi-rider team in order to have a balanced top speed range along with a higher cruising speed range.

Future considerations for the optimization of power losses and rider input range for the vehicle will focus around lowering the drag coefficient along with improving the physical fitness of the riders. Figure 2 provides a good representation of how the aerodynamics could be improved due to the current configuration producing more than desired amounts of turbulent flow up under the front fairing.

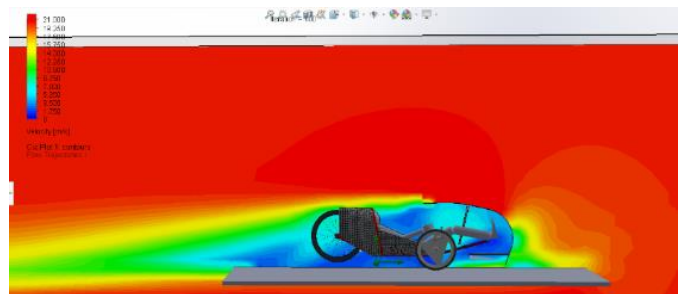


Figure 2: CFD analysis of front, rear, and under fairings at 45 MPH. Blue represents low velocity flow, green represents mid-range velocity, and red represents high velocity.

REFERENCES

1. Bicycleman, “History of the Recumbent Bike,” Bicycle Man, 11-May-2019. [Online]. Available: <https://bicycleman.com/history-recumbent-bike/>. [Accessed: 07-Feb-2020].

ACKNOWLEDGEMENTS

The Cleveland State University HPVC team would like to thank Dr. Kovach and Dr. Chattopadhyay for their guidance and support throughout the entire design and building process of the vehicle. The team would also like to acknowledge the USS Cod WWII Submarine Memorial and Museum for their donation towards build costs.

Eye-Hand Coordination During Functional Reaches

¹Jack Schultz (Presenter) and ¹Eric Schearer

¹Cleveland State University, Cleveland, OH, USA

Email: j.r.schultz12@vikes.csuohio.edu

INTRODUCTION

Individuals who are paralyzed from the shoulders down due to high-level (cervical C1-C4) spinal cord injuries (SCI) often have extreme difficulty performing everyday tasks such as feeding and grooming themselves. The majority of these individuals named recovering hand/arm function as the greatest priority for regaining independence [1]. Functional Electrical Stimulation (FES) is a promising method being explored to restore reaching movements to people with paralyzed limbs [2]. However, development of a non-invasive and reliable interface that allows a person to specify their intent for full arm reaching movements has been elusive. Accordingly, there is a critical need to develop a minimally invasive HMI that uses natural human actions to control complex reaching motions via FES. I present eye-tracking in this research as a suitable HMI due to its, intuitive control, and high sensitivity, and non-invasive nature. The overall goal of this research is to provide individuals with paralysis due to SCI the ability to control a functional neuroprosthesis with their eye movements. The objective of this study is to answer the research question: can a person use their eyes to control an effector to achieve desired positions in the presence of entangled feedback, and what is the effect of the feedback? We hypothesize that humans will be able to achieve desired target positions with their eyes and hand more accurately with feedback.

METHODS

We addressed the research question by measuring the positions of subjects' eyes during functional reaching tasks. We collected eye and hand data from 5 male subjects (age: 28 ± 2.9 years). Gaze data was

collected using a head-mounted eye-tracking system (iSCAN ETL-600) and hand data was collected using a 3D motion capture system (Optotrak 3D Investigator). All data communication was governed by a real-time target computer (dSPACE MicroLab Box). The subject was seated in front of a monitor that displayed fixation targets (Fig. 1). Targets were displayed using the OpenGL framework and the fixation shape was chosen based on previous studies [3]. All fixation times and locations were randomized. The reaching pattern resembled a center-out task but was constrained to the horizontal or vertical directions in this study to avoid contradictory arm configurations.

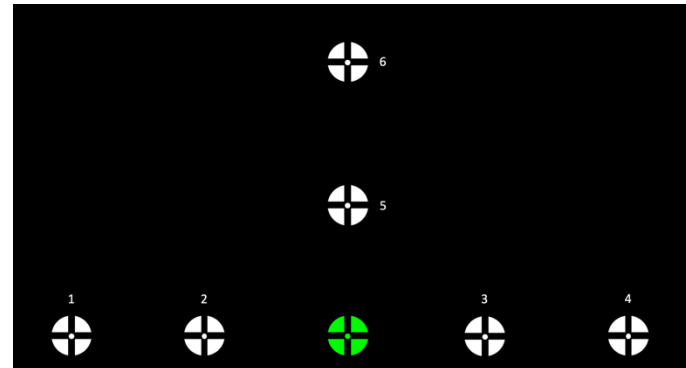


Figure 1: Depiction of fixation target locations. Numbered targets are fixation targets, with randomized order and fixation times. The green target is the default target position.

Four experimental conditions were included: 1) Eye-Alone without feedback, 2) Eye-Alone with feedback, 3) Eye-Hand without feedback, 4) Eye-Hand with feedback. The eye-alone conditions consisted of only looking at the targets while the eye-hand conditions included reaching as well. The feedback was a crosshair cursor located at the current gaze position of the subject. During the 'without feedback' conditions, the subject was instructed to

look and/or reach naturally, while during the ‘with feedback’ conditions, the subject was instructed to move the cursor to the target position. The objective of this study was to determine if the subject could achieve target positions by controlling a cursor with their eyes, and what strategies they employed to complete the task. To answer the research question, we compared the root mean squared error (RMSE) of achieving the target locations with the eyes and hand between the ‘without feedback’ and ‘with feedback’ experimental conditions. All data analyses were performed using MATLAB 2019a. Statistical analyses were performed using IBM SPSS.

RESULTS AND DISCUSSION

At the time of submission, data from one subject was analyzed. With the addition of feedback, the RMSE of the eyes *decreased* for the ‘EyeAlone’ Condition from 9.87 to 5.98 mm in the x-direction and *decreased* from 48.81 to 14.48 mm in the y-direction. For the ‘EyeHand’ condition, the RMSE of the eyes *decreased* from 12.93 to 4.73 mm in the x-direction but *increased* from 78.56 to 113.72 mm in the y-direction. The RMSE of the hand *increased* from 9.37 to 9.76 mm in the x-direction and *decreased* from 4.48 to 3.88 in the y-direction (Fig. 2).

RMSE During Functional Reaching

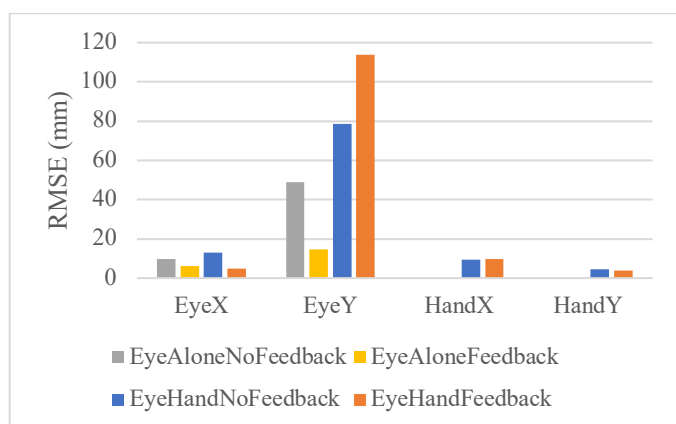


Figure 2: RMSE between intended target and measured parameter during each experimental condition.

Because only one subject’s data had been analyzed at the time of submission, no statistical analysis

could be performed. However, the results display a trend of decreasing RMSE with the addition of feedback. This result supports our hypothesis that humans are able to achieve a desired target position with their eyes and hand in the presence of entangled feedback. A notable exception to this trend is the RMSE of the eyes in the y-direction during the ‘EyeHand’ condition. By qualitative analysis, we observed that the measured data for the eyes was much noisier in the y-direction than in the x-direction. This can also be seen in the higher RMSE for the eyes in the y-direction than in the x-direction across all conditions. This observation can be attributed to the fact that y-direction changes in the eye’s position are much more sensitive to noise than the x-direction.

CONCLUSION

In this study, the cursor feedback was meant to resemble a robot or human arm under neuroprosthetic control. The results of this study suggest that humans are able to accurately achieve target positions in the presence of entangled feedback, however more data is needed to say this conclusively. Future studies will extend this work to 3D environments and to implement adaptive cursor dynamics to further improve accuracy and to increase stability.

REFERENCES

1. Anderson, K, et al. *Journal of Neurotrauma*. 1371-1383, 2004.
2. Ragnarsson, K, et al. *Spinal cord*, 255–274, 2008.
3. Thaler, L, et al. *Vision Research*, 31-42, 2013.

ACKNOWLEDGEMENTS

We would like to thank the Cleveland State University Office of Research for their support of this study. We would also like to thank Dr. Andrew Slifkin (Cleveland State University Psychology Department) for his help with the experimental design.

Transition to Turbulence in an Eccentric Stenosis for Whole Blood Under Steady Flow Conditions

¹Junyao Yao, ¹Rayanne Pinto Costa, ²Dipankar Biswas and ¹Francis Loth

¹University of Akron, Akron, OH, USA

²University of Central Florida, FL, USA

Email: jy62@zips.uakron.edu

INTRODUCTION

A stenosis is a restriction in the artery which reduces blood flow and is associated with heart attacks and strokes. To predict the biological response to the stenosis, it is important to understand the solid and fluid dynamics interaction. Blood is a suspended fluid composed of 45% blood cells and exhibits a non-Newtonian fluid behavior at a low shear rates ($<200\text{s}^{-1}$) and a near Newtonian fluid behavior at a high shear rate. Biswas et al. (2016) conducted a straight pipe experiment to demonstrate a 20% delay of the critical Reynolds numbers for blood compared with a Newtonian fluid [1]. Khan et al. (2017) used direct numerical simulation to investigate the evidence of the stabilizing effect of shear thinning, a non-Newtonian property of the blood, in an eccentric stenosis and how it affects the critical Reynolds number [2]. The DNS simulation was done at Reynolds number 500-1000. They found that the Newtonian fluid transitioned at $\text{Re}=700$ and the blood transitioned at $\text{Re}=800$. We sought to verify the delay in transition in the same eccentric stenosis geometry experimentally.

METHODS

Five samples of water-glycerin (48% glycerin by volume) with titanium dioxide particles and five samples of porcine blood (100ml 3.66% sodium citrate solution was added into each 900ml blood) were tested in an in vitro system. A drawing of the system is shown in Figure 1. Samples were preheated to 37° Celsius before loading the system. The fluid was driven by centrifugal pump from the reservoir through a 6.35mm diameter plastic pipe. Temperature was maintained at 37° Celsius using a

computer-controlled system comprised of a heat exchanger and electric heater. Velocity profiles were measured at 21 points with a 0.175mm step size across the pipe. Velocity was measured by a 60 degrees Doppler ultrasound probe after the fluid passed through the stenosis with a 75% area reduction. The model of the stenosis is shown in Figure 2. The Doppler ultrasound probe was placed 11 diameters downstream of the stenosis. The velocity of each point was taken as an average of a three-second measurement. The flowrate was monitored by an ultrasonic flowmeter. The rheological properties of fluid were measured by a TA Instrument AR2000EX rheometer with the shear rates from 10 to 1000s^{-1} . The viscosities at 1000s^{-1} were used in the calculation of Reynolds number.

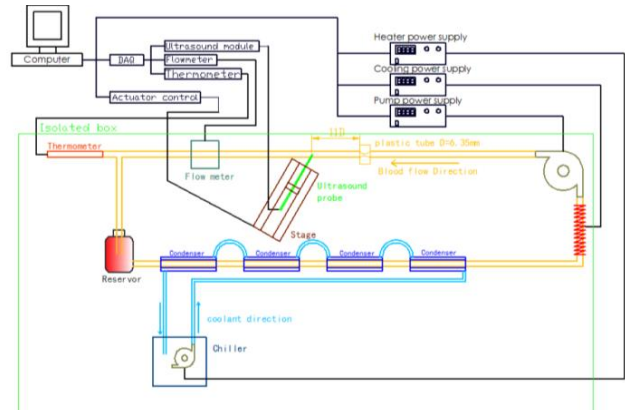


Figure 1: Drawing of the experimental system



Figure 2: Eccentric stenosis model

RESULTS AND DISCUSSION

Velocity profiles downstream of the stenosis are shown for water-glycerin and whole blood in Figure 3. Each measurement point shows the mean velocity and standard deviation in the same figure. TKE (Turbulence Kinematic Energy) is used to determine the critical Re for the transition to turbulence (Figure 4). Critical Re was identified as corresponding to the highest TKE. The results show that the mean critical Re of the blood sample is 472 while the mean critical Re is 395. It demonstrates that blood has a 20% delay compared to water-glycerin for the transition to turbulence using the TKE approach.

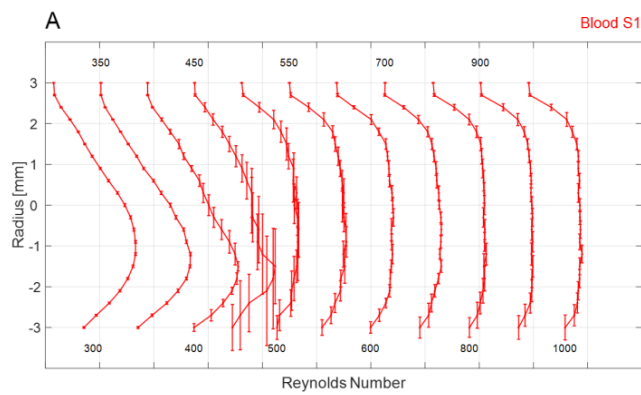
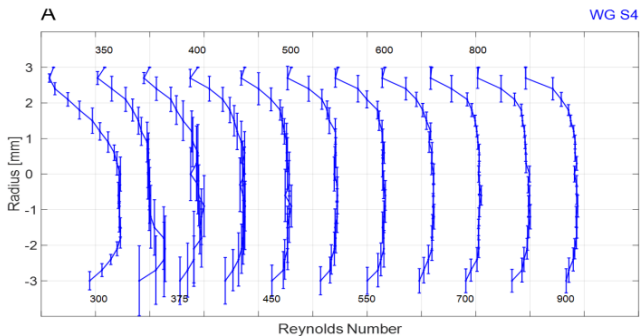


Figure 3: Velocity profiles measured by Doppler ultrasound.

DISCUSSION

Dave Casey completed an experiment in 2016 with the same eccentric stenosis. However, his results were not consistent due to imperfection in his stenosis geometry. The geometry utilized in the present study was manufactured in such a way to minimize geometric imperfections. [3]. The present results demonstrate good agreement with the work

of Khan et al. While they found a larger critical Reynolds numbers than the present study ($Re=700$ for Newtonian and $Re=800$ for blood), the differences between critical Re for water-glycerin and blood were similar ($\Delta Re \sim 90$). It is expected that experimental results would have a smaller critical Reynolds number than numerical simulations since imperfections in the geometry and inlet flow condition in the experiment can be amplified. Numerical simulations have perfect geometry and inlet flow conditions. Future studies should examine the pulsatile flow conditions and tissue compliance effects.

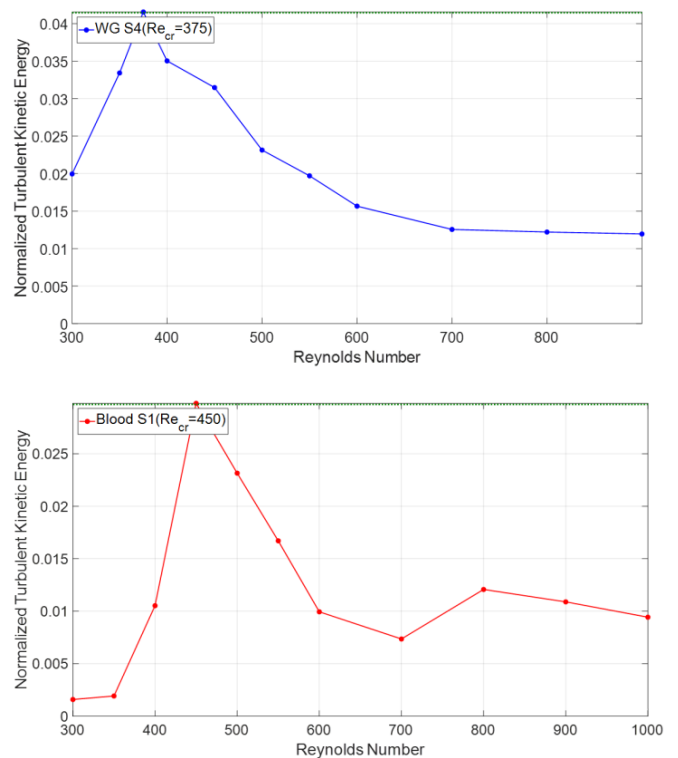


Figure 4: Normalized TKE vs. Reynold number.

REFERENCES

1. Dipankar Biswas et al., Journal of Biomechanical Engineering
2. Khan et al., (2019) 102:43–72. Volume 102
3. Casey, MS thesis, University of Akron

TRANSITION TO TURBULENCE FOR NON-NEWTONIAN FLUID IN A STRAIGHT PIPE UNDER STEADY AND PULSATING FLOW CONDITIONS

¹Rayanne Pinto Costa, ¹Junyao Yao, ⁴Dipankar Biwas, and ¹Francis Loth

¹University of Akron, Akron, OH, USA

⁴University of Central Florida, FL, USA

Email: rp98@zips.uakron.edu

INTRODUCTION

Blood is a complex liquid with a large volume fraction of solid particles which is responsible for blood's non-Newtonian characteristics. However, when trying to model blood flow inside arteries, vessels and other biological components using numerical simulations, a Newtonian assumption is often employed. Researchers have considered blood to have a shear thinning behavior under a shear rate of 200s^{-1} and a Newtonian behavior at higher shear rates [1]. A study reported whole blood has a delay in transition to turbulence compared to a Newtonian fluid under steady flow conditions [2]. However, blood in the human body is pulsatile. Thus, it is important to verify if this delay is present under pulsatile flow conditions.

METHODS

This study aims to examine the transition to turbulence behavior for whole blood inside a rigid straight pipe under steady and pulsating flow conditions. The critical Reynolds number will be evaluated based on the measured velocity profiles using the PSI (Profile Shape Index) and TKE (Turbulent Kinetic Energy). The steady flow study measured velocity for three seconds at each point on the profile. The fluid was put in a reservoir and a centrifugal blood pump (Sarns Disposable Centrifugal Pump 7850) pumped the fluid through the testing area where a pulsed Doppler ultrasound probe measures fluid velocity at 21 points along the pipe diameter. The flow rate was measured by a transit time flow meter and a computer controlled

power supply. The fluid temperature was maintained in a range between 36.5-37.5°C and computer-controlled using an electric heater, a heat exchanger, and a digital thermometer.

The steady flow measurements were made in the Reynolds number range of 900-3400 for 21 locations across a 6.35 mm diameter pipe in water-glycerin (WG, 52:48) and whole blood. The WG is a Newtonian fluid with similar viscosity as the blood at high shear rates ($>1000\text{s}^{-1}$). Viscosity measurements were performed using a AR2000ex rheometer (TA Instruments) to obtain the viscosity at a shear rate of 1000s^{-1} . This viscosity was used to calculate the flow rate needed to reach the desired Reynolds number during the experiment. For the pulsatile flow studies, a piston will be connected inline and downstream of the steady flow centrifugal pump to obtain the pulsatile flow. For 1Hz pulsatile waveform, 20 seconds of data will be recorded and an ensemble averaged waveform will be computed. Turbulence will evaluated at acceleration, peak, deceleration and minimum flow condition during the cardiac cycle and compared between whole blood and WG.

RESULTS AND DISCUSSION

The average viscosity and density for WG and whole blood were 4.1 & 4.0 cP and 1.1 & 1.1 g/cm³, respectively. The velocity profiles in steady flow for the WG and whole blood are shown in Figure 1. The profile starts out parabolic and becomes blunt at Reynolds number near 3257 for blood and 2793 for WG, which indicates transition to turbulence.

The PSI compares the laminar and the turbulent velocity profiles and the intersection provides an estimate of the critical Reynolds number [2]. For blood, the Re_{cr} was 3094 and for WG, the Re_{cr} was 2826 (Figure 2).

The TKE in steady flow for the WG and blood is shown in Figure 3. Critical Reynolds number is considered to be at the peak TKE value [2]. For the WG, Re_{cr} was 2790 and for blood, it was 3052.

The blood had a delay of 9% compared to the WG using PSI and TKE methods.

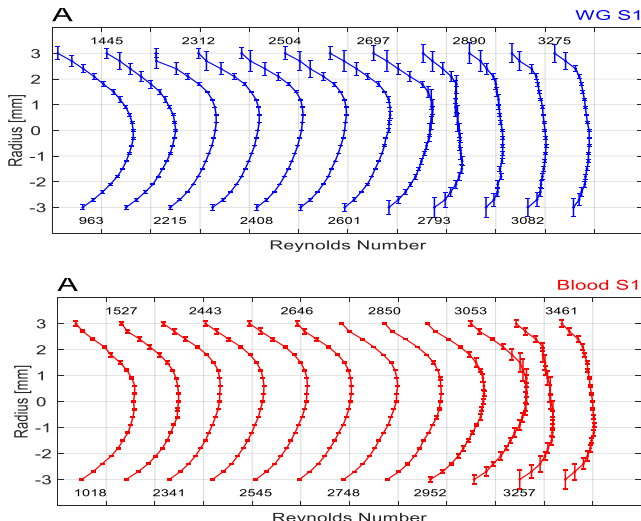


Figure 1. WG and blood velocity profile comparison.

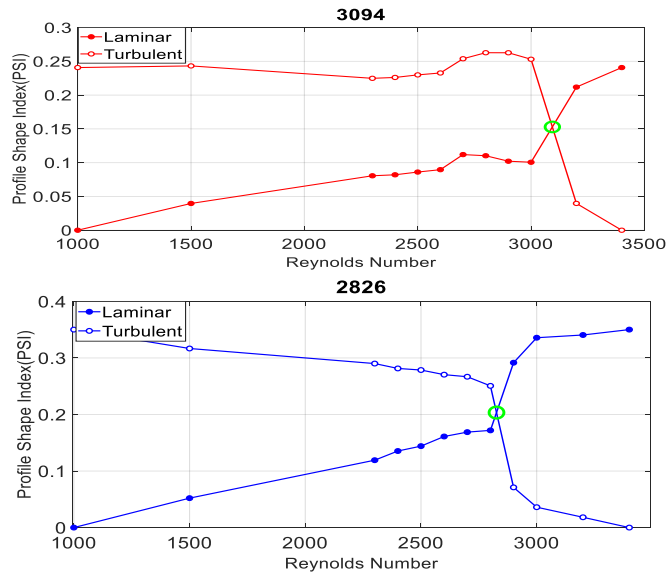


Figure 2. PSI comparison for WG and blood.

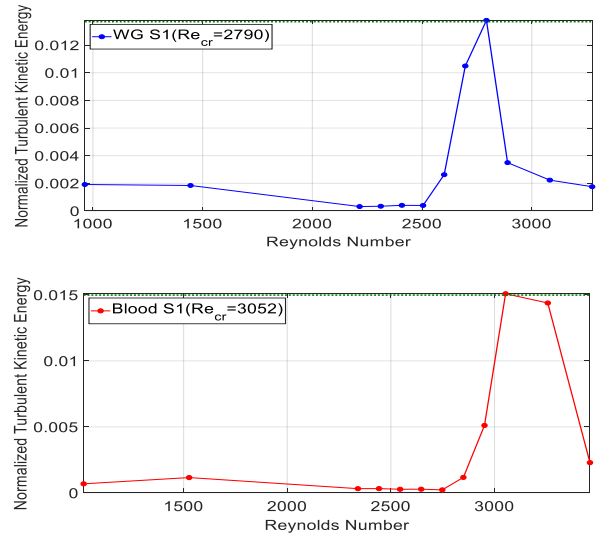


Figure 3. TKE comparison for WG and blood.

The same methods to obtain the critical Reynolds number in steady flow will be used for the pulsatile flow to verify if this delay in transition to turbulence also occurs. However, pulsatile flow will go through a range of Reynolds during the cardiac cycle. Thus, we will use mean Reynolds number to define the flow and determine where in the cardiac cycle transition begins (i.e. acceleration, deceleration).

CONCLUSION

The PSI and TKE method revealed that blood have a delay in the critical Reynolds number compared to WG (Newtonian fluid) of 9%. Pulsatile experiments are ongoing may demonstrate less differences in critical Reynolds number than that for steady flow since turbulence needs time to develop and the unsteady nature of pulsatile may disrupt this development.

REFERENCES

1. Casey, D. 2014. Master thesis. University of Akron, Akron, OH.
2. Biswas et al., *Journal of Biomechanical Engineering*, ASME, 2016.

CHARACTERIZATION HUMAN OSTEOBLAST CELLS ON 3D PRINTED TITANIUM: DEVELOPMENT OF AN IN VITRO BIOASSAY SYSTEM¹

Sarah Seman^{1,2}, Brianna Holst¹, Dr. Rocco Rotello³, Timothy L Norman¹

¹School of Engineering and Computer Science

²School of Science and Mathematics

³School of Pharmacy

Cedarville University, Cedarville, OH, USA

Email: tnorman@cedarville.edu

INTRODUCTION

The osteoinductive characteristics of surfaces constructed from 3D printing of metals is an emerging area of study. Work from previous investigators has shown that 3D printed titanium is biocompatible and demonstrates successful osteointegration [1-5]. Gulati et al. [1] concluded that micro and nano-scale surface topography improves cell proliferation. In the current study, the maintenance and characterization of human osteoblasts (large T-antigen transfected) on 3D printed titanium surfaces was undertaken. This study involved testing the growth and survival of osteoblasts after attachment to artificially generated surface with variations in roughness of 3D printed disks made from Titanium. The disks were designed to include variations in magnitude and frequency of surface topography features. The goal of this study is to identify surface features obtainable from the variables of 3D printing that are optimal for 3D printed titanium implants.

METHODS

Test specimens consisting of 20 mm diameter disk (Fig. 1) were design using NToplogy Platform (New York, NY). The disks were constructed such that they were divided into 8 wedges with each wedge differing by the frequency or magnitude of peaks defining the surface roughness topology. Each disk included a blank surface, which represents the smoothest surface printable by the additively manufactured selective laser melting techniques utilizing with a printing resolution of 0.15 mm. The disks were printed by Tangible Solutions (Fairborn, OH). The disks are defined by four groups: a) magnitude of peaks ranging from 0.35-0.36 mm, b) magnitudes of peaks ranging from 0.15-0.3 mm, c) the frequency of peaks form 3k-4.5k and d) the frequency of peaks ranging from 4k-10k. To date, two samples of each of the above disk configurations

were printed. After printing, the disks were sterilized in 70% isopropyl alcohol for 24 hours then air-dried in a HEPA filtered BL-2 Biosafety cabinet. The last step in sterilization included a two hour UV irradiation in the BL-2 biosafety cabinet. Throughout the study, all recommendations for culturing and passaging of large T antigen transfected human osteoblasts (CRL-11372) by the ATCC were followed. Individual 3D printed disks placed in a 6-well plate with five mL of complete growth media Dulbecco's and F12-mixture, 10% fetal bovine serum, G418 50 mg/ml, incubated at 37 °C and new media added every two days. After one week of culture the disks were removed from media, fixed in freshly prepared 2% PBS-buffered paraformaldehyde for 15 minutes at room temperature. Variations in magnitude and frequency of peaks and Disks with attached cells now fixed to the scaffold were rinsed with PBS twice, for five

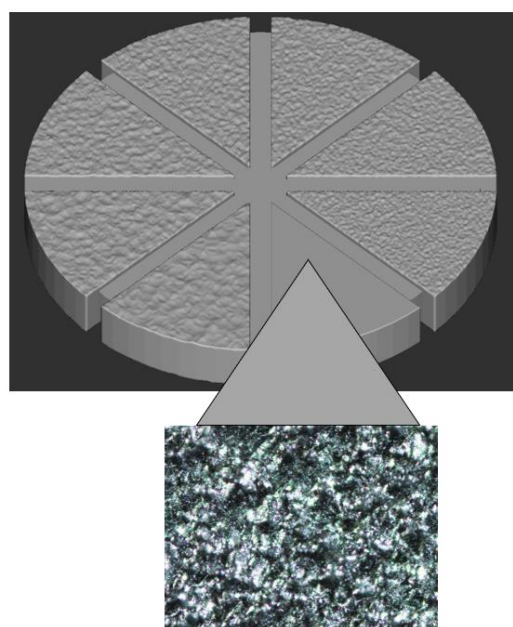


Fig. 1.
Example of
surface
roughness
disk with
image of
microscopic
topography of
the “blank”
portion

minutes. The disks were then stained with a DNA dye, Hoechst dye 33248 and imaged using Nikon Ti90 fluorescent microscopy. Each section/plane of the disk was

counted using three similarly placed, randomly selected viewing windows with an area of 0.0095 mm^2 . These counts were then averaged by comparing with ANOVA to determine if significant differences exist among and within groups. Pairwise comparisons were made using Tukey Kramer. All statistical analysis was performed using the statistical software package JMP (SAS Institute, Cary, NC). Significance was set for $p < 0.05$.

RESULTS

Large T antigen transfected human osteoblast cells were found to survive, proliferate and maintain phenotype on all 3D printed surfaces (Figure 2 – a picture of cells of the disk – the one Brianna captured). Cell counts varied by group (Figure 3). The 0.15-0.30 magnitude group had significantly ($p < 0.05$) higher cell counts than the disks with magnitude of 0.35-0.36 and with a frequencies ranging over 3k-4.5k. There were no significant variations in cell counts within groups (Figure 4).

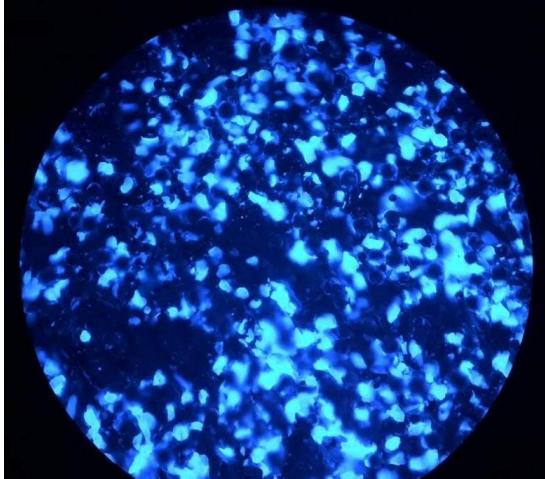


Figure 2. Picture of Cells on disk

DISCUSSION

Disk that have variations in the surface roughness have been shown to have no adverse properties that prevent cells from adhering and surviving. Cells can survive for extended periods of time with no change in morphology or phenotype. Significant attachment occurs without variation in location of attachment. Statistical analysis (ANOVA) shows that there were significant differences between disks but not within disks. This is likely due to the small magnitude of variation within each disk with features too large to have a significant impact on cell growth. However, due to the nature of 3D printing, the surfaces all had some level of baseline roughness that seems conducive to cell growth, as demonstrated by the moderate to high numbers found on the “blank” surfaces.

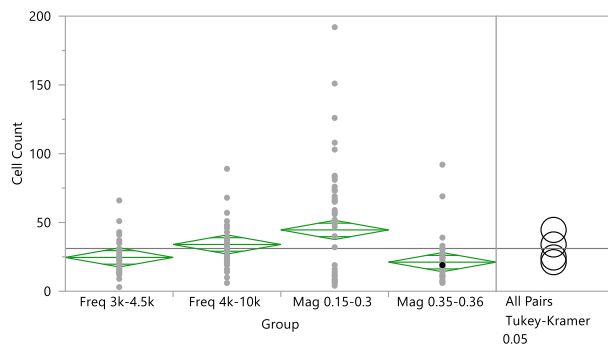


Figure 3. Cell counts by disk.

Oneway Analysis of Cell Count By ID

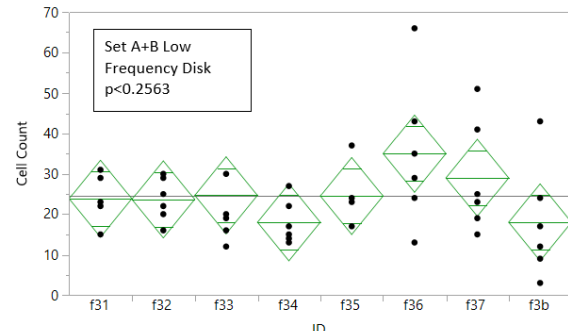


Figure 4. Cell counts on the 3k-4.5k frequency disk, Blank specimen far right.

CONCLUSIONS

In conclusion, large T antigen transfected human osteoblasts survive, proliferate and maintain phenotype on 3D printed titanium specimens. This initial observation has established an in vitro bioassay to determine cell growth on surfaces with different roughness. The goal of the first experiment was to determine if a 3D printer with a resolution of (0.15mm) could generate surfaces with enough variation on a scale that impacts cell growth. Upon analysis of the six area counts from each surface type, there is no statistical significance in cell growth between the differing surfaces.

REFERENCES

- [1] Gulati, K. et al. (2016). *Journal of Tissue Engineering and Regenerative Medicine*, 11(12), 3313–3325. doi: 10.1002/tterm.2239
- [2] Tedesco et al. (2017) *International J. of Dentistry*. Vol. 2017.
- [3] Wei,Zu et alos *J Mater Sci: Mater Med* (2017) 28:62
- [4] Shah, F.A. et al. *Acta Biomat.*, 30 (2016), 357-367.
- [5] Nune, KC et. al, *J of Bio. Mater. App.*, (2018) Vol. 32(8).

ACKNOWLEDGEMENTS

The authors would like to recognize Tangible Solutions in Fairborn Ohio for their donation of the materials and printer use to make the titanium specimens used in this study.

SENSITIVITY OF SWING TOE HEIGHT TO JOINT ANGLES OF BIPEDAL LINKED CHAIN DURING OBSTACLE CROSSING

¹Chuyi Cui, ^{2,3}Brittney Muir, ¹Shirley Rietdyk, ¹Jeffery Haddad, ⁴Richard van Emmerik, ¹Satyajit Ambike

¹ Purdue University, West Lafayette, IN, USA

² University of Washington, Seattle, WA, USA

³ RR&D Center for Limb Loss and MoBility (CLiMB), Seattle, WA, USA

⁴ University of Massachusetts, Amherst, MA, USA

Email: cui111@purdue.edu

INTRODUCTION

Tripping while walking is a main contributor to falls [1]. Tripping frequency is related not only to the elevation of the swing toe above the ground or an obstacle, but also to the variance in the swing toe height [2]. To identify the source of this variance, the sensitivity of the swing toe height to changes in the limb joints has been quantified. However, sensitivity calculations have been restricted as follows: sagittal-plane angles only [4], swing limb only [4], or overground walking only [3, 4].

Therefore, the aims of the present study are (1) to quantify the sensitivity of swing toe height to sagittal and frontal plane joint angles during overground walking and while crossing obstacles of varying height, and (2) to compare the sensitivities of groups of angles. We hypothesize that the swing toe height is most sensitive to stance hip ab/adduction, and sensitivity will be different when the lead versus trail foot crosses an obstacle.

METHODS

Ten healthy young subjects (23.8 ± 3.4 years, 3 female) crossed an obstacle (0, 3, 10, and 26 cm tall) on a 15 m walkway with self-selected lead foot. Each task was repeated 10 times. Whole-body kinematics were measured using the Qualysis motion capture system (Qualysis Inc., Gothenburg, Sweden). Sensitivity of the toe height to the lower-limb joint angles were determined at minimum toe clearance for unobstructed gait (no obstacle, 0 cm), and when the

first and the second foot crossed the obstacle (called lead and trail subtasks).

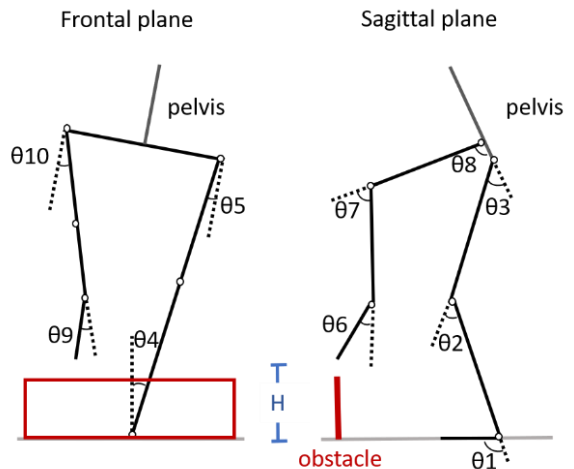


Figure 1: Lower-limb joint angles that influence toe height.

The swing toe is the end point of a linked chain (Fig. 1). The function relating the toe height (H) to the lower-limb joint angles (θ_i , $i=1$ to 10) was written: $H=f(\theta)$. The Jacobian of f was derived: $J=[\partial H/\partial \theta_1 \ \partial H/\partial \theta_2 \dots \ \partial H/\partial \theta_{10}]$ and evaluated by substituting the measured values of the joint angles. The values in J are the changes in H due to a unit change in an angle, i.e., the sensitivities of H to individual angles.

Sensitivity of H to a group of angles was quantified as the singular value of the Jacobian comprising of the partial derivatives with respect to those angles. For example, the singular value of $J_{\text{frontal}}=[\partial H/\partial \theta_4 \ \partial H/\partial \theta_5 \ \partial H/\partial \theta_9 \ \partial H/\partial \theta_{10}]$ yields the maximum possible change

in H due to the vector $[\partial\theta_4 \ \partial\theta_5 \ \partial\theta_9 \ \partial\theta_{10}]$ of unit magnitude, and it is defined as the sensitivity of H to the frontal plane angles. We compared singular values for the stance and swing limb angles and for the sagittal-plane and frontal-plane angles. All sensitivity values are averaged across the 10 trials for each subtask. Sensitivity to individual joint angles was analysed with *joint* \times *subtask* \times *obstacle height* ANOVA. Sensitivity to joint angle groups was analysed with *subtask* \times *obstacle height* \times *plane* and *subtask* \times *obstacle height* \times *limb* ANOVAs.

RESULTS AND DISCUSSION

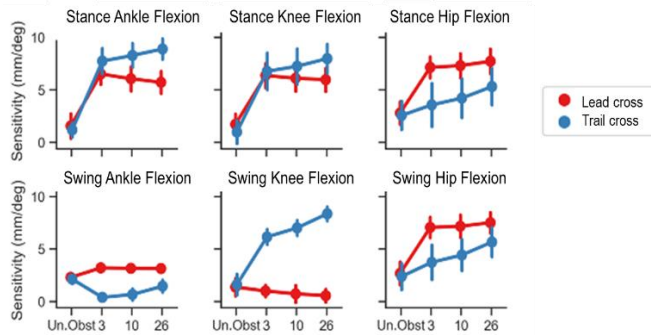


Figure 2: Mean \pm SD of toe height sensitivity for each joint angle in the sagittal plane.

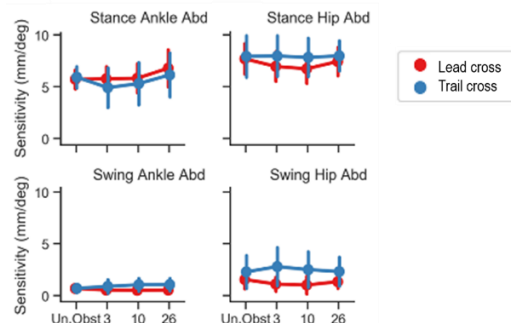


Figure 3: Mean \pm SD of toe height sensitivity for each joint angle in the frontal plane.

All joints influenced the toe height. The influence of swing ankle ab/adduction is small compared to other joints (Fig. 3). Toe height was most sensitive to stance hip ab/adduction, stance ankle flex/extension and stance ankle ab/adduction. Sensitivity to a few joints (e.g. swing knee flex/extension) was higher for trail subtask than lead subtask whereas the opposite was observed for other joints (e.g. swing ankle flexion) (three-way interaction effect: $F(27,711) = 7.12$, $p<.001$; Fig. 2,3).

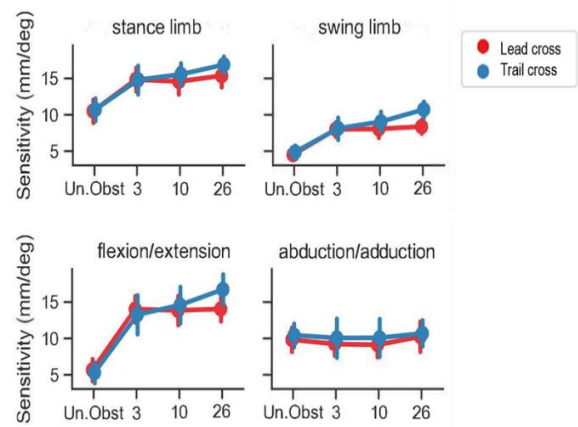


Figure 4: Mean \pm SD of toe height sensitivity to groups of joint angles.

Toe height was more sensitive to the stance limb joints than the swing limb joints for unobstructed gait and for all obstacle heights (main effect: $F(1,135)=912.9$, $p<.001$). Sensitivity was similar for the two subtasks for unobstructed and 3 cm obstacle for both limbs, but it was higher for the trail subtask for 10 and 26 cm height obstacle (*subtask* \times *obstacle height* interaction effect: $F(3,135)=3.21$, $p=.025$).

Toe height was more sensitive to the frontal plane angles than the sagittal plane angles for unobstructed gait, but this relation is reversed during obstacle crossing (*plane* \times *obstacle height* interaction effect: $F(3,135)=53.1$, $p<.001$).

CONCLUSION

When individuals/patients report increased frequency of tripping, weakness or impaired coordination in the ab/adductors should be considered. Furthermore, interventions should not be limited to the swing limb, as the joints of the stance limb had a greater influence on the toe height than the swing limb across all locomotor tasks observed here.

REFERENCES

- [1] Berg, WP et al. *Age and ageing*, 26(4), 261-268, 1997.
- [2] Barrett, RS et al. *Gait & posture*, 32(4), 429-435, 2010.
- [3] Winter, DA. *Physical therapy*, 72(1), 45-53, 1992.
- [4] Moosabhooy, MA et al. *Gait & posture*, 24(4), 493-501, 2006.

STRUCTURE OF VARIANCE IN FINGER FORCES VARIES ACROSS TRACKING TASKS WITH DIFFERENT TASK UNCERTAINTY

¹Paige Thompson (Presenter) and ¹Austin Cooper, ¹Laura Claxton, ¹Satyajit Ambike

¹Purdue University, West Lafayette, IN, USA

Email: thomp732@purdue.edu

INTRODUCTION

Motor systems are often redundant, with multiple input variables contributing to a fewer number of output variables defining a motor tasks. Redundant motor systems display compensatory behavior in which errors generated by some input variables are compensated by changes in others so that the task-specific output variables are stabilized. Such synergistic covariation in input variables has been observed for several motor behaviors [1].

Synergies that stabilize task variables will resist any volitional changes in those variables as well. However, anticipatory synergy adjustments (ASAs) are seen in many tasks: synergies weaken when individuals prepare to voluntarily change their motor state [2]. It was recently established that ASAs occur in response to the mere expectation of an upcoming change and even when there is uncertainty in the timing and the nature of the upcoming change, indicating that ASA is a generalized form of preparation that could facilitate the performance of several potential motor actions [3]. ASAs can occur due to lower task-specific covariation, or higher variability in the task variables, or both.

The objective of this study was to investigate if individuals prepare similarly for motor transitions with and without uncertainty. We hypothesized that ASAs for tasks with and without uncertainty will be similar, and will occur through similar mechanisms.

METHODS

Ten young, healthy, right-handed participants (21.3 ± 2.6 years; mean \pm SD) participated in this study. Participants were seated comfortably at a table, and

they produced downward pressing forces with the distal phalanx of their right-hand fingers pressing on four force sensors (Nano 17, ATI Automation, Garner, NC). They produced a single total force (F_T) which was the sum of the forces of the fingers to track force targets presented on a computer screen. Participants performed three types of tracking tasks. In the steady task, a square target was displayed at 10% of the participant's maximum voluntary contraction (MVC, measured earlier). Participants knew that the target will not move for this task. In the uncertain task, trials began with the square force target at 10% MVC, which then began moving vertically after a random time interval. The participants were informed that the target will begin to move at any time and in any direction. In the certain task, the two horizontal lines at 10% and 20% MVC represented the target. The 10% line stretched from the left edge up to the midline of the screen, and the 20% line stretched from the midline to the right edge. The target lines were visible at the start of each trial. The participant's F_T was represented as an 'X', which they modulated to match the target box in the steady and uncertain tasks. For the certain task, the 'X' moved from left to right on the screen with time, and the participant first matched the 10% MVC line, and then produced a rapid F_T pulse to the 20% MVC line when the 'X' reached the midline of the screen. Each task was repeated 15 times to yield a distribution in the space of finger forces.

The finger force data from the portion of the trials when the targets were at 10% MVC were analyzed using the uncontrolled manifold (UCM) method [3]. Participants are producing roughly the same F_T , but their expectation of future movements and the

uncertainty in those movements is modulated across the task types. The across-trial variance in the finger forces was partitioned into a component that does not change F_T (variance along the UCM, V_{UCM}) and a component that changes F_T (variance orthogonal to the UCM, V_{ORT} ; Fig. 1). A synergy index was computed as $\Delta V = (V_{UCM}-V_{ORT})/(V_{UCM}+V_{ORT})$, which was then z-transformed (ΔV_z) to meet normality requirements. A positive synergy index implies $V_{UCM} > V_{ORT}$, and indicates the presence of a synergy. Higher ΔV_z indicates stronger synergy between the finger forces, and vice versa. A reduction in ΔV_z for the certain/uncertain tasks compared to the steady task (i.e., the difference variable $\Delta\Delta V_z$) is the ASA. Furthermore, we quantified the change in the variance components across the certain/uncertain tasks and the steady task: $\Delta V_{UCM\text{-certain}} = (V_{UCM\text{-certain}} - V_{UCM\text{-steady}})/V_{UCM\text{-steady}}$, $\Delta V_{UCM\text{-uncertain}} = (V_{UCM\text{-uncertain}} - V_{UCM\text{-steady}})/V_{UCM\text{-steady}}$, and similarly for V_{ORT} . One-sample t-tests were used to test if the difference variables $\Delta\Delta V_z$, ΔV_{UCM} and ΔV_{ORT} were significantly different from zero. $\Delta\Delta V_z > 0$ will indicate the presence of ASA, and significant changes in V_{UCM} and V_{ORT} will indicate the change in the variance structure, i.e., the specific mechanisms that yield $\Delta\Delta V_z$.

RESULTS AND DISCUSSION

$\Delta\Delta V_z$ was not significantly different from zero for either the certain or the uncertain task ($t_{(9)} > 0.11$; $p > 0.49$), indicating that ASA was not observed in our data. Thus, our data does not support our hypothesis that similar ASAs will be observed in tasks with and without uncertainty.

However, task uncertainty had a striking effect on the variance structures. The variance components for the certain task were not different from the components for the steady task ($t_{(9)} > 1.4$; $p > 0.11$). In contrast, V_{UCM} and V_{ORT} were significantly larger for the uncertain task compared to the steady task ($\Delta V_{UCM\text{-uncertain}}$ and $\Delta V_{ORT\text{-uncertain}} > 0$, $t_{(9)} > 2.7$; $p < 0.05$). Thus, the absence of ASA for the certain task arose

from consistent variance components across the two tasks, whereas the absence of ASA for the uncertain task arose from compatible increases in V_{UCM} and V_{ORT} in the uncertain task that leave ΔV_z invariant across the two tasks (Fig. 1). Increased V_{UCM} has been associated with greater flexibility of task performance, and greater V_{ORT} has been associated with lower task stability [1,2,3]. Both these mechanisms likely assist in the preparation for the uncertain change in total force. Thus, our hypothesis that the ASAs for tasks with and without uncertainty will be achieved via similar changes in the structure of variance was not supported.

CONCLUSION

There is minimal preparation for a well-defined, certain change in the total force produced by the four fingers. In contrast, preparation for an uncertain, ill-defined change in the total force leads to more flexible finger force patterns (higher V_{UCM}) and lower stability of the total force (higher V_{ORT}).

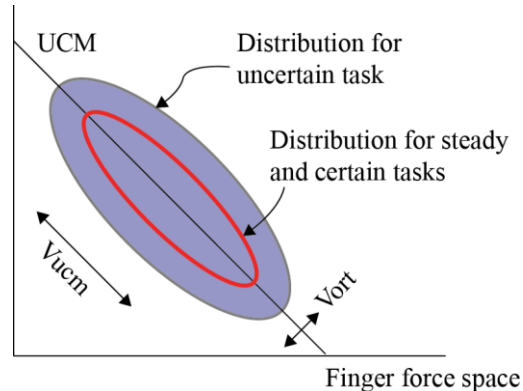


Figure 1: Finger force distributions indicating synergies that stabilize total force. Red ellipse is distribution for the steady and certain tasks. Large ellipse is the distribution for the uncertain task.

REFERENCES

1. Scholz, J, et al. *Exp Brain Res*. 289-306, 1999.
2. Olafsdottir, H, et al. *Neurosci Lett*. 92-96, 2005.
3. Tillman, M, et al. *J Neurophysiol*. 21-32, 2018.

RECUMBENT TRIKE: INFLUENCE OF ANTHROPOMETRIC MEASUREMENTS ON HUMAN POWERED VEHICLE DESIGN

¹Antal K. Petrik and ¹Louis F. Vertosnik IV, ¹Alex C. Vertosnik, ¹Assel Al-Adayleh, ¹Andrew L. Sahlani

¹Cleveland State University, Cleveland, OH, USA

Email: akpetrik@gmail.com

INTRODUCTION

Recumbent bicycles have been around since the turn of the 20th century. These designs offer various rider advantages, including higher speed and comfortability. There are also ergonomic benefits due to a rider's weight being distributed over a larger surface area and more towards the rear drive wheel. Recumbent bikes became famous when biker Francis Faur broke the one-hour speed record in 1934 [1]. The efficiency and added speed appealed to the likes of many, producing many different styles and layouts. One such design is the so-called "tadpole" option, where one wheel is at the back driving the vehicle and two wheels are in the front to steer with. This provides better balance when turning at higher speeds.

The overall goals of this project were to (i) optimize the vehicle's weight and aerodynamics, (ii) reduce the amount of drag developed at higher speeds, and (iii) design a tricycle that could accommodate different anthropometric dimensions.

METHODS

To start, anthropometry of the entire team, of 8, was surveyed to understand which team members would be the best candidates to develop a vehicle around. Anthropometric measurements of the legs, height, arms, and shoulder width were obtained with the use of a tape measure, while weight was found using a digital weight scale.

The leg measurements were broken into two X-seam values based on the full extension of the leg. Each team member positioned themselves on an indoor

Star Trac Pro 6430 HR Recumbent Bike (w/o click-in pedals), found in the CSU gym, based on where the crank reached its extreme position along with their leg at full extension. From there, a tape measure was positioned at the base of the seatback and extended to the sole of the shoe. Moving to the opposing crank, at the second extreme position, a measurement was again taken from the sole of the shoe to the base of the seatback, providing the displacement of the leg based on crank position. From these values, the lengths of both the hip-knee and knee-heal were later on obtained through calculation.

The measurements were then inputted into an excel sheet for analyzation using statistical methods. The main focus of design was not around the fitness level of the team members but instead the anthropometric measurements. To achieve efficiency and an ergonomic design, the team average, standard deviation, and variance of each measured value was taken using excel based formulas.

Following team calculations, each member was split into gender based groups to isolate outliers within the data sets. Since the competition requires both genders to actively compete in each event, and with the team having 6 male members and 2 female members, it was decided that a design specification goal was to find 3 male members within 1 standard deviation of the male average for at least 80% of the anthropometric measurements.

A bell curve was developed for each anthropometric measurement using normal distribution based on the team average and standard deviation. After

observing each bell curve, the final 3 male team member riders were chosen.

Using the newly determined team member riders, (ignoring genders) the shortest and largest rider dimensions were set as design parameters for frame and aerodynamic fairing design. Inputting those parameters into a positional analysis, based around a 175mm crank length, produced the necessary constraints as to which the roll-over protection system (RPS) bar diameter and front fairing position were held to.

RESULTS AND DISCUSSION

Disclaimer: Team member names have been held to anonymity for privacy reasons and instead have been denoted as $T_i \rightarrow i = 1-8$, along with their genders in parenthesis (M /or F) with M = male and F = female.

Table 1: Team anthropometric measurements and statistical analysis.

Team Member	Full Ext. (in)	Displacement (in)	Height (in)	Shoulder Width (in)	Weight (lbs)
T1 (M)	41	28	71	19	210
T2 (M)	41	28	71	19	190
T3 (M)	40	28	70.5	19	184
T4 (M)	42	31	72	21	180
T5 (M)	42	34	74	23	260
T6 (M)	45	34	78.5	21.5	200
T7 (F)	35	24	61.5	17.5	110
T8 (F)	36	25	63	19	177
Average	40.25	29.00	70.19	19.88	188.88
Male Average	41.83	30.50	72.83	20.42	204.00
Female Average	35.50	24.50	62.25	18.25	143.50
STD DEV	3.07	3.50	5.19	1.67	38.88
Male STD DEV	1.72	2.95	3.04	1.69	29.53
Female STD DEV	0.71	0.71	1.06	1.06	47.38

Table 1 provides a detailed result of each team member's anthropometric dimensions along with statistical analysis of the team average & standard deviation, and gender average & standard deviation. It was evident that the male sample was not within 1

standard deviation for 80% of the anthropometric measurement data, but the female sample was.

Figures 1-5 below, depict normal distribution bell curves showing the deviation of team member dimensions, from the average, for each anthropometric measurement. Taking the female members as outliers due to the need for both to be active participants in the competition, it was immediately evident which 3 male members were to be used as riders. Male members T1, T2, and T3 all fell within ± 2 standard deviations from the team average for at least 4 out of 5 anthropometric measurements, where as male members T4, T5, and T6 were only within spec less than 40% of the time.

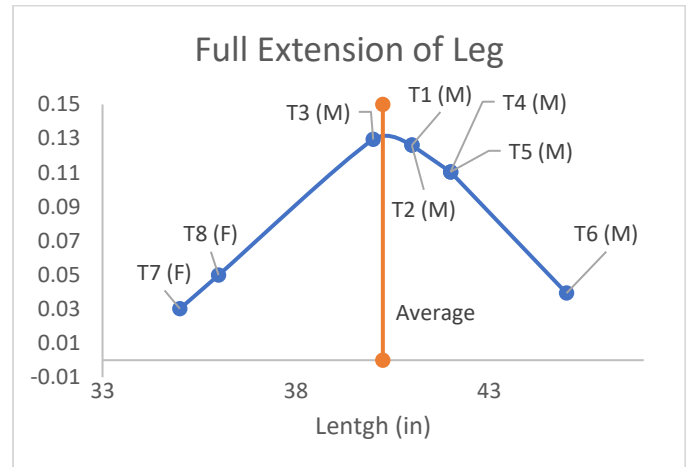


Figure 1: Normal distribution bell curve based on Table 1 calculated statistical results for full extension measurements.

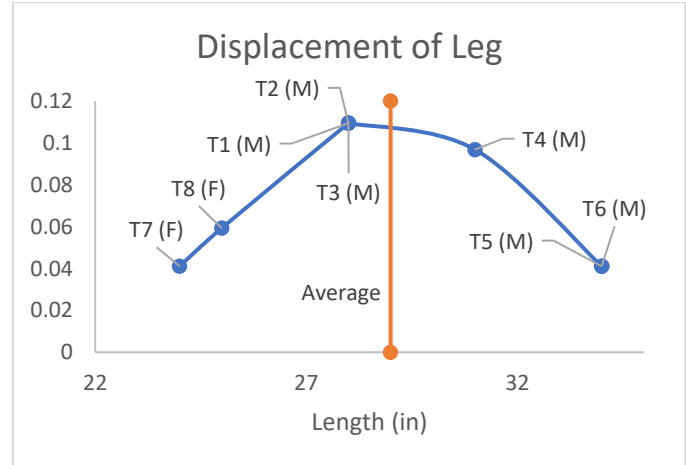


Figure 2: Normal distribution bell curve based on Table 1 calculated statistical results for displacement measurements.

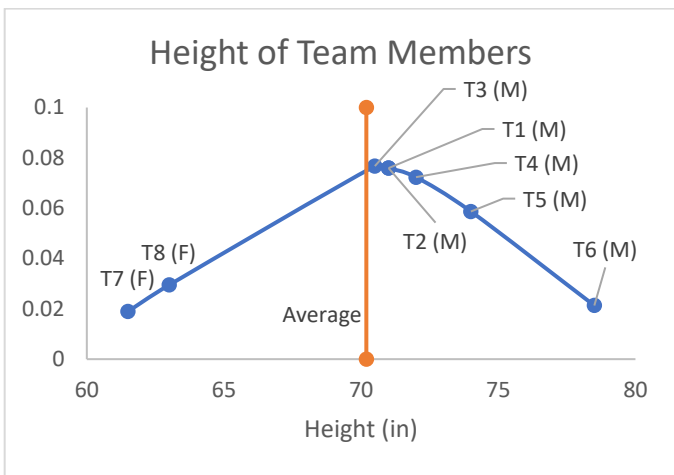


Figure 3: Normal distribution bell curve based on Table 1 calculated statistical results for height measurements.

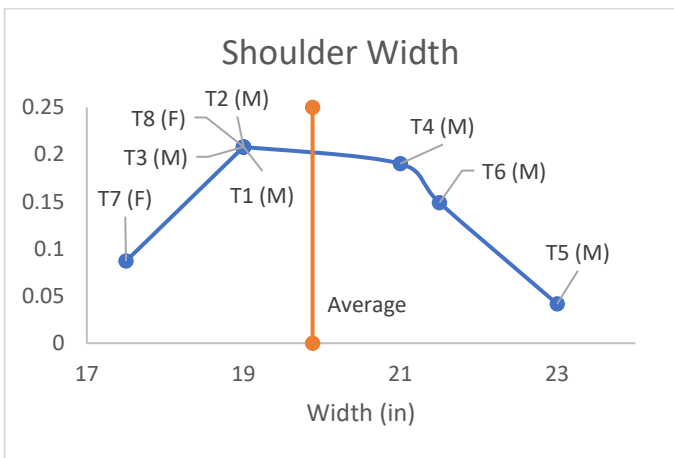


Figure 4: Normal distribution bell curve based on Table 1 calculated statistical results for shoulder width measurements.

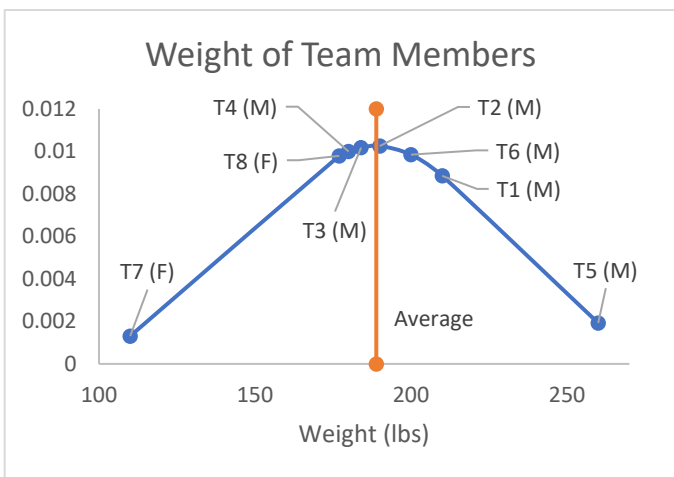


Figure 5: Normal distribution bell curve based on Table 1 calculated statistical results for weight measurements.

With male members T1, T2, and T3 chosen as designated riders, the male standard deviation drastically lowered (found in Table 2). The percent difference between Table 1 and Table 2 values for male standard deviation showed tremendous improvement, helping create tighter design tolerances to which the human powered vehicle could be held to.

Table 2: Adjusted male standard deviation based on riders chosen from analysis of Figures 1-5 along with percent difference from initial male sample calculations.

	Full Ext. (in)	Displacement (in)	Height (in)	Shoulder Width (in)	Weight (lbs)
Male STD DEV	0.58	0.00	0.29	0.00	13.61
% Difference	99.58%	200.00%	165.35%	200.00%	73.78%

Positional analysis of the smallest and largest rider produced desired results allowing the formulation of a design that revolved around an adjustable seat versus the traditional movable crank position. This reduced drivetrain loss due to the reduction of idler pulleys and chain length. Another desired result from the positional analysis was the acquisition of a constant 142° seating angle at which all team riders achieved at least 1" of head room from the top portion of the RPS bar. This seating angle also allowed the front fairing to be positioned lower which in turn reduced the amount of air flow moving under the front wheels.

Figure 6 provides a detailed visual of the smallest and largest rider's leg positions utilizing the measured anthropometric knowns along with the 175mm crank length. Inputting the rest of the predetermined design specifications for the human powered vehicle provided the team with the necessary checks to proceed with frame construction.

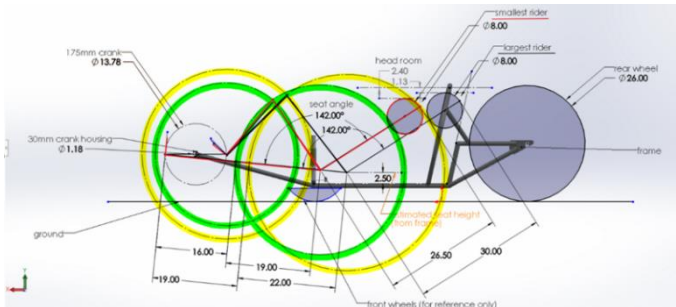


Figure 6: For the largest rider, where the two yellow circles intersect, is the extreme position of the rider's knee when the crank is fully extended away from the vehicle. For the smallest rider, where the two green circles intersect, is the extreme position of the rider's knee when the crank is fully extended. (It is noted that there are 2 extreme positions for both cases, but the inverse position is ignored due to a knee's functionality).

CONCLUSION

When constructing a human powered vehicle, it is absolutely crucial to understand the team's anthropometric measurements. They drastically influence the overall size, shape, and functionality of 90% of vehicle components. In depth analysis on anthropometry leads to efficiency and optimization of major contributing factors in allowing a human powered vehicle to obtain higher speeds and increased handling abilities.

Understanding the extreme positions of rider extremities allows the optimization of tighter design constraints for fairing position, RPS diameter, reduced frontal area, and an overall more aerodynamical vehicle shape. These tighter tolerances allow a vehicle frame to be designed in an ergonomic and efficient manner along with allocating less budget towards frame material expenses, while promoting a reduced curb weight.

Limitations during the design stage are attributed to the accuracy, precision, and calibration of the measurement tools used to acquire the anthropometric measurements. While these limitations can hinder proper vehicle development, they did not skew data drastically as precautions were taken to overcome measurement error, i.e. multiple measurements for each body appendage.

ACKNOWLEDGEMENTS

The Cleveland State University HPVC team would like to thank Dr. Kovach and Dr. Chattopadhyay for their guidance and support throughout the entire design and building process of the vehicle. The team would also like to acknowledge the USS Cod WWII Submarine Memorial and Museum for their donation towards build costs.

An AFM method to obtain nanoscale viscoelastic properties

¹Li Li ¹Steven J. Eppell and ²Fredy R. Zypman,

¹ Case Western Reserve University, Department of Biomedical Engineering, Cleveland, OH
44106

² Yeshiva University, Department of Physics, New York, NY 10033

Email: lxl525@case.edu

INTRODUCTION

We demonstrate a method to acquire nanoscale viscoelastic information from a damped oscillating signal just after the point when an atomic force microscope tip contacts a sample surface. This oscillating signal is below the noise in most single force-displacement measurements. Auto-correlating 20 measurements using the snap-to-contact feature as the reference mark improves the signal/noise ratio allowing making the oscillation clearly visible. The oscillation amplitude is largely insensitive to the speed with which the sample is brought toward the tip consistent with the hypothesis that the signal comes primarily from the impulse generated by the snap-to-contact event. This speed-independence sets a lower limit on how softly a sample may be interrogated when measuring mechanical properties in the surface region. Collection and analysis of this damped oscillating signal eliminates the need for standard low bandwidth lock-in based techniques to determine time dependent surface mechanical properties. This allows conventional atomic force microscopes to make a single pass of force collection over a surface and, after post-processing, yields the full time dependent mechanical behavior of the surface. To demonstrate a practical use of the oscillations, we produce images of a polystyrene/polyethylene sample where the contrast mechanisms are stiffness and viscosity.

METHODS

Atomic force microscope data was collected using a Bruker MultiMode 8 with a Nanoscope V controller operated in peak force quantitative nanomechanics

(QNM) mode in air. The sample studied was a low density polyethylene/polystyrene blend provided by Bruker as a calibration standard for QNM mode. A Bruker ScanAsyst-Air triangle cantilever was used (nominal length 115 um, nominal tip radius 2 nm). The spring constant (1.2 N/m) and first mode resonance frequency (78 kHz) were obtained using the thermal tune method. A 256X256 pixel image of the sample was collected with a peak force set point of 1 nN, a nominal peak force frequency of 1 kHz, and a nominal line scan rate of 0.977 Hz.

While the AFM used has a 50 MHz digitizer, it is difficult to extract data at high bandwidth for extended periods of time using the provided software interface. To overcome this limitation, we interfaced a commercial high speed digitizer (Picoscope 5500) controlled with a custom written Matlab program. The error signal line from Bruker's signal access module was passed through a 1 MHz anti-aliasing filter before being digitized into 15 bit numbers at 62.5 MHz. Collecting all the of the force-distance curves from a single image at this rate and bit depth would have required 32 Gb. We reduced this substantially by sub-sampling the data stream using a square wave trigger from a function generator (Stanford Research System model DS345). The end of line signal from the Nanoscope V controller was used to trigger the function generator which then output a square wave signal at 10 times the line rate of the AFM providing a 10X10 pixel data set. Each square wave triggered the digitizer which was programmed to record 20 peak force cycles of data/trigger. This allowed each pixel to be an

average of 20 force-distance curves collected near the center of the pixel.

RESULTS AND DISCUSSION

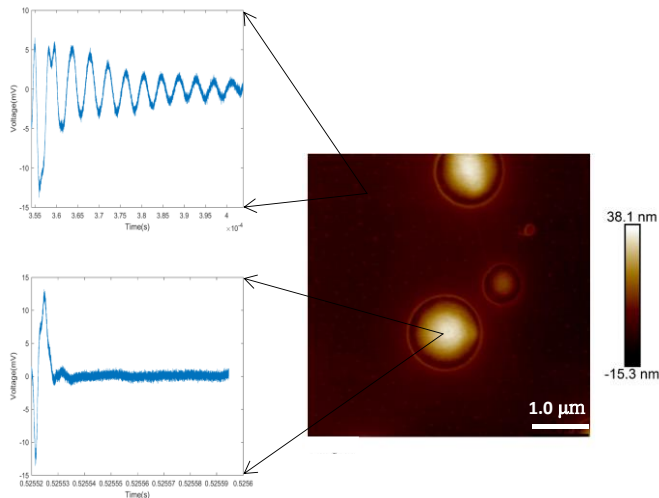


Figure 1 shows a typical topograph of a polystyrene/polyethylene sample taken using peak force tapping mode. The light disc shaped objects are polyethylene. They are typically 0.5-5 μm in diameter and stand proud of the darker polystyrene background by about 20 nm in height. The insets at left are processed force-distance curves showing the difference in response over the two polymer phases. The polyethylene, a soft viscous material, shows stronger damping after impact compared to the polystyrene, a hard-elastic material.

We have introduced a new way to obtain viscoelastic properties of surfaces at the nanoscale. The method has the low shear force advantages inherent in peak force or digital pulse force mode operation; it does not require lock-in detection or the need to digitally assess phase shifts between the cantilever response and cantilever driving signal.

The magnitude of sample response appears to be largely decoupled from the speed with which the tip and surface approach each other under typical operating conditions. Of course, if the tip/sample velocity were to approach the velocity the tip obtains during the snap to contact event (typically around 1

mm/sec), then this assumption would fail. However, this would only increase the impulse delivered to the sample upon impact. Thus, the impulse delivered due to the snap to contact sets a lower bound on how gently the sample can be interrogated when using methods like the one presented here.

The decaying sinusoid seen between contact and peak force has a frequency, amplitude, and damping coefficient set by both the sample properties and the cantilever. Based on first principles, it is expected that a minimum of two coupled oscillators will be necessary to obtain quantitatively accurate measures of surface stiffness and viscosity. However, the single oscillator model used above showed very good fits to the data.

CONCLUSION

By autocorrelating and averaging at least 20 curves, we found a previously hidden decaying oscillation in the separation vs. time curve collected during a typical stroke of peak-force mode imaging. The frequency of this oscillation is not from any expected natural frequency of a beam pinned at both ends. This fact is consistent with the decaying oscillation containing information about the mechanical properties of the sample surface. A single damped harmonic oscillator fits the decaying oscillation well. Since the cantilever mechanical properties remain constant throughout the

experiment, we conclude that contrast in parameters corresponding to the oscillatory and decaying components of the model oscillator are related to the local stiffness and viscosity of the sample respectively. Finally, since the overall amplitude of the oscillation is not a function of the velocity with which the sample is brought toward the tip, we conclude that the decaying oscillation occurs in response to the snap to contact event. This is consistent with stating that the lateral resolution of the mechanical properties obtained using the new method is a maximum with respect to any technique

that does not keep the tip in constant contact with the sample as the surface of interest is scanned.

ACKNOWLEDGEMENT

This work is supported by NSF grant # CHE
1508085

TREATMENT OF STRESS URINARY INCONTINENCE BY M2-POLARIZED MACROPHAGE SEEDED COLLAGEN BIOTEXTILES

^{1,2}Ilaha Isali, ²Phillip McClellan, ¹Eswar Shankar, ¹Sanjay Gupta, ⁴Mukesh Jain, ¹Adonis Hijaz,
^{2,5,6}Ozan Akkus

1. Department of Urology, Case Western Reserve University, Cleveland, OH, USA. 2. Department of Mechanical and Aerospace Engineering, Case Western Reserve University, Cleveland, OH , USA. 4. Harrington Discovery Institute and the Harrington Heart and Vascular Institute, Case Western Reserve University, Cleveland, OH, USA 5. Department of Biomedical Engineering, Case Western Reserve University, Cleveland, OH, USA. 6. Department of Orthopedics, Case Western Reserve University, Cleveland, OH , USA

Email: oxa@case.edu

INTRODUCTION

The immunological response of the body to implanted biomaterials remains the most significant critical issue for the development of tissue engineering. Numerous urogynecological applications necessitate tissue support meshes. These scenarios call for materials that endorse de novo collagen deposition by the body to maintain long-term load bearing capacity. A key regulator of collagen production *in vivo* is pro-regenerative M2 macrophages. By simplified classification, macrophage phenotypes has been divided into 2 groups: M1 (classically activated macrophages) and M2 (alternatively activated macrophages) [1]. The establishment of advanced biomaterials that encourage monocytes to polarize to M2 macrophages may be an effective way to increase surgical outcomes in tissue reinforcing mesh applications. Our past *in vivo* study has shown that M2 polarized macrophages were elevated around genipin crosslinked collagen textiles [2]. Based on those results, we hypothesized that a genipin-crosslinked collagen mesh will promote polarization of M0 macrophages to M2 form *in vitro*. Our aims are: 1) to demonstrate the feasibility of seeding macrophages on genipin-crosslinked mesh for implantation; 2) to illustrate M0 macrophages on said scaffolds undergo a transition to M2 macrophages.

METHODS

Monocytes were harvested from rat bone-marrow and after about 7 days, cells became attached. After 24 h. incubation with LPS and IFN- γ , M0 cells were polarized into M1 cells. For M2 polarization, the M0 cells were incubated with IL-4, -10 and TGF beta1 for 24 h. The macrophage subtypes were identified by using flow cytometry and immunocytochemistry using antibodies against CD68, CD163, CD86, Arginase 1 and iNOS2. Collagen threads were prepared by electrochemical alignment process as described previously [3]. Electrochemically aligned collagen threads were filament wound using a custom computer numeric controlled machine to produce collagen textiles which were then crosslinked by using genipin (Figure 1). Following sterilization, scaffolds were seeded with macrophages and cultured for up to 3 days. Experimental groups included M0 (N=3), M1 (N=3), and M2 (N=3) macrophages. Seeded scaffolds were assessed for cell attachment, proliferation, structure, and protein expression. Western blot analysis was conducted for iNOS and Arginase 1 each of the three groups to determine their phenotype at 72 hours.

RESULTS AND DISCUSSION

Macrophages from all groups exhibited over 70% cell attachment at 4 hours following seeding and cell

proliferation was similar among all 3 groups. With respect to cytoskeletal structure using phalloidin staining, M0 and M2 macrophages demonstrated a significant degree of alignment on the surface of the collagen fibers while alignment of M1 cytoskeletal elements was not as readily apparent. Protein expression highlighted the presence of arginase I and absence of iNOS in M0 cells at 72 hours after seeding on genipin-crosslinked fibers (Figure 2).

Figure 1. Genipin crosslinked scaffolds (scale bar: 10 mm).

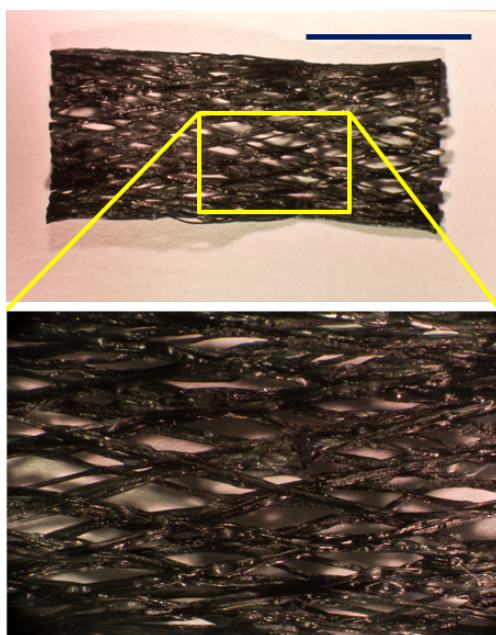
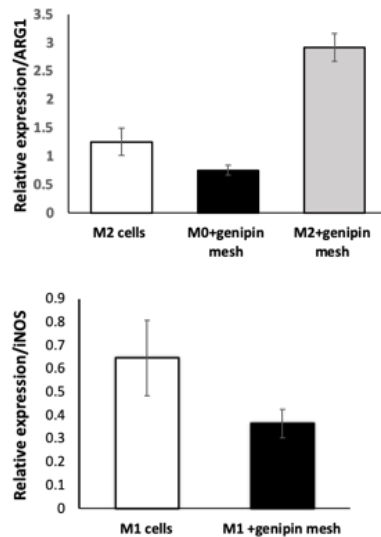
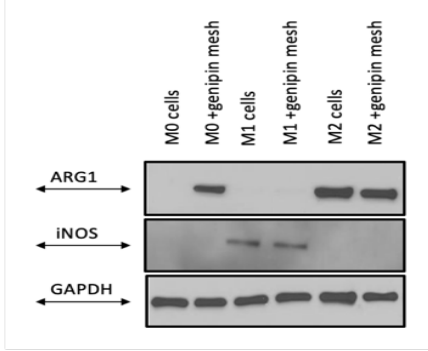


Figure 2. Protein expression analysis of macrophages seeded on genipin crosslinked collagen scaffolds after 72 hrs.



CONCLUSION

Genipin-crosslinked collagen scaffolds support sufficient macrophage attachment and survival for implantation. Protein expression results suggest genipin-crosslinked collagen scaffolds induce polarization of M0 macrophages to the proregenerative M2 phenotype. This is a significant finding implying that genipin crosslinked collagen meshes promote the regenerative capacity by potentiating macrophage polarization.

REFERENCES

1. Mills, C. D, et al. *The Journal of Immunology*, 2000, 6166-73.
2. Chapin K, et al. *J Biomed Mater Res B Appl Biomater*. 2019, 479-489
3. Younesi M, *Adv Funct Mater*, 2014, 5762-5770.

ACKNOWLEDGEMENTS

This work is supported by NIH grant: R21HD095439-02

RADIAL HEAD FOVEAL RADII OF CURVATURE ARE RELATED TO CARTILAGE THICKNESS AND THE SAFE ZONE OF THE HEAD

¹Joseph M Amadio (Presenter), ² Kathryn Smolinski, ²Anne Smolinski, ¹Alexander Kharlamov,
^{1,3} Mark Carl Miller

¹Allegheny General Hospital, Pittsburgh, PA, USA

²University of Wisconsin, Madison, WI, USA

³University of Pittsburgh, Pittsburgh, PA

Email: 22jamadio22@gmail.com

INTRODUCTION

Radial head replacement often follows comminuted fracture with the choice of prosthesis dictated by the head diameter. While replacement is effective in the majority of cases, stem loosening, the articulation of cobalt-chrome on cartilage and infection can lead to revision or excision. The current research was undertaken to examine factors related to the problems of the metal on cartilage articulation. The capitellum of the humerus seats in the foveal depression of the radial head and the interface contact pressures will be directly related to the curvature of the surface. Previous studies have described variations in articular cartilage across the radius but have neither defined the fovea nor measured surface topology.^{[1][2]} In the current work, we sought to quantify the location of the fovea, the radius of curvature of the fovea and the relationship of the foveal curvature to the thickness of the articular cartilage.

METHODS

Eight cadaveric radial heads were procured with institutional board approval. They were separated just below the radial tuberosity and attached to a keyed block that fit into a solid base. The heads were scanned with a NextEngine 3D Laser Scanner. After the initial scan, each radial head was placed in 5% bleach solution, submerging the lateral cartilage border. In the bleach, cartilage was removed to obtain the subchondral surface. Models with and

without cartilage were aligned using the solid base; each model was smoothed and checked for surface integrity.

A plane was fit to the rim of the radial head and an ellipse was fit to each radial head and the average major and minor axes were determined. The location of the average major axis relative to the radial tuberosity was determined.

A 500 x 500 Cartesian grid was overlaid on each radial head and the cartilage thickness and curvature at each grid point was determined. The average thickness and curvature of the eight radial heads was computed using the Cartesian grid. The average ellipse bounding the radial heads was determined and used to locate the grid points.

The fovea was outlined using the inflection points determined by the Gaussian and mean curvature maps; points of zero gaussian curvature and mean curvature sign change indicated an inflection point. The planes fit to the rims were used to place all radial heads in the same coordinate system and the mean major axis of the bounding ellipse of the radial head was used as a reference axis.

RESULTS AND DISCUSSION

The inflection points of the curvature on the surface outlined an elliptical region identifying the average fovea (Figure1). The mean fovea comprised 49% of the average surface area, centered 3.7% radially in the first quadrant at 44° from the major axis of the

radius. The average minimum radii of curvature inside and outside the fovea were 13.8 ± 4.4 mm and -3.01 ± 2.61 mm. The average maximum radius of curvature were 41.8 ± 70.2 mm and 135.2 ± 3662.8 mm, high radii signifying flat surfaces. The average cartilage thickness inside the fovea was 0.885 ± 0.235 mm, outside the fovea the average thickness was 1.415 ± 0.580 mm

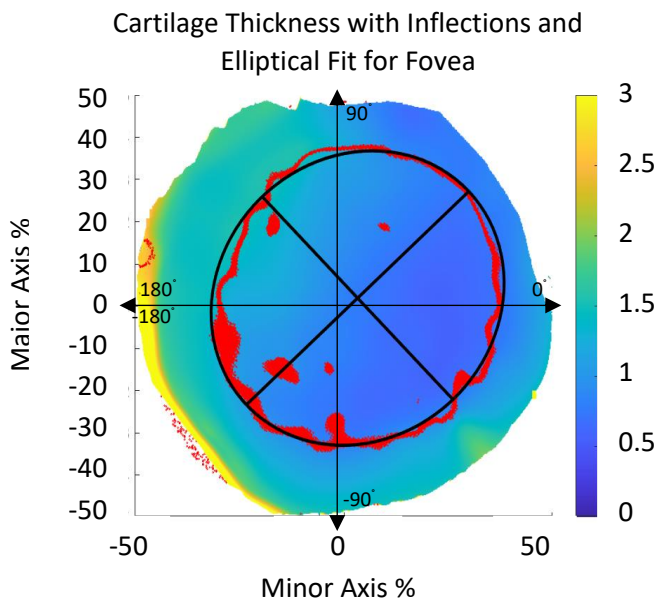


Figure 1: Cartilage thickness map with major and minor axes aligned with the x and y axes. Inflection points and the subsequent foveal fit are superimposed. Angular position is $-180^\circ < \theta < 180^\circ$ with 0° aligned with the right side of the major axis.

Inside the fovea, maximum curvature values (P_{\max}) were normally distributed, however, the minimum curvature values (P_{\min}) were not. The two distributions were significantly dissimilar ($p < 0.001$). Neither P_{\max} or P_{\min} were related to θ and both possessed moderate negative correlation ($\rho_{\text{spearman}} = -0.405$ and $\rho_{\text{pearson}} = -0.516$ respectively) with distance from the foveal center.

Cartilage thickness inside the fovea was not normally distributed and was very weakly correlated with P_{\max} and P_{\min} ($\rho_{\text{spearman}} = -0.129$ and $\rho_{\text{spearman}} = -0.2288$ respectively). Correlation between the distance from the foveal center and thickness was very weakly

positive ($\rho_{\text{spearman}} = 0.1734$). Cartilage thickness along radial lines from the center of the fovea using the major axis as a reference angle clearly agreed with the location of the safe zone of the radial head (Figure 2). The minimum variation in cartilage thickness was located at approximately 55° , which closely aligned with the major axis of the fovea.

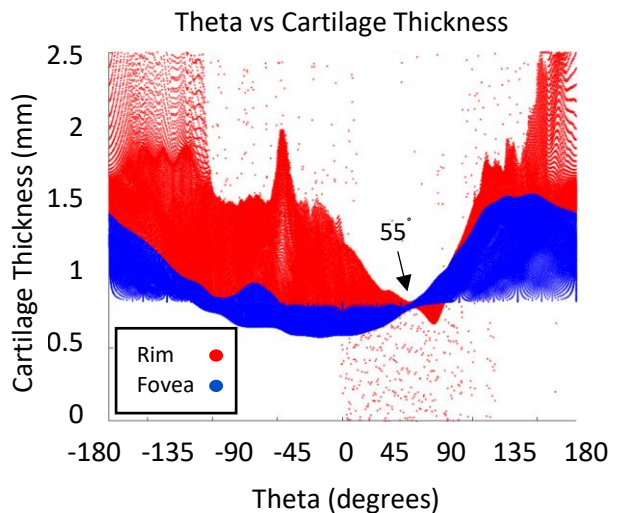


Figure 2: Scatter plot of cartilage thickness inside and outside the fovea in terms of relative polar position. Zero degrees is aligned with the x-axis of the cartilage thickness map (Figure 1).

CONCLUSION

The average foveal radii of curvature of the eight radial heads were 13.8 ± 4.4 mm and 41.8 ± 70.2 mm. The fovea was aligned within 11 degrees of the safe zone of the radial head. Cartilage thickness and surface curvature only weakly covary in the radial direction, while curvature has no relationship with the angular distribution of cartilage but may be oriented with respect to the safe zone.

REFERENCES

1. Yeung, C., *J Hand Surg Am.* 2015; 40(12): 2364-2371.
2. Miyamura, S., *JB JS Open Access* 2019; 4(3): 1-11.

T1 AND T2 WEIGHTED IMAGE PROCESSING OF CHIARI MALFORMATION TYPE I

¹Jiyoon Kim, Maggie Eppelheimer, Francis Loth

¹The University of Akron, Akron, OH, USA

Email: jk215@zips.uakron.edu

INTRODUCTION

Chiari Malformation Type I (CMI) is a disorder that occurs due to the extension of cerebellar tissue into the spinal canal [1]. Chiari patients experience occipital headaches, neck pain, balance problems, and many other diverse symptoms [2]. MRI (Magnetic resonance imaging) is magnetizing the properties of atomic nuclei of the tissue being imaged, and is used to obtain the midsagittal image of the patient. Two types of MR images are mainly used in the study, which are T1 (longitudinal relaxation time) and T2 (transverse relaxation time) weighted images. The main difference between T1 and T2 weighted images is relaxation times and spin density, T1 has an increase in T2 proton density, the TR (Repetition Time) and TE (Time to Echo) is made short, magnifying the effect of longitudinal relaxation and reduce the effect of transverse relaxation for T1 images which is the reason why it can be made quickly. Compare to T1-weighted images, T2 use longer TR with low signal intensity, making CSF (cerebral spinal fluid) a bright intensity, and longer TE, it is more accurate however took long imaging time [3]. All the measurements were completed on a T1- and T2-weighted MR images of a single Chiari patient to have better understanding and more accurate diagnosis of CMI. They are commonly used to assess the brain anatomy, T1-weighted imaging was significantly superior to T2-weighted imaging in assessment of infundibulum ($p < 0.05$) in diagnosis and management of patients after surgery for pituitary tumors [4]. While infundibulum has been shown to be clearer in T1 images, clarity of other brain morphology between T1 and T2 has yet to be assessed. This study is focused on quantifying morphological differences between T1 and T2 images in Chiari patients. The main objective for this study was to visualize the specific difference between T1 and T2 brain MR

images of the CM cases of the same patient and examine if the T1-weighted images are more useful to diagnose the Chiari patients.

METHODS

All morphometric parameters were measures using a *MATLAB* based image processing software (*MorphPro*). It was used to obtain twenty-four measurements (length, angle and area) from the MR images. T1 and T2 weighted images were obtained through the Chiari1000 database, and a commercial DICOM image viewer (*Horos*) was used to obtain the midsagittal images. The criteria zones (McRae line, Tonsillar position, Distance from Fastigium, Pons, Corpus Callosum to McRae line, and the Clivus length) and additional measurements were obtained to be compared. One patient was examined and more cases will be added to the study in future.

RESULTS AND DISCUSSION

Figure 1 shows a representative T1-weighted image, and figure 2 shows a representative T2-weighted image. The percent difference was used to analyze the data. Most of the difference were under 10%, but some were above 10%. Following measurements had percent difference more than 10%: Tonsillar Position (21.5%), Distance from Pons to McRae (11.95%), Basilar impression (55.60%), Basion dens interval (36.72%), Gabbs oakes (10.33%), and Basion to Posterior axialine PAL (18.78%). The most significant percent difference was the Basilar impression with the percentage of 55.6%. The average percent difference was 8.92%.

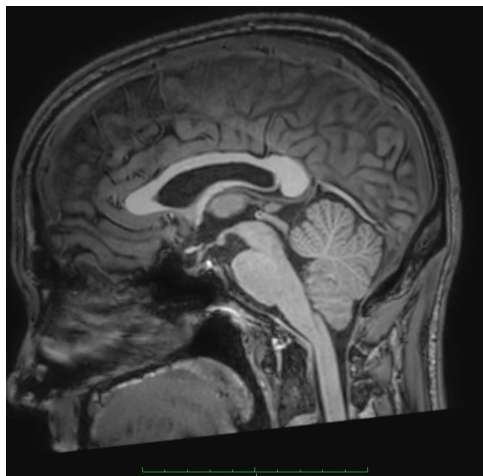


Figure 1: T1 weighted MR image



Figure 2: T2 weighted MR image

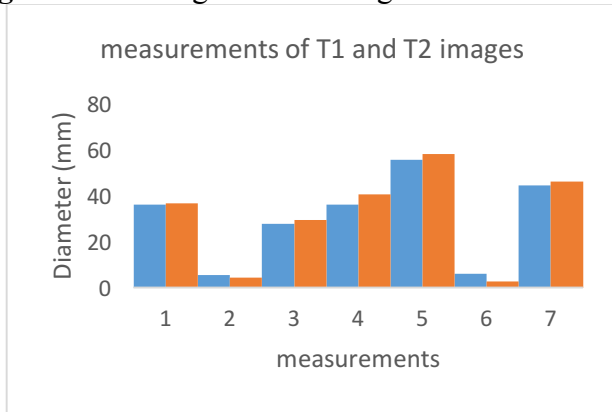


Figure 3: Bar graph with the measurements of

McRae Line (1), Tonsillar Position (2), Distance from Fastigium to McRae (3), from Pons to McRae (4), Corpus Callosum to McRae (5), Basilar impression (6), and the Clivus Length (7) in T1 (Blue) and T2 (Orange), respectively.

CONCLUSIONS

The percent difference of some measurements were suggestive. They were differing by more than 10% percent error. Since T2 weighted images has higher density, the measurements were easier to be recognize. More cases with more morphometric parameters assessing the CSF space differences will be evaluated in the future.

REFERENCES

1. Nash, J et al. *Chiari Type I Malformation: Overview of Diagnosis and Treatment*. Wisconsin Medical Journal. 2002; 101(8): 35-40.
2. Fischbein R, Saling JR, Marty P, Kropp D, Meeker J, Amerine J, et al. *Neurological Sciences*, 36:1617-24, 2015.
al. *Neurological Sciences*, 36:1617-24, 2015.
3. Bladowska J, Biel A, Zimny A, Lubkowska K, Tupikowska G, Sozanski T, Dorobisz U, Sasiadek M, et al. *Medical Science Monitor*, v.17(10); 2011
4. Buxton R, Edelman R, Rosen B, Wismer G, Brady T, et al. *Journal of Computer Assisted Tomography* Raven Press, 15 1987

ACKNOWLEDGEMENTS

I would like to thank all CMI patients for participating in this study and for Conquer Chiari for financial support.

DESIGN OF TPMS FOR TISSUE ENGINEERED SCAFFOLDS USING NTOPOLOGY PLATFORM

¹Andrew Fretwell (Presenter), ²Matthew Shomper, ¹Trenton Classen, ¹Joel Pensworth, and ¹Timothy Norman

¹Cedarville University, Cedarville, OH, USA

²Tangible Solutions, Fairborn, OH, USA

Email: tnorman@cedarville.edu

INTRODUCTION

In the medical industry, there is a growing need for affordable implants that are customized to each patient. Just as each bone defect is unique, so is each patient in need of an implant. Additive manufacturing (AM) allows for the creation of more complex geometries than traditional manufacturing methods and can be used to make customized titanium implants. Triply-periodic minimal surfaces (TPMS) can be created using AM. TPMS structures have continuous smooth surfaces in which the mean curvature of the surface is zero [1]. TPMS have a high ratio of surface area to volume, allowing more room for osteoblasts to adhere to the structure [2]. TPMS are also preferred for biological applications because they have a long fatigue life, are less prone to stress risers and concentrations, and encourage homogeneous cell generation [3].

METHODS

In this study, we created cubic lattices composed of repeating TPMS unit cells to match the strain response rate of natural trabecular bone. TPMS unit cells come in a variety of types. The diamond and gyroid unit cell types are studied here.

Using nTopology Platform (New York, NY), we generated TPMS lattices in the shape of 1cm³ cubes, utilizing both the diamond and gyroid unit cell types. We created nearly 70 lattices, varying the wall thicknesses and the sizes of the repeated TPMS unit cells. The cell size was varied from 1mm³ to 10mm³ in 1mm³ increments, and these 10 designs each had a respective group of models with varying wall thicknesses. When increasing the wall thicknesses for each design, a point was reached where increasing the thickness any more would not be beneficial, as the resulting geometry would resemble a solid cube. This is illustrated in Figure 1.

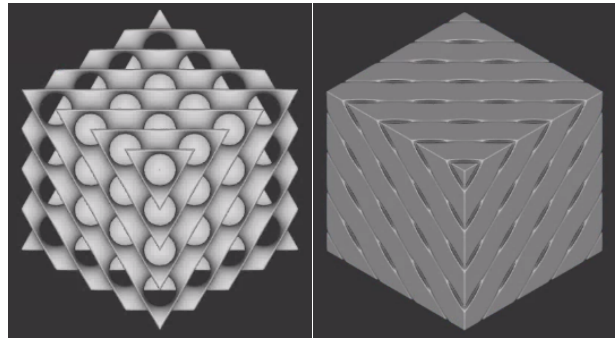


Figure 1. Diamond TPMS lattices with 5 mm unit cell side lengths. 0.25 mm wall thickness (left); 1.75 mm wall thickness (right)

Once we had created the lattices that fell within the range of 1mm-10mm side lengths and with varying thicknesses, we performed finite element analysis (FEA) on the lattices (Figure 2). In order to perform satisfactorily as implants, a target strain range of 1500-3000 $\mu\epsilon$ for the lattices was used [4]. For our analyses we subjected each scaffold to a 1000 N load, a conservative estimate for what is experienced in the human spine during moderate exercise [5].

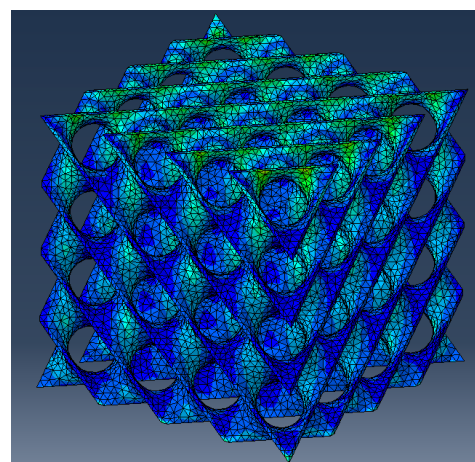


Figure 2. Max principle strain plot on diamond TPMS lattice (5 mm cell size, 0.25 mm wall thickness)

Using our results and the cross-sectional areas of the lattices, we also determined the stiffness of each structure, E_{global} . Due to the nature of TPMS, the cross-sectional area of each lattices is not constant. Because of this, an average cross-sectional area was used when calculating stiffness. 1-D Hooke's Law (Eq. 1) was used for the stiffness calculations.

$$\frac{Load}{A_{avg}} \cdot E_{global} \epsilon_{global} \quad (1)$$

After analyzing our models using FEA, we printed physical lattices in order to verify our results. The physical models were additively manufactured using Ti-6Al-4V and Selective Laser Melting techniques at Tangible Solutions (Fairborn, OH) (Figure 3). Compressive loading was applied to the lattices to determine their stiffnesses, and the average cross-sectional areas were used as with the FE models.



Figure 3. 10 mm diamond TPMS cubes. 5 mm cell size, 0.25 mm thickness (left); 8mm cell size, 0.5 mm thickness (right)

RESULTS AND DISCUSSION

Figure 4 shows an interpolated surface using the resulting strains from a select group of diamond TPMS lattices, containing 25 models that experienced max strains near our desired strain range. Horizontal planes mark the desired strain range for the lattices. For a given cell size or thickness, there is a complementary range of thicknesses or cell sizes that produces a strain value within the desired range.

The two physically tested lattices had similar performances when loaded compressively. Both the 5 mm cell – 0.25 mm thickness specimen and the 8 mm cell – 0.5 mm thickness specimen has stiffnesses of about 11.4 GPa. This value is lower than the values obtained through FEA, as these two

models were predicted to have stiffnesses of about 19 GPa. This discrepancy is under investigation but may be attributed to the general differences between ideal numerical calculations and physical models. While different, both of these stiffness values are very comparable to that of bone.

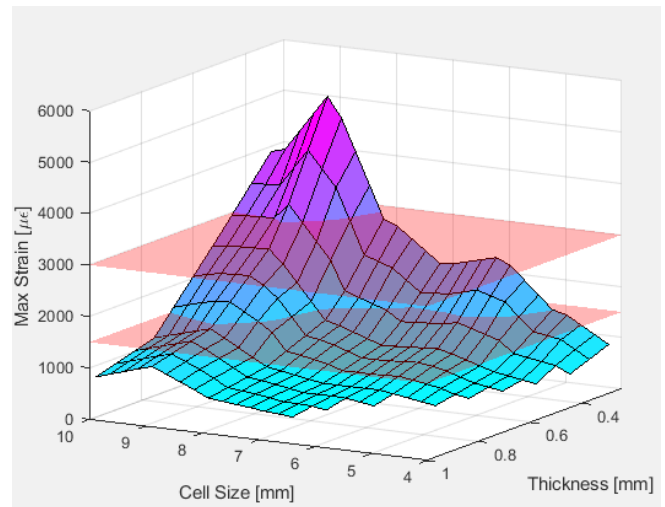


Figure 4. Max principle strain of diamond TPMS finite element lattices subjected to 1000 N load

CONCLUSION

In conclusion, we found that we were able to successfully mimic the strain response rate of trabecular bone with TPMS lattices designed in nTop Platform. These TPMS lattices had high porosity and surface area conducive to cell proliferation. In addition, stiffnesses were comparable to bone which should promote bone remodeling and implant sustainability.

REFERENCES

1. Yan, C. et al. *Journal of the Mechanical Behavior of Biomedical Materials* pp. 61-73 (2015)
2. Vijayaventaraman, S. et al. *ACS Applied Biomaterials* pp. 259-269 (2018)
3. Liu, F. et al. *Materials and Design* pp. 849-860 (2018)
4. Khan, K., et al. *Physical Activity and Bone Health*. Human Kinetics, 2001.
5. Rohlmann, A., et al. *Activities of Everyday Life with High Spinal Loads*. (2014)

ACKNOWLEDGMENTS

The team would like to thank Tangible Solutions for printing our titanium lattices and nTopology for allowing us access to their nTop Platform software.

THE IMPORTANCE OF AN ACCURATE MIDSAGITTAL PLANE IN OBTAINING VALID MORPHOMETRIC MEASUREMENTS

¹Mark Morkos, ¹Natalie Allen, ¹Maggie Eppelheimer, ²Dipankar Biswas, ¹Francis Loth

¹University of Akron, Akron, OH, USA

²University of Central Florida, Orlando, FL, USA

Email: mam585@zips.uakron.edu

INTRODUCTION

Chiari malformation type I (CMI) is a neurological condition, typically characterized by cerebellar tonsils that extend below the foramen magnum at the base of the skull [1]. CMI patients often experience a range of symptoms which could include neck pain, balance problems and numbness. The current process of diagnosis involves evaluating MR images, and morphometric measurements from a reconstructed midsagittal image of the brain. The objective of this study is to determine whether MR images obtained at either left or right of the midsagittal plane of the brain significantly affect morphometric measurements. Particular emphasis was put on the cerebellar tonsillar position in this part of the study. Overall, the study would determine whether MR images that are off the midsagittal plane could be used to obtain valid morphometric measurements that aid in diagnosis of Chiari malformation.

METHODS

Thirty MR midsagittal images were reconstructed using a DICOM medical image viewer called (*Horos*). Each image was processed to obtain a midsagittal slice, and the McRae line, extending from the basion to the opisthion of the foramen magnum, was drawn on each image. The tonsillar position was first evaluated at the midsagittal slice relative to the reference McRae line. Then, slices of the 3-D image were inspected along the coronal plane till the lowest tonsillar position to the right of the midsagittal was found. The tonsillar position on the right plane was evaluated with respect to the

same McRae line drawn on the midsagittal slice. Similarly, the lowest left tonsillar position was also measured for each of the thirty images. The three sets of measurements were statistically analyzed in order to determine whether the difference between either the left or right planes compared with the midsagittal plane were significant. T-tests were performed to compare the average tonsillar position from the right plane to the midsagittal plane, as well as compare the position measurement from the left plane to the midsagittal plane.



Figure 1: Midsagittal plane - The median plane of the head passing through the midline structures

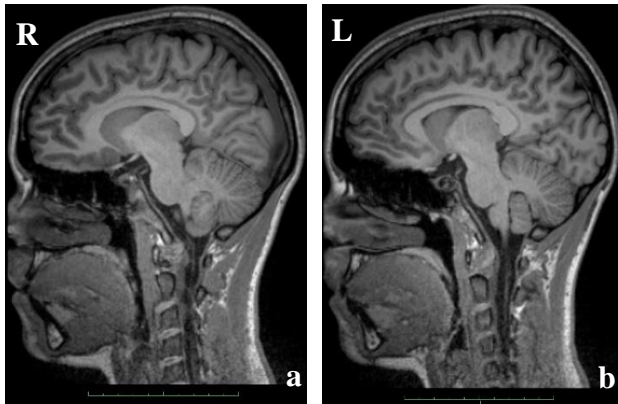


Figure 2: MR sagittal images showing the lowest tonsillar position to the **a)** right and **b)** left of the midsagittal plane.

RESULTS AND DISCUSSION

Statistical analysis involved first calculating the mean values of the three data sets (Figure 3). The mean value for the left tonsillar position was found to be 8.92 ± 4.04 mm, while the mean right tonsillar position was 9.32 ± 4.03 mm and the midsagittal tonsillar mean was 8.82 ± 4.70 mm. The average difference between the left tonsillar position and the midsagittal tonsillar position was found to be 0.10 mm, whereas the average difference between the right tonsillar position and the midsagittal tonsillar position was 0.50 mm. T-tests were performed and concluded that differences between left and central tonsillar positions, and right and central tonsillar positions were not significant ($p > 0.05$)

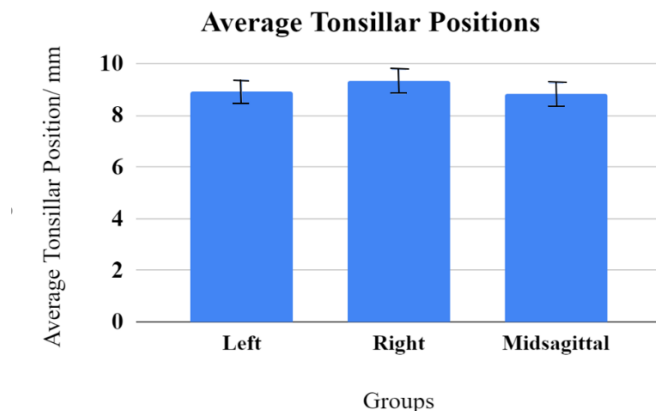


Figure 3: The mean values of the data sets. The whiskers indicate the standard deviation.

CONCLUSION

This study has concluded that it is possible to use MR images that are slightly off midsagittal plane in order to obtain valid tonsillar position measurements that can aid in the diagnosis of Chiari malformation. This is a valuable finding since it is difficult to obtain midsagittal slices for a number of cases, particularly when the number of slices used to reconstruct the 3-D image is limited. Further studies will be undergone to evaluate the effect of the shift from the midsagittal plane on the measurements of other morphological structures, which would further aid the diagnosis of Chiari malformation, as well as other cranial disorders. [2]

REFERENCES

1. Nash, J et al., *Chiari Type I Malformation: Overview of Diagnosis and Treatment*. 2002
2. Houston, J et al., *Morphometric Analysis of Cerebellum in Type I Chiari Malformation*. 2017

ACKNOWLEDGEMENTS

We would like to thank all CMI patients for participating in this study and for Conquer Chiari for financial support.

ANALYTICAL MODEL FOR ATTAINMENT OF SPATIAL COHERENCY TO ENABLE AUXETIC – NONAUXETIC METAMATERIAL COMBINATIONS

^{1,2}Yusuf Dikici, ¹Bo Li and ¹Ozan Akkus

¹Case Western Reserve University, Cleveland, OH, USA

²Bartin University, Bartin, Turkey

Email: ozan.akkus@case.edu

INTRODUCTION

Auxetic metamaterials are engineered materials which exhibit negative Poisson's ratio due to the deformation mechanism of unit geometry. Analytical models of auxetics allow to design new geometries and the tunability in Poisson's ratio as well as Young's modulus. This unique advantage enables the use of auxetics in many engineering fields, including bioengineering. Some examples in the field of biomechanics are hip implant stem design, bone screws and so on.^{3,5}

A few studies on auxetics present hybrid structures which are created in order to combine mechanical advantages of auxetic and non-auxetic structures in the same pattern, such as obtainment of materials with zero Poisson's ratio⁴ and those studies mostly focuses on re-entrant – honeycomb combinations. However, hybridization of different material structures as such has been limited, mainly because stacking of these nodal structures is not straightforward.

In this study, we investigate mechanical behavior of a novel 2D metamaterial concept, which is serially stacked auxetic – non-auxetic combinations. Anti-tetrachiral (ATC) model has been preferred as auxetic part and a non-auxetic pattern which is compatible for combining with chiral patterns has been designed by inspiring from conventional honeycomb. As a result of this study, we are presenting an analytical design protocol to determine unit dimensions for exact opposite Poisson's ratio and equal Young's modulus in auxetics and non-

auxetics under the constraint of equal node spacing in the same axis.

MATERIALS AND METHODS

In previous studies, re-entrant auxetic structures are indicated as a derivation on honeycomb structures. Contrary to re-entrant, chiral structures which consist of nodes and ligaments do not have any relatable non-auxetic structure. As a result of this need we designed a honeycomb-inspired chiral structure (HC) for which the same mathematical equations of conventional honeycomb structures may be used.

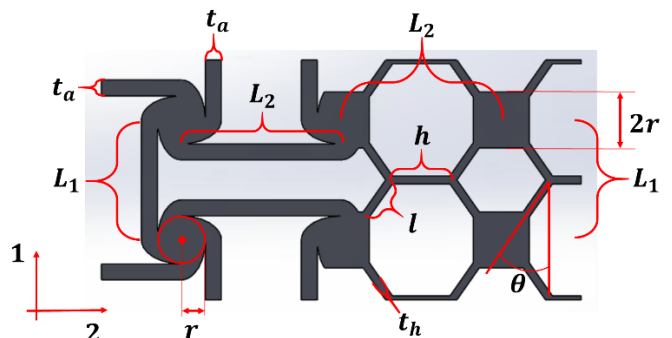


Figure 1: Intersection of metacombination geometry and geometrical parameters

Equal node spacing is the first condition we desire. The reason for this is to make the geometrical parameters relatable:

$$L_1 = 2l\cos\theta + 2r ; \quad L_2 = h + 2l\sin\theta + 2r$$

For the case of serial stacking meta-combination requires a constant Poisson's ratio. The purpose behind this is to provide exact opposite transverse deformation in auxetic and non-auxetic under longitudinal loading. Since exact negative

deformation depends on the same amount of loading, Young's modulus in every cross-section of the structure has to be equal as well so that the deformation applied can be distributed to auxetic and non-auxetic parts equally.

Upon these considerations, previously reported mathematical models of honeycomb¹ and ATC² structures have been utilized with relatable geometrical parameters (eq. 1). Independent variables, θ and h/l are correlated to the condition of equal Poisson's ratio (eq. 3). Substitution of corresponding geometrical parameters into the Young's modulus formulas enables to determine the required ligament thickness of ATC pattern which is a fundamental parameter for stiffness.

$$v_{21}^A = -\frac{L_2}{L_1} = \frac{h/l + 2r/l + 2\sin\theta}{2r/l + 2\cos\theta}; v_{21}^H = \frac{(h/l) + \sin\theta}{\cos^2\theta} \quad (\text{eq. 1})$$

$$-v_{21}^A = v_{21}^H \rightarrow (h/l) = f(\theta) \quad (\text{eq. 2})$$

$$E_2^A = \frac{E_s t_A^3}{3(2r + t_A)^2} \left(\frac{L_1 + L_2}{L_1^2} \right) = \frac{E_s t_A^3}{3(2r + t_A)^2} \left(\frac{h/l + 4r/l + 2\sin\theta + 2\cos\theta}{l * (2r/l + 2\cos\theta)^2} \right)$$

$$E_2^H = \frac{E_s t_h^3 [(h/l) + \sin\theta]}{l^3 \cos^3\theta} \quad (\text{eq. 3})$$

RESULTS

The result demonstrates that the data generated by analytical model is valid between the θ values of 20.7° and 45° for equal Poisson's ratio and Young's modulus in ATC and HC structures. The data that is sourcing from outside of this interval is found practically incompatible for designs.

The results also illustrate that h/l and t_a decreases to maintain the equality of v_{21} and E_2 as increasing θ values.

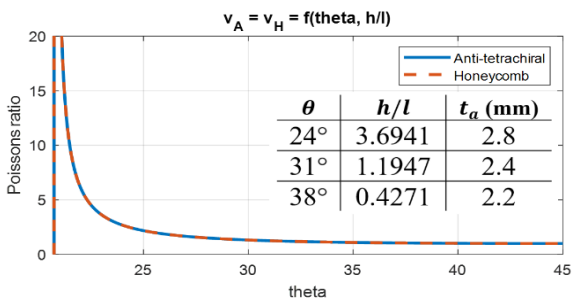


Figure 2: Variation of Poisson's ratio with θ and corresponding h/l ($r = 3 \text{ mm}$, $l = 7 \text{ mm}$, $t_h = 1 \text{ mm}$).

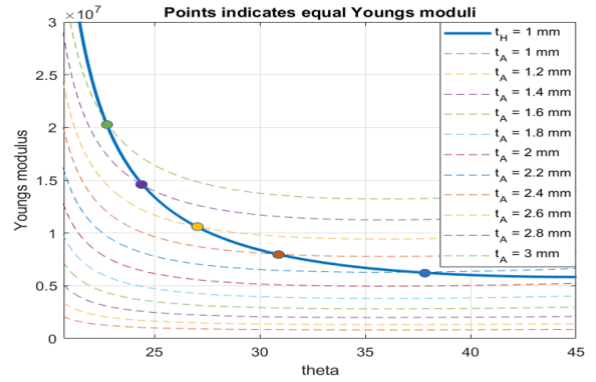


Figure 3: Young's modulus distributions with θ and corresponding h/l for different ligament thicknesses in ATC ($r = 3 \text{ mm}$, $l = 7 \text{ mm}$, $t_h = 1 \text{ mm}$).

DISCUSSION AND CONCLUSION

The main objective of this study is to provide appropriate dimensions of unit structures in order to have relatable mechanical properties between two different meta-structures. This protocol may also be applied for different auxetic – non-auxetic couples and different correlations of v_{21} and E_2 such as $-v_{21}^A = 2v_{21}^H$, $3E_2^A = E_2^H$. Moreover, the findings are directly usable for the purpose of designing 2D and tubular parts exhibiting unique deformation under uniaxial loading.

This research is to be continued with finite element analysis, additive manufacturing and mechanical testing of structures that are predicted by this model.

REFERENCES

1. Gibson, L, et al. *The Mechanics of Two-Dimensional Cellular Materials*. 25-42, 1982.
2. Gatt, R, et al. *A realistic generic model for anti-tetrachiral systems*. 2012–2019, 2013.
3. Kolken, H, et al. *Rationally designed meta-implants: a combination of auxetic and conventional meta-biomaterials*. 28-35, 2018.
4. Olympio, K, et al. *Zero Poisson's Ratio Cellular Honeycombs for Flex Skins Undergoing One-Dimensional Morphing*. 1737-1753, 2010.
5. Yao, Y. et al. *A novel auxetic structure based bone screw design: Tensile mechanical characterization and pullout fixation strength evaluation*. 188, 2019.

EXAMINING RELATIONSHIPS BETWEEN POSTURAL STABILITY AND COGNITIVE TASK DIFFICULTY VIA WAVELET TRANSFORMS: A NONLINEAR DYNAMICS APPROACH

¹Brittany N. Sommers, ²Douglas A. Wajda, ¹Brian L. Davis

¹Cleveland State University, Department of Mechanical Engineering, Cleveland, OH, USA

²Cleveland State University, Department of Health and Human Performance, Cleveland, OH USA

Email: b.n.sommers@vikes.csuohio.edu

INTRODUCTION

Multiple sclerosis (MS) affects more than 2.3 million people worldwide, nearly 1 million in the United States (US) alone [1]. A few of the many symptoms of MS include muscle weakness, poor cognition, and decreased alertness, all of which impact the ability to maintain upright stance.

The purpose of this study is to examine postural stability mechanisms of MS compared to healthy controls as the difficulty of the task increases cognitively. Previous work examined the cognitive effects of these tasks [2], but not the dynamic stability effects.

Stability mechanisms were examined through the Hurst exponent (H), a statistical parameter defining long-term correlations in any moving system. H is defined over a range of $0 \leq H \leq 1$, where $H < 0.5$ indicates stability and $H > 0.5$ indicates instability [3]. H values were calculated with wavelet analyses. Wavelets were used for their ability to characterize non-stationary signals and provide time-frequency localization of a signal [3,4].

METHODS

The four conditions performed were: (1) quiet eyes-open standing (EO), (2) quiet eyes-closed standing (EC), (3) audio perturbed standing with participants leaning to their limits of stability (PRT-LOS), and (4) audio perturbed standing with participants in a comfortable stance (PRT-STA).

In the EO and EC conditions, participants were instructed to stand comfortably for 30-s while performing each task. In the PRT conditions, 20

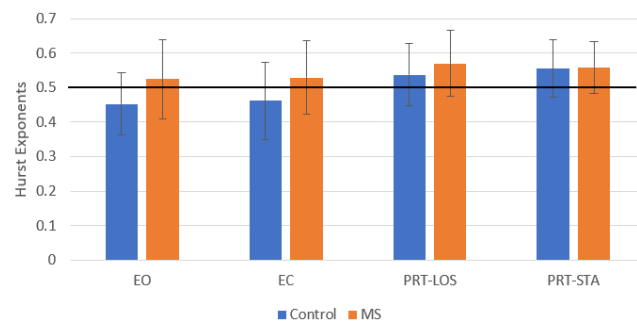
auditory cues (beeps) were given during each task. Participants were asked to respond as quickly as possible to the noise by saying “pop” out loud. They were instructed to maintain their balance on both tasks as well. Ages for controls ($n=33$) and MS ($n=16$) were 62.6 ± 9.1 years and 55.3 ± 11.1 years, respectively.

Center-of-pressure trajectories in the anterior-posterior (AP) direction were analyzed by a level 12, Symlet 2 wavelet decomposition. To obtain H , log-log plots of the average wavelet coefficients at each decomposition level versus 2^j (j = number of levels) were plotted [3,4]. H values are then calculated as $H = \text{slope} - \frac{1}{2}$ [3,4]. Average H values were calculated for both groups.

RESULTS AND DISCUSSION

In the AP direction, control $H_{PRT-LOS}$ values were significantly higher than H_{EO} and H_{EC} . Similarly, control $H_{PRT-STA}$ values were significantly higher than H_{EO} and H_{EC} . (Fig.1)

Fig 1: Control and MS Anterior-Posterior Hurst Exponents



MS did not display significant differences in the AP-directions between conditions. MS were

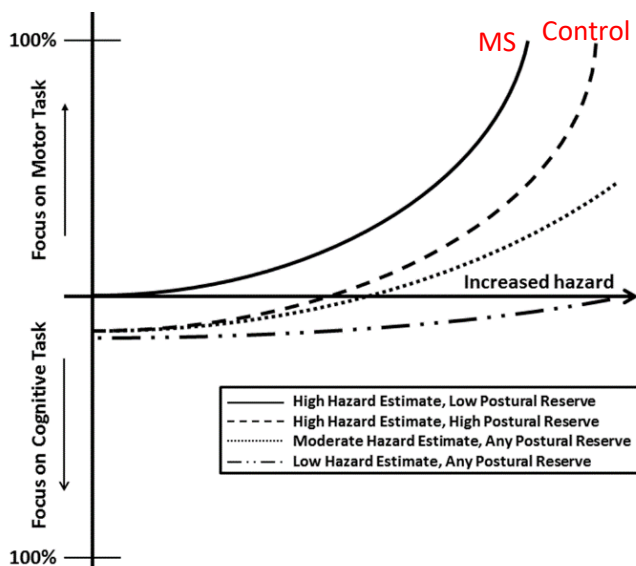
significantly less stable than controls in both the EO and EC condition.

MS displayed instability on all four conditions ($H>0.5$), whereas controls displayed stability ($H<0.5$) for EO and EC, but instability ($H>0.5$) for PRT-LOS and PRT-STA.

Interestingly, controls became less stable on the PRT-STA task than the PRT-LOS task, even though the task difficulty decreased from a stability standpoint. MS became more stable on the PRT-STA task than the PRT-LOS task.

One explanation for this is that controls are considered “High Hazard Estimate, High Postural Reserve” meaning they are cognitively sound, and have better control over their motor output [5]. MS are considered “High Hazard Estimate, Low Postural Reserve” meaning that they were also cognitively sound but have poor control over their motor output [5].

Fig 2. Effects of hazard estimation and postural reserve on focus on cognitive task vs. motor task [5]



Thus, when asked to stand comfortably and respond to the sound, controls most-likely spent more time focusing on the cognitive task than their motor control, as they were confident in their ability to maintain upright stance. As a consequence, their

balance suffered. MS participants on the other hand had to focus more on maintaining postural control, and spent less time focusing on the cognitive task as a way to maintain their balance.

CONCLUSION

Using wavelets to obtain Hurst exponents allows for the analysis of non-stationary time-series data. Controls became significantly less stable as cognitive tasks were introduced. MS participants were unstable even without cognitive involvement and became even more unstable with it. The way these different cohorts respond to cognitive tasks could be due to their amount of hazard estimate versus postural control. Although there were discrepancies between number of participants in each group, the results are logical with the group with a neurological disorder presenting less stability, and the amount of stability decreasing in both cohorts as cognitive challenges were introduced.

REFERENCES

1. National Multiple Sclerosis Society.
2. Wajda D et al. (2019). Journal of Neural Transmission.
3. Simonsen I et al. (1998). Physical Review 58.
4. Schaefer A et al. (2014). Journal of Neuroscience Methods 222, 118-130.
5. Yogev-Seligmann G et al. (2012). Movement Disorders. 27(6).

ACKNOWLEDGEMENTS

Acknowledgements are given to Dr. Doug Wajda for providing the data used in this study.

Volumetric Quantification of Fatty Infiltration in Rotator Cuff Repair Using Semi-Automated Intensity Histogram Analysis

¹Phillip McClellan, ²Lekha Y. Kesavan, ³Jason Ina, ¹Greg D. Learn, ³Robert J. Gillespie,
²Victoria Webster-Wood, and ^{1,3}Ozan Akkus

¹Case Western Reserve University, Cleveland, OH, USA

²Carnegie Mellon University, Pittsburgh, PA, USA

³University Hospitals, Cleveland, OH, USA

Email: pjm357@case.edu

INTRODUCTION

Injuries to the rotator cuff tendon often require surgical intervention. Recurrent failures remain common for tears or ruptures to the tendon classified as large or massive [1]. One potential predictor of success in tendon repair strategies is the quantity of fatty infiltration and muscle degeneration surrounding the affected tendon. Current methods of assessing fatty infiltration exist (i.e. Goutallier classification) but typically rely on subjective assessment and scoring by experienced individuals. However, such methods are difficult to repeat and result in significant inter-observer variability [2,3]. In this study, consistent assessments of fatty infiltration were obtained by using microCT imaging in combination with anatomic landmarks and semi-automated volumetric histogram analyses. Functional outcomes were correlated to fatty infiltration measurements as a potential means of predicting successful surgical outcomes.

METHODS

New Zealand White (NZW) rabbits underwent surgical recreation of a critical defect to the right infraspinatus tendon. The tendon was either repaired immediately (direct repair n=7) or a 5 mm segment was removed from the distal end, leaving the tendon unrepaired (gap n=6). Six months after repair, rabbits were euthanized and left and right scapulohumeral complexes were isolated for microCT imaging. Resulting DICOM files were rescaled based on two known materials, air and carbon fiber, before a cylindrical volume of interest

based on anatomical landmarks was determined. Histograms of volumetric pixel intensities were then generated and assessed for mean, standard deviation, skew, and kurtosis. A specimen composed of adipose tissue in place of the infraspinatus tendon on a rabbit scapula was also scanned to provide a control for determining percent fat by volume. Specimens then underwent biomechanical testing to determine maximum load to failure and stiffness under monotonic conditions or were fixed in formalin and processed for histology. Statistical significance was determined with Mann-Whitney tests ($p \leq 0.05$).

RESULTS AND DISCUSSION

Values of the mean, standard deviation (stdev), skewness (skew), and kurtosis from the volumetric pixel intensity histograms were collected (Fig. 1).

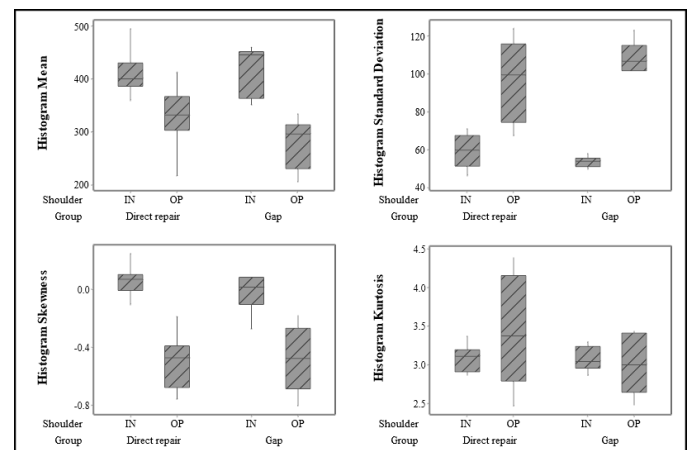


Figure 1: Mean, standard deviation, skewness, and kurtosis for volumetric pixel intensity histograms.

Each set of values from the histogram analyses were assessed to determine to values of fatty infiltration. No significant differences were noted between either group for the intact (IN) or operative (OP) specimens. Differences in mean, stdev, and skew were noted when OP specimens were compared to IN specimens in each group. Percent fat by volume was also compared between groups (Fig. 2).

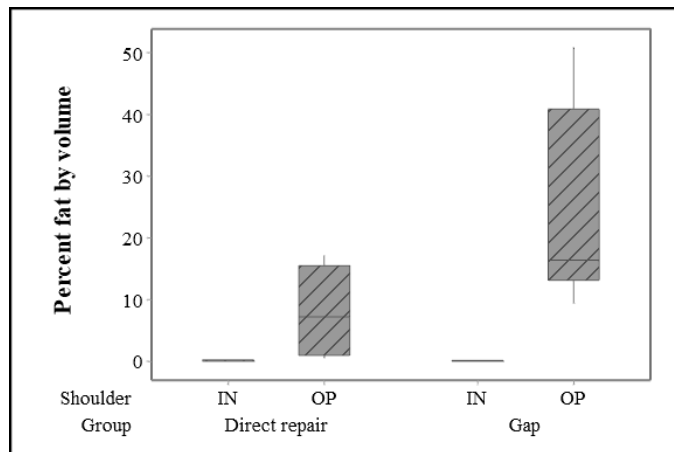


Figure 2: Percent of fat by volume in rabbit infraspinatus tendon and muscle.

In both groups, OP shoulders exhibited significantly more fat tissue within muscle and tendon as compared to IN shoulders. Multivariate regression revealed that calculated percent fat in the volume of interest is best modeled by a combination of mean and stdev in the following equation:

$$\%Fat = 61.24 - 0.1846 * (Mean) + 0.1911 * (STD)$$

Biomechanical testing results highlighted that max load and normalized max load were significantly correlated to percent fat. Stiffness measurements were not found to correlate as strongly with percent fat measurements. After conducting Pearson correlation analysis, models for normalized maximum load with single variate regressions resulted in the highest R^2 values when $p < 0.05$. Equations for regressions were as follows:

$$Norm. Max Load = 0.8872 - 0.09898 * (\%Fat)$$

$$Norm. Max Load = 1.422 - 0.00879 * (STD)$$

Histological examination of the infraspinatus tendons and muscles confirmed the presence of significant adipose tissue primarily within the muscle belly (Fig. 3).

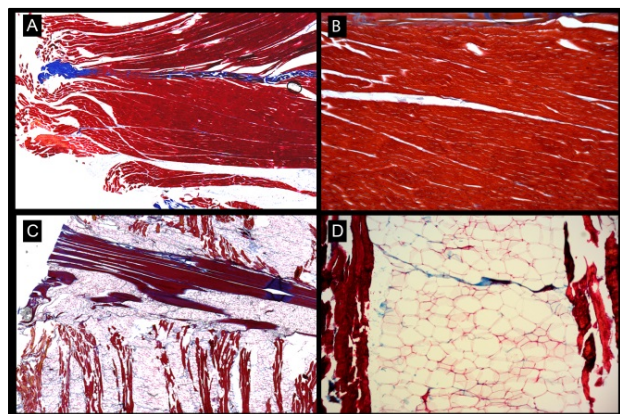


Figure 3: Masson's trichrome staining of IN (A and B) and OP (C and D) shoulders.

CONCLUSION

These results highlight a link between fatty infiltration and biomechanical properties in rotator cuff repair. Understanding the underlying biological mechanisms of fatty infiltration could be critical to improving long-term functional outcomes in rotator cuff repair procedures. A consistent method of assessing fatty infiltration, such as the one presented here, will assist researchers and clinicians.

REFERENCES

1. McElvany, MD, et al., *Am J Sports Med* 43:491–500, 2015.
2. Melis, B, et al., *Orth Traumatol Surg Res* 95:319–324, 2009.
3. Spencer, EE, et al., *Am J Sports Med*, 36:99–103, 2007.

ACKNOWLEDGEMENTS

This study was supported by grants from National Institutes of Health (NIH): R01 AR063701 and T32 AR007505.

INTENSITY OF BALANCE CHALLENGE DURING VIDEOGAMING

Amanda Laxganger, Debbie Espy, and Ann Reinald

Cleveland State University, Cleveland, OH, USA

Email: a.m.lowe9@vikes.csuohio.edu

INTRODUCTION

Poor balance and falls remain a large concern for older adults and individuals with physical disability. Clinicians use adapted commercial video gaming as one intervention technique to address balance impairments. However, a lack of standardized balance intensity measures poses a significant challenge in prescribing appropriate dosage for balance rehabilitation interventions such as gaming [1]. Movement kinematics provide one method for quantifying functional demands of a therapeutic intervention. This study's objective was to use kinematics to investigate how varied balance training game demands and gaming surface increase the intensity of balance challenge, specifically movement of the center of mass (COM) relative to base of support (BOS).

METHODS

Twenty-seven self-reported community ambulators, ages 50-79, played four randomly selected video-gaming conditions. Each condition consisted of a specific game (Microsoft Kinect) and play surface combination. Game conditions were grouped into those requiring kicking (4 conditions), stepping (5 conditions), or no stepping (6 conditions). Participants played about five minutes per condition. They rated their self-perceived balance challenge of each condition using the visual Rate of Perceived Stability (RPS) Scale [2]. Three-dimensional motion capture was collected using the Helen Hayes marker set, an eight-camera system and Cortex software (Motion Analysis Corp., Rohnert Park, CA). Capture data were processed through Cortex and custom

MATLAB code to determine the fraction of game play time that the COM moved outside of the BOS (FX) as well as the maximum excursion range of the COM (EX). Descriptive statistics were calculated for these measures in each condition.

RESULTS AND DISCUSSION

Tables 1-3 display the mean and ranges for RPS scores (maximum challenge 10 on 1 to 10 scale), the fraction of time the COM was outside of the BOS (FX: %), and the maximum excursion of the COM (EX: mm).

Table 1: Data for Kicking Games

Condition description	n	RPS mean	RPS range	Frac. BOS mean	Frac. BOS range	max excursion Mean*	max excursion Range*
Intermediate Target Kick on Mats/Rafts	18	3.61	1-7	0.32	0.10 - 0.56	44.0	5-273
Hard Target Kick on floor	4	3.25	2-5	0.18	0.04 - 0.34	16.7	4-29
Hard Target Kick on rocker	13	4.31	2-7	0.14	0.03 - 0.34	18.5	3-90
Hard Target Kick on slider	16	5.31	4-8	0.15	0.06 - 0.37	7.2	2-33

Table 2: Data for Stepping Games

Condition description	n	RPS mean	RPS range	Frac. BOS mean	Frac. BOS range	max excursion Mean*	max excursion Range*
Ship shapes on Floor	7	1.29	1 - 2	0.06	0.02 - 0.13	179.2	7 - 536
Cruiser Reflex Ridge on Floor	8	1.63	1 - 3	0.05	0.01 - 0.12	56.4	6 - 318
Dodger Reflex Ridge on Floor	3	2.33	2 - 3	0.10	0.02 - 0.14	14.8	6 - 25
Crab Crazy & Fish Frenzy on Floor	11	1.82	1 - 3	0.13	0.03 - 0.35	94.0	7 - 360
Cruiser Reflex Ridge on Mats/Rafts	5	3.20	2 - 5	0.11	0.06 - 0.20	83.9	9 - 369

Table 3: Data for Non-Stepping Games

Condition description	n	RPS mean	RPS range	Frac. BOS mean	Frac. BOS range	max excursion Mean*	max excursion Range*
Amateur Table Tennis on Floor	8	1.50	1 - 2	0.03	0.00 - 0.10	29	2 - 113
Amateur Table Tennis on Mats/Rafts	8	2.13	1 - 4	0.08	0.00 - 0.38	11	1 - 20
Hard Table Tennis on Rocker	7	2.43	1 - 4	0.13	0.00 - 0.65	4	0 - 10
Funnel Cake Falls on Rocker	8	4.25	2 - 7	0.10	0.00 - 0.41	6	1 - 10
Amateur Table Tennis on Slider	7	2.71	1 - 4	0.00	0.00 - 0.00	1	1 - 4
Funnel Cake Falls on Slider	7	1.71	1 - 3	0.01	0.00 - 0.05	1	1 - 1

During the kicking games (Table 1), EX and FX increased on the mat while decreasing on the slider and rocker surfaces. EX especially decreased on the slider while having the highest RPS score. Since there were three conditions using the same game (Hard Target Kick) with three different surfaces, RPS scores ranked these surfaces from easiest to hardest as floor, rocker, and slider, respectively. During stepping games, FX was highest on the mats and the two harder floor games, while RPS and EX increased on the mat surface in the one game played on both floor and mats (Cruiser Reflex Ridge). In the non-stepping games, EX was highest on the floor/mat surfaces and lowest on the slider. FX was lowest in the slider and highest on the rocker surface while RPS was highest on the rocker.

CONCLUSION

Overall, FX and EX were highest in the stepping games, where the games demanded more movement, and lowest in the non-stepping games where the games demanded stability. They also decreased on the two mobile surfaces, especially on the slider. Thus, kinematic analysis of balance intensity in terms of EX and FX must be coupled with an understanding of the game condition.

REFERENCES

1. Farlie M, et al. Intensity of challenge to the balance system is not reported in the prescription of balance exercises in randomised trials: a systematic review. *Journal of Physiotherapy*, 59(4), 227–235, 2013.
2. Espy D. Intensity of balance task intensity, as measured by the rate of perceived stability, is independent of physical exertion as measured by heart rate. *J Nov Physiother*, 7(343), 2, 2017.

ACKNOWLEDGEMENTS

We acknowledge support from the Cleveland State University Undergraduate Summer Research Award as well as the assistance of Lorenzo Bianco, Summer Gaglione, Kathryn Kroszkewicz, and Emily Meisterheim in data collection and analysis.

Measuring Molecular Level Collagen Damage After Uniaxial Tension Test Of Single Collagen Fibrils.

¹Christopher Slater and ¹Steven Eppell

¹Case Western Reserve University, Cleveland, OH, USA

Email: [cas291@case.edu](mailto:cav291@case.edu)

INTRODUCTION

In the United States it is estimated that over 16 million people experience injury to tendons or ligaments each year [1]. Healing from a tendon injury is a process that takes many months and can have a significant impact on quality of life and ability to work. Even with this, our current treatments often do not lead to a full recovery [2]. Presently, finding new and better options for treating tendon injuries (tendinopathies) is limited by our basic understanding of the tendon tissue [2].

We aim to not only improve the basic understanding of tendon tissue but also provide a method of detecting tendon damage before it becomes symptomatic. This is be done using a fluorescently labeled collagen hybridizing protein (CHP), that is able to bind to unwound collagen molecules. In this work, we show that the level of CHP that binds to a single collagen fibril is able to be measured using a fluorescent microscope. We are able to see that as modulus and final stress of a single collagen fibril, increase, so does the amount of CHP binding. We do not see this relationship with final strain of the collagen fibril. We propose that this is due to differences in crosslink density of the collagen fibrils, but more work is needed to prove this. This work aids in both the understanding of how we can detect tendon damage at the single collagen fibril level and aids in our understanding of tendon tissue.

METHODS

First, single collagen fibrils are isolated from rat tail tendons [3]. Using micromanipulators, single

collagen fibrils are placed on a microelectromechanical system (MEMS) and epoxied down for testing. We stained the fibrils with CHP in order to determine the control level of CHP binding. We then attempted to strain seven fibrils to 25% final strain but due to slack in the fibrils the true final strain was lower. Variation in the amount of slack caused varied in amount of final strain for the fibrils.

We then took a second CHP staining in order to see how much more CHP binding took place. We quantified the relative fluorescent increase (RFI) from before strain and after strain using a control (undamaged) region and an experimental (damaged) region in each fibril. This allows us to account for any variations that might affect the fluorescent images, such as photobleaching. The RFI measures how much brighter the strained region is after straining. This corresponds to the amount of unwound fibrils and molecular level damage.

We then ran a Spearman's Correlation Test on RFI value, final stress, final strain and modulus for the fibrils.

RESULTS AND DISCUSSION

We found that every fibril increased its fluorescent intensity after straining. We found a positive monotonic relationship between modulus and RFI ($\rho = +1$, $p\text{-val} = 0.000397$) and final stress and RFI ($\rho = +0.893$, $p\text{-val} = 0.0123$). There was no such relationship between RFI and final strain (Fig. 1). Due to the relationship between RFI, CHP binding, molecular level collagen unwinding and collagen damage, the observed relationships associated with RFI are also associated with damage. Suggesting that

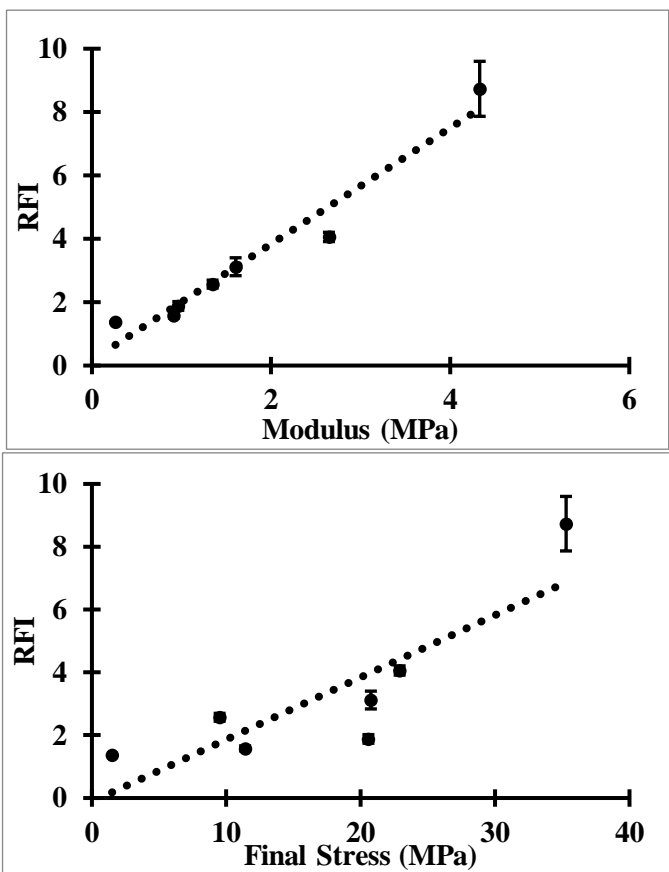


Figure 1. Relationships with relative fluorescent increase (RFI). (a) Plot of RFI vs modulus with linear best fit line (*dashed line*) (b) Plot of RFI vs final stress with linear best fit line (*dashed line*).

there is a relationship between fibril damage and final stress and fibril damage and modulus.

We believe the reason we do not see a relationship with RFI and final strain is due to differences in crosslink density of the collagen fibrils. If two fibrils are taken to the same final strain, but the crosslink density of one fibril is higher than the other, the fibril with a higher crosslink density will experience more damage.

CONCLUSION

These results suggest that there is a relationship between fibril damage and modulus and fibril damage and final stress. We propose that the reason we do not see a relationship between final strain and

fibril damage is due to varying crosslink density between the fibrils.

We have also been able to successfully quantify CHP binding using fluorescence of a single collagen fibril.

REFERENCES

1. Roshan, J., et al. *The Journal of Hand Surgery*. 102-112, 2008.
2. Wu, F., et al. *The Journal of Hand Surgery. EFORT Open Reviews*, 332-342, 2017.
3. Liu, Y., et al. *A Novel Method to Extract Type-I Collagen Fibrils From Mammalian Tendons*. Master's thesis, Case Western Reserve University, 2015.

ACKNOWLEDGEMENTS

I would like thank all the members of my lab who helped me solve the challenges of this research I would also like to thank Jeffery Weiss and Alan Lin from the University of Utah who helped fund this project and also collaborated with us on this project.

Biomechanics of the Praying Mantis Foreleg Strike

¹Walid Abuhashim, ¹Colleen Unsworth, ²Gavin Svenson, ² Sydney Brannoch ¹Henry Astley

¹The University of Akron, Akron, OH, USA

²Case Western Reserve University, Cleveland, OH, USA

Email: waa23@zips.uakron.edu

INTRODUCTION

Praying mantises (*Mantodea*) catch prey via rapid motion of their specialized forelegs. Due to the high speed requirements to catch quick prey items, a mantis must accelerate their limb segments rapidly, which depends upon mechanical power. Besides increase in muscle mass organisms can increase mechanical power output by coupling muscle with an elastic tissue to generate relatively greater power than muscle alone. In this phenomenon, known as power-amplification, elastic potential energy is stored in elastic structures and rapidly released, resulting in power outputs beyond those of muscle, as seen in the flea jump. This research investigates the foreleg strike of the Chinese Mantis (*Tenodera sinensis*) capturing live prey (*Periplaneta americana*) to determine whether power-amplification is used in the mantis strike.

METHODS

The praying mantises were collected from the Cleveland Metro Parks. From the mantises collected, we recorded 11 strikes at 700 frames/second with two Edgertronic high-speed cameras, of the mantises striking at cockroaches attached to strings. The use of 2 cameras allowed us to track the movements of points in three dimensions. We used a calibration device to convert the pixels to metric units.

There were 8 points that were being tracked for the strikes. The points were digitized via MATLAB DLTdv5 software package. These 8 points then made 4 vectors. Upon which we calculated angular displacement, velocity, and acceleration for the 3 joint angles.

The strikes of the mantis were split into 2 phases an extension phase, where the mantis was extending its forearms to attain its prey, and a grabbing phase, where the mantis was closing its arms to grab its prey.

RESULTS AND DISCUSSION

From the 11 strikes, the angles were calculated and plotted as shown in figure 1.

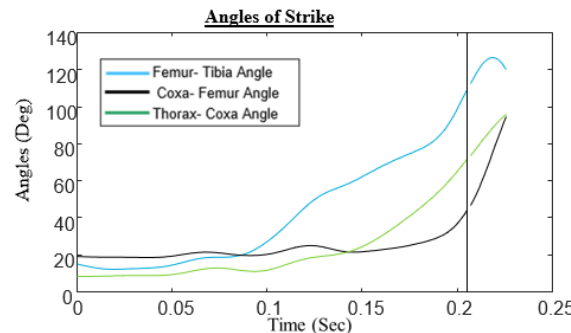


Figure 1: 1 of the strikes joint angular displacements over time, the vertical line denotes the split.

The angular acceleration was then calculated from the angles. the fastest average joint angular acceleration was the Femur Tibia Joint during extension with a velocity of 2,180 deg/sec, as seen from table 1.

Table 1: Average max angular velocity of 11 strikes, split into 2 parts: Extension and Grabbing.

	Peak Angular Velocity	
	Extension (deg/s)	Grabbing (deg/s)
Femur Tibia Joint	2,180	2,130
Coxa Femur Joint	970	2,700
Thorax Coxa Joint	1,260	1,320

Compared to Dr. Patek's study of mantis shrimp, which was found to exhibit power amplification, had an angular velocity of 38,888 deg/sec [1]. More than 10 times faster than the preying mantis strikes. Hence, the angular velocity's suggest purely muscular actuation. To confirm this we will use inverse dynamics to compare joint angles, angular acceleration, torque, and power across individual foreleg segments (coxae, femora, tibiae, tarsi) to identify coordination and control patterns and which joints are primarily responsible for generating power. The apparent lack of power amplification in *T. sinensis* forelegs suggests that tradeoffs may preclude some animals from using it, such as the dual function of *T. sinensis* forelegs for both prey capture and locomotion.

CONCLUSION

The results suggest an apparent lack of power amplification in *T. sinensis* forelegs. For the praying mantis had a fraction of the mantis shrimp speeds. Which had two phases of behavior, extension and grab. The trade-offs may deter some animals from using power amplification, such as the dual function of *T. sinensis* forelegs for both prey capture and locomotion.

REFERENCES

1. Patek, S, et al. *Nature*. Page 428 (2004).

ACKNOWLEDGEMENTS

We would like to acknowledge the University of Akron Biology Department Tiered mentoring program for funding part of this research, and pairing the student with the lab. As well as Stephen Howe for demonstrating how to use and setup the cameras.

Upper Body Estimation of Muscle States and Joint Motion Using Extended Kalman Filter

¹Hanieh Mohammadi and Gholamreza Khademi¹, Dan Simon, Antonie J. van den Bogert, Hanz Richter

¹Cleveland State University, Cleveland, OH, USA

²Cleveland State University, Cleveland, OH, USA

Email: h.mohammadi17@csuohio.edu

INTRODUCTION

This paper synthesizes modeling techniques and dynamic state estimation techniques for the simultaneous estimation

of the muscle states, muscle forces, and joint motion states of a dynamic human arm model. The estimator considers both muscle dynamics and motion dynamics. The arm model has two joints and six muscles and contains dynamics both of the muscles and of the motion. We develop an optimally-tuned extended Kalman filter (EKF) using noisy measurements of joint angles with standard deviation 2.87 deg, of joint velocities with standard deviation 6.9 deg/s, and of muscle activations with standard deviation 10% of their peak values, and then simultaneously estimate joint angles, joint velocities, muscle forces, joint moments, and muscle states.

The standard deviations of the estimation errors (SDEE) are no more than 0.07 deg for joint angles, 1 deg/s for joint velocities, 0.6 mm for muscle-tendon lengths, and 0.1 Nm for joint torques. The results are compared with a previously developed static optimization method, and verify the effectiveness of our proposed estimator in providing lower SDEE for both muscle and motion dynamics of the human arm model compared to the static optimization method.

METHODS

The musculoskeletal model represents a human arm constrained to planar motion. This system has two joints and six muscles. Our specific aim is to estimate the human musculoskeletal signals during workout with advanced exercise machines. We simultaneously estimate the muscle states and

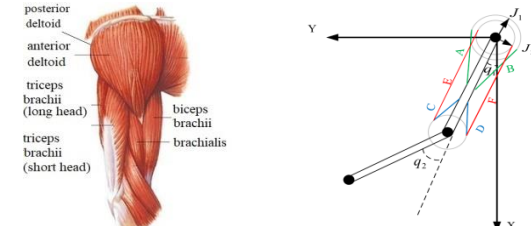


Figure 1: (a) side view of planar arm model with motion in the vertical plane [1], and (b) front view of the human arm muscle system, adapted from [2].

joint motion states of a human arm mode. We develop an optimally-tuned extended Kalman filter (EKF). We use noisy measurements of joint angles, joint velocities, and muscle activations. The EKF simultaneously estimates joint angles, joint velocities, muscle forces, and muscle states. The Human arm dynamic equation is:

$$\mathbf{M}(\mathbf{q})\ddot{\mathbf{q}} + \mathbf{C}(\mathbf{q}, \dot{\mathbf{q}})\dot{\mathbf{q}} + \mathbf{G}(\mathbf{q}) \quad (1)$$

where $\mathbf{M}_{2 \times 2}$ is the mass matrix, $\mathbf{C}_{2 \times 2}$ is the Coriolis matrix, $\mathbf{G}_{2 \times 1}$ is the gravity vector, \mathbf{q} , $\dot{\mathbf{q}}$, $\ddot{\mathbf{q}}$: the vectors of joint angles, velocities, and accelerations, τ is the vector of joint moment s generated by the six muscles.

Now we design an extended Kalman filter (EKF) for state estimation of the two-joint, six-muscle human arm model. The human arm model is a system with highly nonlinear dynamics. Suppose the state space representation of the model is written in the general form:

$$\begin{aligned} \dot{\mathbf{z}} &= f(\mathbf{z}, \mathbf{u}, t) \\ \mathbf{y} &= h(\mathbf{z}, \mathbf{v}, t) \\ \mathbf{w} &\sim (\mathbf{0}, \mathbf{Q}), \mathbf{v} \sim (\mathbf{0}, \mathbf{R}) \end{aligned} \quad (2)$$

The following Jacobians are calculated to form the EKF for the arm model:

$$\mathbf{A}_f = \frac{\partial f}{\partial \mathbf{z}} \Big|_{\hat{\mathbf{z}}} \quad \mathbf{C}_h = \frac{\partial h}{\partial \mathbf{z}} \Big|_{\hat{\mathbf{z}}} \quad \mathbf{L}_f = \frac{\partial f}{\partial \mathbf{w}} \Big|_{\hat{\mathbf{z}}} \quad \mathbf{M}_h = \frac{\partial h}{\partial \mathbf{v}} \Big|_{\hat{\mathbf{z}}}$$

The EKF Equations are:

$$\begin{aligned}\hat{\mathbf{z}} &= f(\hat{\mathbf{z}}, \mathbf{u}, 0, t) + \mathbf{K}[\mathbf{y} - h(\hat{\mathbf{z}}, 0, t)] \\ \mathbf{K} &= \mathbf{P} \mathbf{C}_h^T \tilde{\mathbf{R}}^{-1} \\ \dot{\mathbf{P}} &= \mathbf{A}_f \mathbf{P} + \mathbf{P} \mathbf{A}_f^T + \tilde{\mathbf{Q}} - \mathbf{P} \mathbf{C}_h^T \tilde{\mathbf{R}}^{-1} \mathbf{C}_h \mathbf{P}\end{aligned}$$

$$\begin{aligned}\tilde{\mathbf{Q}} &= \mathbf{L}_f \mathbf{Q} \mathbf{L}_f^T \\ \tilde{\mathbf{R}} &= \mathbf{M}_h \mathbf{R} \mathbf{M}_h^T \\ \mathbf{z}(0) &= E[\mathbf{z}(0)] \\ \mathbf{P}(0) &= E[(\mathbf{z}(0) - \hat{\mathbf{z}}(0))(\mathbf{z}(0) - \hat{\mathbf{z}}(0))^T]\end{aligned}$$

We assume that the output measurements are linear functions of the states and measurement noise, and the system dynamics is a linear function of the process noise. Thus, the only Jacobian we need to calculate is $A_f = \frac{\partial f}{\partial \mathbf{z}}|_{\hat{\mathbf{z}}}$.

RESULTS AND DISCUSSION

We assume the available noisy measurements are joint angles, joint velocities, and activation signals. The tuning parameters of the EKF are tuned by defining an optimization problem in such a way that the standard deviations of the estimation errors are minimized. The performance of the EKF in estimating joint angles and velocities is shown in Figure 2, which shows that the estimates converge in spite of large initial estimation errors and high measurement noise. The performance of the EKF in estimating contractile lengths and muscle forces are shown in Figures 3. We considered very large initial estimation errors for the tendon lengths by assuming that all six tendons are at their slack lengths because there is no available measurement for such states. The EKF performed well in spite of these large initial estimation errors and high measurement noise of the joint angles and joint velocities and converged to their actual values accurately.

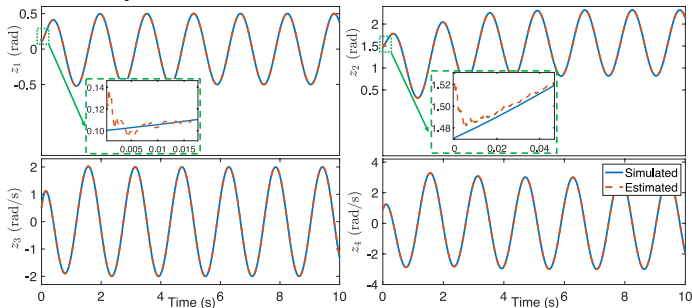


Figure 2: The simulated and estimated values of z_1 , z_2 , z_3 , and z_4 .

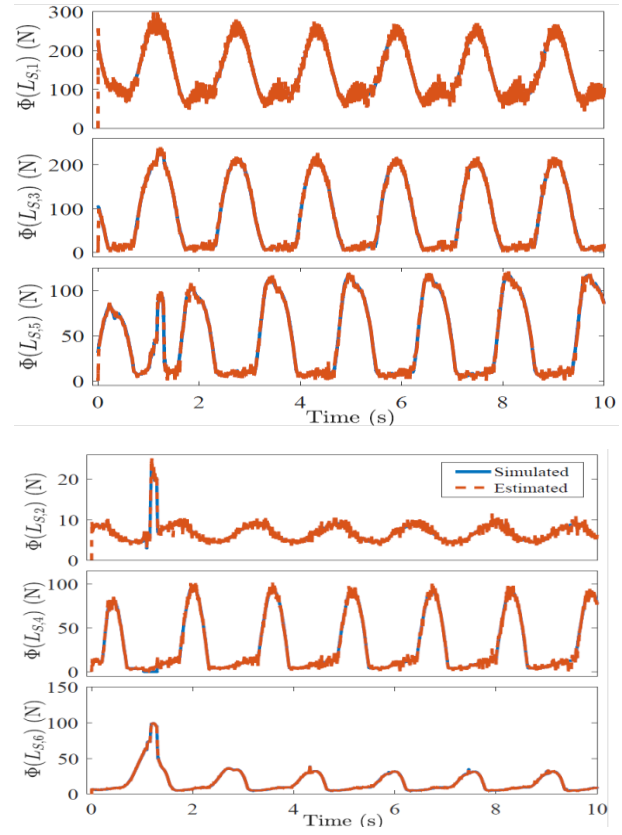


Figure 3: The simulated and estimated values of six muscle forces.

CONCLUSION

In this paper, we proposed a method for simultaneous estimation of a human arm model. We used the joint angles, joint velocities, and activation signals as measurements, and we designed an EKF to estimate the joint angles and velocities, muscle forces, and muscle states for all muscles attached to the shoulder and elbow joint. We considered high measurement noise to evaluate the EKF with non-zero initial estimation errors. We conclude that the EKF can successfully estimate joint motion states, joint moments, muscle forces, and muscle states.

REFERENCES

- [1] Jagodnik, K.M., van den Bogert, A.J.: ‘Optimization and evaluation of a proportional derivative controller for planar arm movement’, Journal of Biomechanics, 2010, 43, (6), pp. 1086–1091
- [2] Strickland, A.. ‘Gross anatomy and functions of skeletal muscles’. , 2015. Available from: <https://slideplayer.com/slide/4311270/>

ACKNOWLEDGEMENTS

This research was supported by National Science Foundation Grants 1344954 and 1536035.

ANALYZING JOINT ANGLES AND JOINT LOADS IN THREE DIFFERENT POSTURES

Archana Lamsal¹, Garrett Weidig¹ and Tamara Reid Bush, PhD¹

Teresa Bellingar, PhD²

¹Michigan State University, East Lansing, MI, USA ²Haworth, Holland, MI, USA

email: lamsalar@msu.edu, reidtama@egr.msu.edu

INTRODUCTION

Office workers can spend as much as ten to eleven hours in a seated posture, causing prolonged physical inactivity [1]. This can lead to health risks such as poor metabolism, type-two diabetes, and obesity [2]. Research indicates that breaks in prolonged sitting reduce these health risks in office workers [2].

Using Sit-to-Stand workstations has been shown to break up the time spent seated [3]. However, standing for long periods of time has also been associated with musculoskeletal disorders, pain, and discomfort [4]. Current research suggests a need for an alternative which can provide changes in posture without subjecting the legs to large loads. The goal of this study was to compare the joint angles, joint moments and loading on the body between being seated, a new type of mid-seated posture, and standing.

METHODS

Twenty consenting participants (ten males and ten females) were recruited. An 11-camera motion capture system and force plate were used for this study. Reflective markers were attached on the toe, lateral malleolus, lateral epicondyle, greater trochanter, glenohumeral joint, anterior superior iliac spine (ASIS), and posterior superior iliac spine (PSIS). The participants were asked to conduct a computer task in three different postures, spending fifteen minutes in each posture. The postures were: seated, mid-seated, and standing. The mid-seated posture was with a slightly bent knee, in an elevated chair with their feet on the ground. Marker position and ground reaction force were collected for every posture and during transition between postures. Data for all postures and motions were collected for 20 participants. Additionally, a sub-set of three participants returned to the lab to conduct

movements directly from seated to the standing position.

Joint angles at the knees, ankles, and hips were calculated for all three postures. These angles were obtained by using vectors to represent the foot, shank and thigh segments. In addition, pelvic tilt (angle between the pelvic plane and horizontal) and openness angle (angle between the thorax and pelvis) were calculated for all postures. Inverse dynamics was used to compute joint moments in the sagittal plane for transition between three postures, also referred to as dynamic motions. The motions were: seated-to-mid-seated (Sit-M), mid-seated-to-standing (M-S), and seated-to-standing (Sit-S). Anthropometric data for calculating joint loads were taken from Winter [5].

RESULTS AND DISCUSSION

The ground reaction force in mid-seated posture was slightly higher than the seated posture but significantly lower than standing (Figure 1).

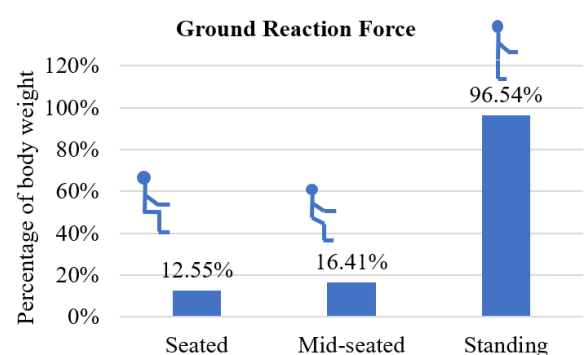


Figure 1 Average ground reaction forces across the subject pool for each posture in terms of percent body weight

All the joint angles for the mid-seated posture were between the values for seated and standing postures (Table 1). However, interesting to note that even while "seated" in the mid posture, the pelvis was able

to be moved to a point halfway between the seated and standing postures. This is shown by the change in pelvic tilt angles and also supports a change in lumbar curvature.

The openness angle was smallest in the seated posture and largest in the standing posture. Previous research has shown that a larger openness angle is correlated to an increased lordotic lumbar curvature [6]. This is another measure that confirms lumbar articulation is occurring in this mid-seated position – even though the person is still sitting down.

Table 1 Average joint angles and standard deviations in degrees across the subject pool for each posture

Angles	Seated	Mid-seated	Standing
Ankle	101.2 (5.9)	97.3 (4.6)	93.8 (3.4)
Knee	101.1 (6.6)	111.1 (5.8)	171.7 (4.3)
Hip	116.9 (6.2)	123.0 (8.0)	169.8 (4.9)
Pelvic Tilt	15.3 (6.6)	6.3 (6.6)	-8.4 (7.6)
Openness	96.7 (15.7)	102.1 (14.0)	116.5 (17.1)

It was observed that during transition, some participants used the armrest for support. As the use of armrest affects the joint moments, those two groups of people were analyzed separately. The average maximum joint moments for the three motions for the participants who used the armrest and who did not use the armrest showed similar trends. The ankle moment was largest in the Sit-S motion and smallest in the Sit-M motion. The knee moment was largest in the Sit-S motion and smallest in the M-S motion. The hip moment was largest in Sit-M motion and smallest in M-S motion.

All the joint moments were smaller for M-S motion compared to Sit-S motion. Moving from the mid-seated position to standing put lower load on the joints than standing directly from the seated position. The Sit-M motion had smaller joint moments in the knee and ankle joints compared to Sit-S motion. However, the hip moment was the largest in the Sit-

M motion. The hip moment was largest because participants had to lean forward to move the seat into the second position. This resulted in the shoulder joint being more anterior to the hip joint during the Sit-M motion, which resulted in larger moment arm for the torso weight. This, in turn, resulted in higher moments.

CONCLUSIONS

The considerably lower leg loads in the mid-seated posture compared to standing posture was a positive outcome. Prolonged loads on feet while standing lead to pain and musculoskeletal discomfort. The change in posture from the seated to the mid-seated posture provided a significant change in joint angles (especially pelvic tilt). The pelvic tilt coupled with the decreased leg loads suggests positive benefits of lumbar motions but without the negative leg loads.

Standing from mid-seated posture is easier on the joints than standing from a standard seated posture, as the moments in ankle, knee and hip were smaller compared to rising from a seated posture. The transition from the seated posture to a mid-seated posture, however, put a larger moment on the hip joints. Considering all the facts, one can say that the mid-seated posture provides the benefit of both sitting and standing. It reduces the load from the feet in comparison to standing and is easier to stand from in comparison to the seated posture. Change of posture from seated posture to mid-seated posture also provides motion to the joints and lumbar region.

REFERENCES

1. Smith L., et al., *BMC Public Health*, 1-9, 2015
2. Hamilton MT, et al., *Diabetes*, 2655–2667, 2007
3. E F Graves, L., et al., *BMC public health*, 2015
4. Boussenna, M., et al., *Ergonomics*, 315–322, 1982
5. Winter, D. A., *Biomechanics and motor control*. John Wiley & Sons, 2009
6. Leitkam ST., et al. *Journal of Biomechanics*. 2011

ACKNOWLEDGEMENTS

This work was supported by Haworth Inc.

ON THE CLINICAL DIAGNOSIS OF ACROMIOCLAVICULAR JOINT ARTHRITIS

¹Arn, Bethany, ¹Hefzy, Mohamed Samir, ²Trease, Brian, and ³Mustapha, Abdulazim

¹Biomechanics and Assistive Technology Laboratory

²Mechanism, Mobility and Multifunctional Design Laboratory, ³Department of Orthopaedic Surgery

The University of Toledo, Toledo, OH, USA

Email: bethany.grayczyk@rockets.utoledo.edu

INTRODUCTION

Osteoarthritis of the acromioclavicular (AC) joint has been said to be a common source of shoulder pain, and is said to be the most common source in patients over the age of 50, with over 50% of the patients showing radiographic signs of degenerative arthritis [1,2]. The pain associated with AC osteoarthritis is thought to be caused by irritation of the subacromial bursa when the AC joint becomes inflamed or has protruding osteophytes and the cross body adduction (CBA) test is a current clinical diagnosis of this pathology [3]. However, recently, another test has been proposed that involves placing the hand behind the back (HBB).

In a clinical setting, it was observed that some patients test negative for pain under the CBA test and positive under the HBB test. These patients were later found to have arthritis of the AC joint through imaging or arthroscopic means. The purpose of this study is to investigate the biomechanics of these two positions in order to determine if the HBB test is a better one.

METHODS

The Zygote Solid 3D Male Human Anatomy model by ZYGOTE (American Fork, UT) was used to construct a 3D CAD model of an adult 50th percentile male shoulder and chest cavity. This model is created as a SolidWorks file, Dassault Systèmes (Vélizy-Villacoublay, France). This model was then imported into MSC.ADAMS, Adam View 2017 by MSC Software (Newport Beach, CA) in order to

model and study the dynamics of the shoulder in three specified positions — standard anatomical, CBA and HBB. The model includes the clavicle, scapula, humerus, and the rib cage. The radius and ulna were combined as a single rigid body. Similarly, the 27 bones of the hand were considered as one segment.

Three revolute joints were used to model the glenohumeral joint allowing rotations around three different axes. A spherical joint was used to model the elbow joint. In order to move from one position to another, these six rotations were identified.

Nine springs were used to model five ligaments, with stiffness identified from the literature [4]. Three muscle forces were introduced into the model for the CBA position and two for the HBB position. In order to account for the complexity of the contact constraints of the scapulothoracic contact, tangential springs were introduced in order to allow scapular motion along the curvature of the thorax.

The shortest distance between the distal clavicle and the acromion process of the scapula was calculated as an indicator of the intensity of the stress at the articulating surfaces, which would indicate the presence of arthritis at the AC joint.

RESULTS AND DISCUSSION

Table 1 shows the three rotations at the glenohumeral joint and the three rotations at the elbow joint that were used to position the skeleton in the CBA and HBB positions, moving from the anatomical

position. Figure 1 depicts the skeleton at both positions.

Table 1: Rotations used to position the skeleton in both the CBA and HBB positions

Joint	Joint Type (Model)	CBA		HBB	
		Angle (deg)	Process Step	Angle (deg)	Process Step
Glenohumeral	-	-	-	-	-
Glenohumeral - M/L	Revolute	28	3	20	3
Glenohumeral - A/P	Revolute	-90	2	45	2
Glenohumeral - Rot.	Revolute	90	1	90	1
Elbow	Spherical	-	-	-	-
	Global X	90	4	120	4
	Global Y	0	-	-10	6
	Global Z	10	5	-45	5

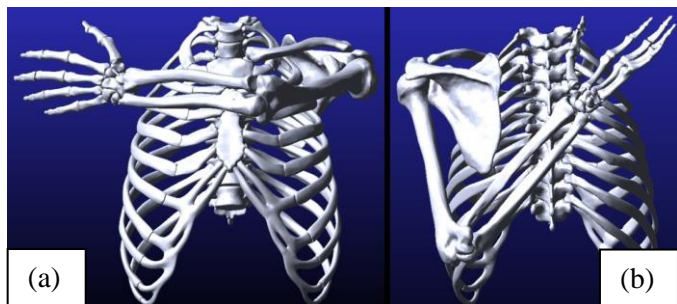


Figure 1: (a) cross body adduction and (b) hand behind the back positions

The shortest distances between the distal clavicle and acromion process of the scapula for these two positions were obtained interactively using ADAMS and are listed in Table 2. This table also includes the shortest distance in the anatomical position obtained from the literature [5] as well as using ADAMS and using SolidWorks.

Table 2: Minimum distances between the distal clavicle and acromion process

Source	Distance (mm)
Literature [5]	3.32
Anatomical (SW)	3.14
Anatomical (ADAMS)	3.16
CBA (ADAMS)	2.85
HBB (ADAMS)	1.54

CONCLUSIONS

Table 2 shows that the acromion process of the scapula moves to different locations relative to the clavicle. With CBA decreasing the distance between the distal clavicle and the acromion process by 0.31 mm there is an indication that the stress level at the joint increases, thus causing irritation and inflammation of the AC joint and suggesting that arthritis is present at that location. It is then understandable that this is the current method of clinically diagnosing osteoarthritis of the AC joint.

Additionally, Table 2 shows that the spacing at the AC joint is decreased by 1.62 mm from the standard anatomical position, in the HBB position, indicating that this is also a valid test for arthritis of the AC joint. Due to the over 5x greater reduction in space, the HBB position may be argued that it is a better test to diagnose earlier stages of osteoarthritis because of the higher stress and degree of irritation that is placed upon the AC joint.

In order to validate this model it is necessary to conduct an experimental study by taking X-Rays of the shoulder complex of subjects passively holding their arms in the three specified positions.

REFERENCES

- Petersson, C., *Acta Orthopaedica Scandinavica*, vol. 54, no. 3. 434-438, 1983.
- Horváth, F., et al. *Archives of Gerontology and Geriatrics*, vol. 3, no. 3, 259-265, 1984.
- Buttaci, C., et al. *American Journal of Physical Medicine & Rehabilitation*, vol. 83, no. 10. 791-797, 2004.
- Soslofsky, L., et al. *Repair and Regeneration of Ligaments, Tendons, and Joint Capsule*. Humana Press, 2005.
- Edwards, S., et al. *Arthroscopy: The Journal of Arthroscopic and Related Surgery*, Vol. 23, no. 12. 1278-1284, 2007.

A Novel Approach to Midfoot Reconstruction Surgery in Patients with Charcot Arthropathy

¹Jessi Martin, ¹Deborah Falokan, ¹Michala Dauterman, ¹Jelena Bundalo, and ²Dr. David Kay

¹The University of Akron, Akron, OH, USA

²The Crystal Clinic Orthopedic Center, Akron, Ohio,
USA Email: jkm71@zips.uakron.edu

INTRODUCTION

Charcot arthropathy is a condition first described by French neurologist, Jean-Martin Charcot, in 1860. [1] Current leaders in orthopaedic surgery explain Charcot arthropathy as:

"... a progressive destruction of bone and joints, which is usually caused by unrecognized injury and occurs in people who have peripheral neuropathy." [1]

Peripheral neuropathy is a condition resulting from damage to the peripheral nerves. Muscle weakness, numbness, lack of coordination, and pain are some of accompanying clinical symptoms. [2] These may initially go unnoticed; however, patients may repeatedly trigger inflammatory responses in their feet. [3] If this condition progresses untreated, the arch of the foot may fracture, resulting in a dysfunctional "rocker-bottom" foot.

METHODS

This project utilized the stage-gate process outlined in the guideline diagram set forth by the Food and Drug Administration (FDA) for the design and development of medical devices, shown in Figure 1. Customer requirements were identified in the User Needs stage. These were used to develop a clinical needs statement for a new implant to reduce failures.

At the Design Input stage, a set of design specifications was based on customer requirements, industry standards, and risk assessment results. This led to the Design process stage, where an initial implant design concept was based on customer requirements and design specifications.

For the Design Output stage, prototypes of the implant design were created, utilizing 3D modeling software and engineering calculations. During the Medical Device Stage, testing and risk assessment were conducted.

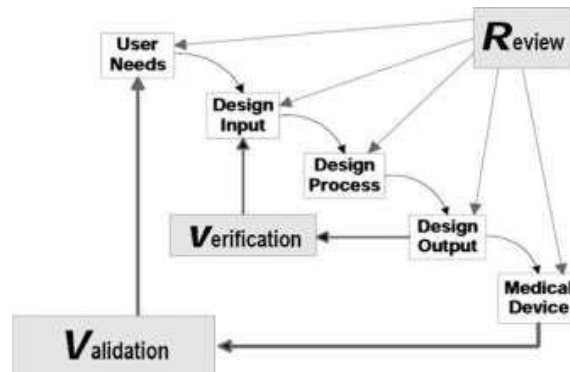


Figure 1: FDA Waterfall Diagram of Design Controls [4]

RESULTS AND DISCUSSION

This project utilized the FDA design process to address a real-world problem facing orthopedic surgeons. The result of this project is a beta prototype of the final design, as well as documentation for the design process. In addition, a Design History File was created that documented the entire design process.

REFERENCES

- [1] Jani, M. M., & Johnson, J. E. (2002, January 30). Charcot Neuropathic Arthropathy.
- [2] Peripheral neuropathy. (2019, May 22).
- [3] Rogers, L. C., Frykberg, R. G., Armstrong, D. G., Boulton, A. J. M., Edmonds, M., Van, G. H., ... Uccioli, L. (2011, September 1). The Charcot Foot in Diabetes. Retrieved from <https://care.diabetesjournals.org/content/34/9/2123>.
- [4] https://www.researchgate.net/profile/Lauren_Shluza_s/publication/262375810/figure/fig6/AS:668296957_399063@1536345819620/Application-of-design-controls-to-waterfall-design-process-13.ppm Retrieved on November 25, 2019.

ACKNOWLEDGEMENTS

We would like to acknowledge Dr. David Kay for his time and assistance on this project. We also would like to acknowledge the University of Akron, Dr. James Keszenheimer, and Dr. Adel Alhalawani for providing our team the resources and education that allowed us to design and develop our beta prototype.

Index

- Abdollahi, Neda, 11
Abuhashim, Walid, 97
Akkus, Ozan, 77, 87, 91
Al-Adayleh, Assel, 56, 70
Allen, Natalie, 85
Amadio, Joseph M., 79
Ambike, Satyajit, 66, 68
Arn, Bethany, 103
Arnold, Nicole, 53
Astley, Henry, 97
- Baron, Elise, 17
Baroudi, Loubna, 19
Barton, Kira, 19
Bazett-Jones, David M., 3
Bellingar, Teresa, 101
Beveridge, Jillian E., 17
Bigelow, Kimberly E., 43
Biswas, Dipankar, 60, 62, 85
Brannoch, Sydney, 97
Bundalo, Jelena, 105
Bush, Tamara R., 31, 37, 53, 101
- Cain, Stephen M., 19, 27
Chambers, Nicholas, 45
Chander, Harish, 15
Chokhandre, Snehal, 13
Christopher, Slater, 95
Classen, Trenton, 35, 83
Claxton, Laura, 68
Cooper, Austin, 68
Cui, Chuyi, 66
- Dauterman, Michala, 105
Davis, Brian L., 5, 7, 89
De las Casas, Humberto, 45
DePons, Gianna, 3
DiBerardino, Louis A., 27
Dikici, Yusuf, 87
Drost, Joshua, 53
- Eppelheimer, Maggie, 81, 85
Eppell, Steven J., 74, 95
Erdemir, Ahmet, 11, 13
Espy, Debbie, 25, 93
- Falokan, Deborah, 105
Fang, Shanpu, 47, 49
Farrag, Mahmoud, 21
- Fretwell, Andrew, 83
Garcia, Micah, 3
Gillespie, Robert J., 91
Gupta, Sanjay, 77
- Haddad, Jeffery, 66
Halloran, Jason P., 11, 33
Hardin, Elizabeth C., 9, 23
Hefzy, Mohamed Samir, 103
Hieronymus, Brooke, 39
Hijaz, Adonis, 77
Hill, Christopher M., 15
Holst, Brianna, 64
- Ina, Jason, 91
Isali, Ilaha, 77
- Jackson, Elizabeth, 19
Jackson, Kurt, 43
Jain, Mukesh, 77
Jones, Kerwyn, 7
- Kay, David, 105
Kesavan, Lekha Y., 91
Khademi, Gholamreza, 99
Kharlamov, Alexander, 79
Kim, Jiyoong, 81
Kinney, Allison L., 47, 49
Klonowski, Ellen, 13
- Lamsal, Archana, 37, 101
Laxganger, Amanda, 93
Learn, Greg D., 91
Leipzig, Nic D., 21
Li, Bo, 87
Li, Li, 74
Loth, Francis, 60, 62, 81, 85
- Mallinos, Alexandria, 7
Martin, Jessi, 105
McCabe, Jessica P., 9, 23
McClellan, Phillip, 77, 91
Mileski, Joseph W., 27
Miller, Mark C., 79
Mohammadi, Hanieh, 99
Morkos, Mark, 85
Muir, Brittney, 66
Mustapha, Abdulazim, 103

- Neumann, Erica, 13
Newman, Mark, 19
Norman, Timothy L., 35, 39, 64, 83

O’Shea, Leah, 51
Osman, Hala, 25

Park, Dong Jae, 15
Pauley, Jordan, 51
Pensworth, Joel, 35, 39, 83
Petrik, Antal K., 56, 70
Pinto Costa, Rayanne, 60, 62
Pukale, Dipak, 21
Pundik, Svetlana, 9, 23

Reinthal, Ann, 25, 93
Reissman, Megan, 47, 49, 51
Reissman, Timothy, 49
Richey, Nick, 53
Richter, Hanz, 45, 99
Rietdyk, Shirley, 66
Rotello, Rocco, 64

Sahlani, Andrew L., 56, 70
Schearer, Eric, 41, 58
Schultz, Jack, 58
Scott, Justin, 31, 53
Seman, Sarah, 64
Shankar, Eswar, 77
Shelton, Andrew, 27
Shomper, Matthew, 35, 83
Shorter, Alex, 19
Simon, Dan, 99
Skelly, Margaret, 9, 23

Smolinski, Anne, 79
Smolinski, Kathryn, 79
Sommers, Brittany, 89
Song, Jiafeng, 9, 23
Sparks, Kenneth, 45
Svenson, Gavin, 97

Thompson, Paige, 68
Tiell, Shaye, 5
Trease, Brian, 103
Twohy, Kyra E., 43

Unsworth, Colleen, 97

van den Bogert, Antone J., 25, 29
van den Bogert, Antonie J., 99
van Emmerik, Richard, 66
Vertosnik, Alex C., 56, 70
Vertosnik, Louis F., 56, 70
Vijayan, Vinayak, 47, 49
Vocelle, Amber, 53

Wajda, Douglas A., 89
Wang, Huawei, 29
Webster-Wood, Victoria, 91
Weidig, Garrett, 37, 101
Wilson, Samuel J., 15
Wolf, Derek, 41
Wood, Tyler, 15

Yao, Junyao, 60, 62

Zaylor, William, 33
Zypman, Fredy R., 74